Neutron Polarization Studies

with the $D(d,n)^3$He reaction.

thesis

submitted by

Alasdair Stewart Hall, M.Sc.

for the degree of

Doctor of Philosophy

University of Edinburgh

1976

ABSTRACT.

This thesis establishes the trend of neutron polarization in the $D(d,n)^3He$ reaction in the 3 to 5.5 MeV energy region where discrepancies in previous measurements exist. Determinations of the differential polarization at 290 keV and 460 keV, *deuteron energy* and the analysis of available data below 1 MeV in terms of the $\sum_n a_n \sin 2n\theta$ expansion gives a reliable parameterization of the reaction characteristics where none was previously available. The dependence of the neutron polarization on energy and angle has thus been established. The use of an experimental approach and apparatus consistent with other measurements at neighbouring energies further enhances the acceptability of this data. An interpretation is performed in the context of various models of the reaction.

Further investigations explore the use of the ratio of asymmetries in backward and forward scattering of 3 MeV neutrons by helium as a means of selecting between the various analysing power curves for n-^{4}He scattering. The implications of the agreement with the phase shifts of Austin et al [69] are considered and proposals for further studies are made.

Important in attaining these objectives were a variety of modifications to detectors and improvements in the modes of data collection which enabled measurements of good statistical accuracy to be obtained under stable accelerator conditions.

DECLARATION.

This thesis has been composed by myself.

The work involved has been performed by myself.

CONTENTS.

Enclosures : H. Davie's Analysing Power Program — Internal Report,
              July 1975

              Nuclear Physics A242(1975)122-128 — Galloway, R.B. et al

CHAPTER 1.

1.1 Thesis objectives.

The experimental work forming the basis for this thesis was undertaken with two basic purposes in mind. The first was to provide data which would be of use in understanding the mechanisms underlying the $D(d,n)^3He$ reaction. The second objective guiding the work was to obtain information for two practical applications involving polarized neutrons, namely 1) the use of the $D(d,n)^3He$ reaction as a source of polarized neutrons, and 2) the use of $n-^4He$ scattering as a polarization analyser.

From a practical point of view, n-He scattering is usually used as an analyser for the measurement of the polarization of neutrons from the $D(d,n)^3He$ reaction. Conversely, the $D(d,n)^3He$ reaction may be used as a source of polarized neutrons to determine the neutron polarization in n-He scattering. A further alternative is to investigate both the reaction and the analysing power-phase shifts jointly by the use of best-fit procedures to the experimental observables.

1.2 <u>Experimental observables:</u> Definitions and choice.

The selection of appropriate properties to be measured is influenced by the existing degree of agreement on values for the observables as well as the relation and sensitivity of various nuclear model formalisms to these observables.

1.2.1 The $D(d,n)^3He$ reaction.

If one is limited to the use of unpolarized deuteron beams and targets, the experimental observables in the $D(d,n)^3He$ reaction are restricted to 1) the differential cross-section $\frac{d\sigma(\theta)}{d\Omega}$ and 2) the polarization $P(\theta)$ of the outgoing neutrons along the direction $\hat{n}$ perpendicular to the reaction plane.

The state of agreement on differential cross-section is satisfactory and fully reviewed up to December 1972 by Liskien [1]; however the reported data on neutron polarization presents an inconclusive picture. Both for the use of the reaction as a source of neutrons with 'known' polarization and for the understanding of the role of spin-dependent forces in this reaction it is necessary to obtain measurements of greater self-consistency and explain the disparities previously observed. The discrepancies in polarization values at 1971 were detailed by Galloway [2] and are illustrated in fig.1. This also indicates the scarcity of observations in the region where P_n changes sign. The parameterisation of the differential polarization has been used
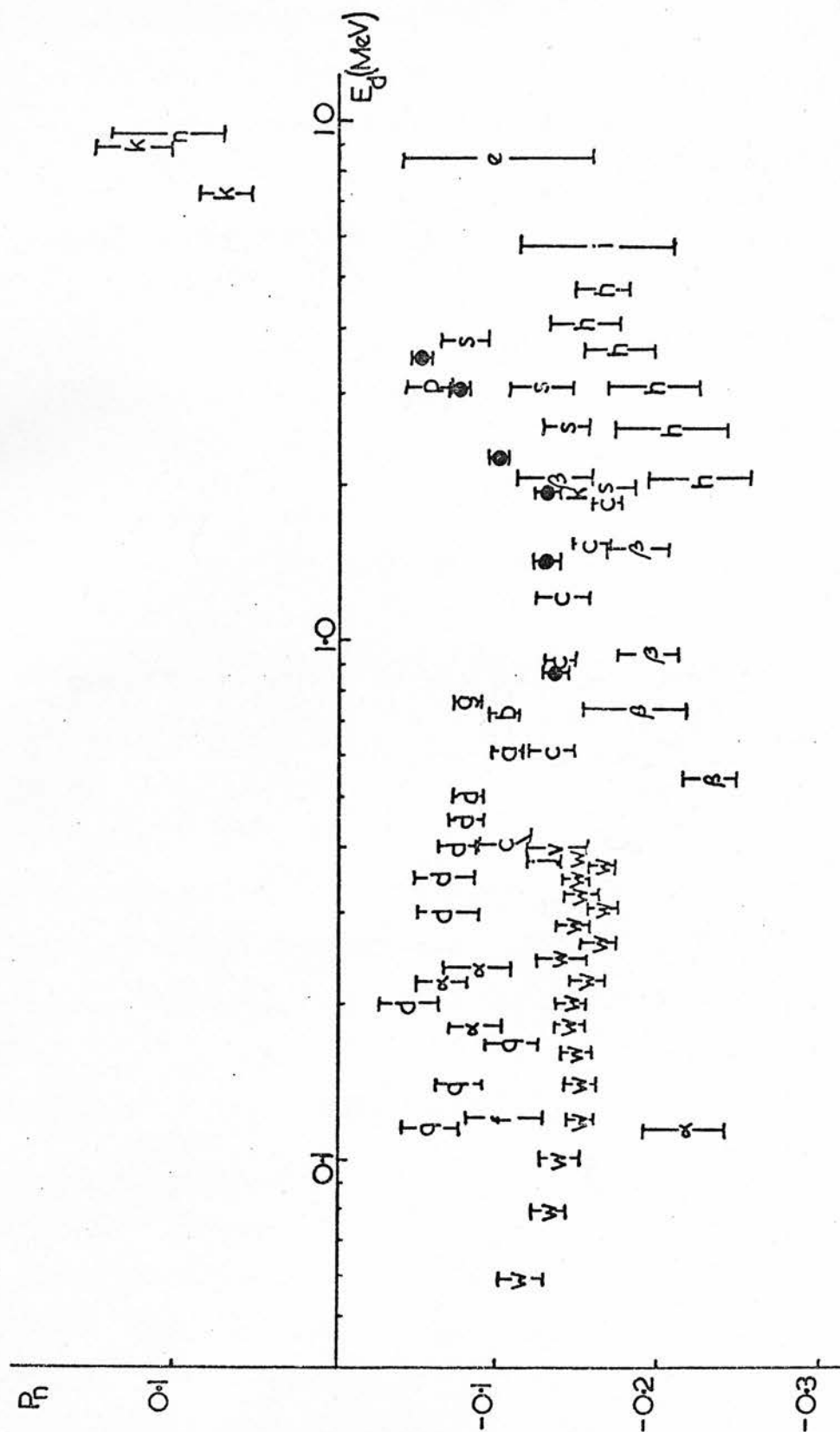
-2-

Figure 1. Polarization of neutrons from the $^2H(d,n)^3$He reaction as a function of incident deuteron energy for laboratory angles of about $45°$ (symbols as in ^{2})).

to determine the importance of spin-orbit terms as described in a more recent paper [3]. The need for confirmation of the trend of lower energy data is indicated by fig.2.

1.2.2 Neutron-Helium scattering.

For neutron energies below the reaction threshold (E_n=22.06MeV) there are three independent measurable quantities which characterise n-alpha elastic scattering for a particular E_n and scattering angle . They are the differential cross-section $I(\theta)$, the polarization $A(\theta)$ and the spin-rotation parameter $\beta(\theta)$. Of these only the first two will be discussed in this work.

The range of analysing power curves at particular energies was reported at the 1970 Polarization Conference [4]. In particular for 3 MeV incident energy the phase shift sets of various groups of workers give rise to the illustrated curves for $A(\theta)$ (fig.3). A means of determining which analysing power curves are experimentally acceptable should at least help eliminate some of the models upon which the associated phase shifts are based.

1.2.3 Summary of Data to be presented.

The totality of data to be presented may be broken into three parts : 1) evaluation of limitations associated with the experimental observations; 2) measurements on the $D(d,n)^3He$ reaction; 3) comparison of the analysing power in the n-He scattering.
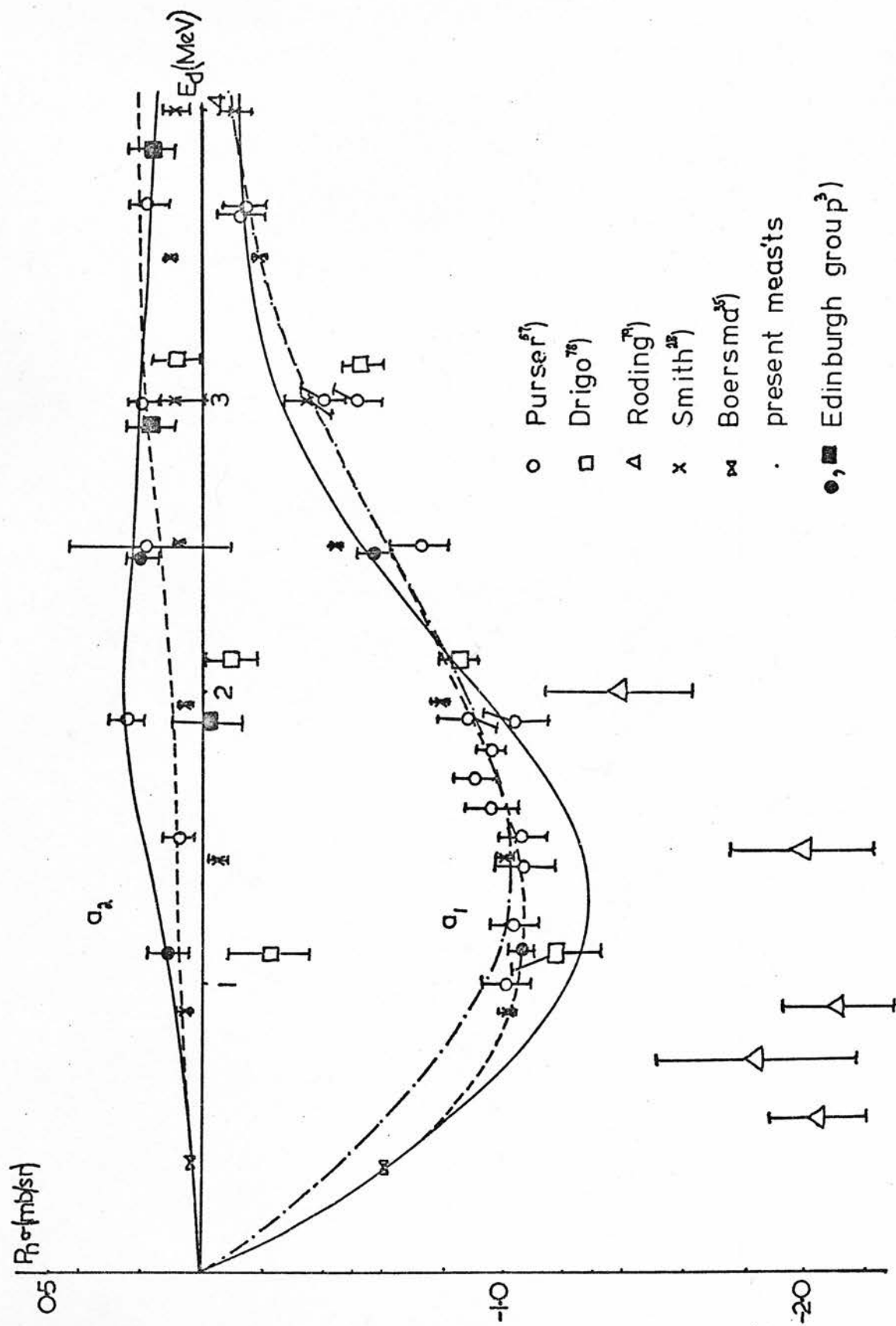
Figure 2. The differential polarization coefficients a_1 and a_2 for deuteron energies up to 4 MeV.
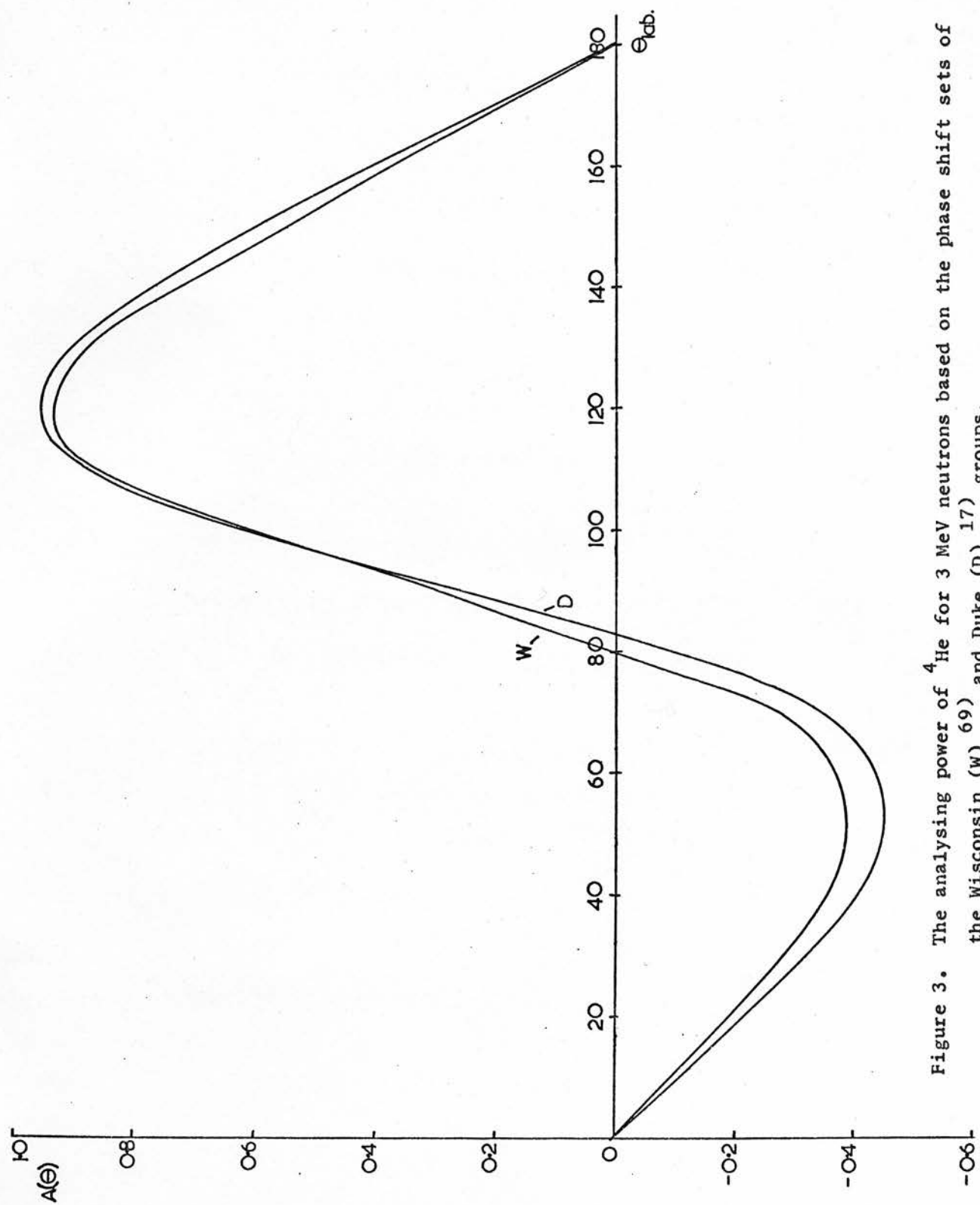
Figure 3. The analysing power of ^{4}He for 3 MeV neutrons based on the phase shift sets of the Wisconsin (W) [69] and Duke (D) [17] groups.

CHAPTER 2.

EXPERIMENTAL APPARATUS.

2.1 General Outline.

An overall picture of the experimental situation may be given with reference to fig.4a. Deuterium ions accelerated to the required energy are brought to a focus on a suitable target. Depending on the type of experiment being performed, a set of signals is produced in a number of detectors placed at appropriate positions in the experimental area. After treatment in the electronics system, a signal is routed to an appropriate section of analyser memory or for some experiments passed to the ADC – computer interface. The computer then performs a certain amount of spectrum sorting to simplify final analysis at a later time. The various elements involved at each stage of this process will be treated in the sections that follow.

2.2 Accelerator and Control Systems.

The accelerator used for the lower energy measurements (at and below 500keV) was an uprated AN-400 Van de Graaff accelerator sited at the Physics Department. This provided a magnetically and electrostatically focussed beam with a resolved current of typically 50μA. The beam spot was focussable to less than 2mm width in the reaction plane under favourable conditions.

deuterium
target

beam-
line
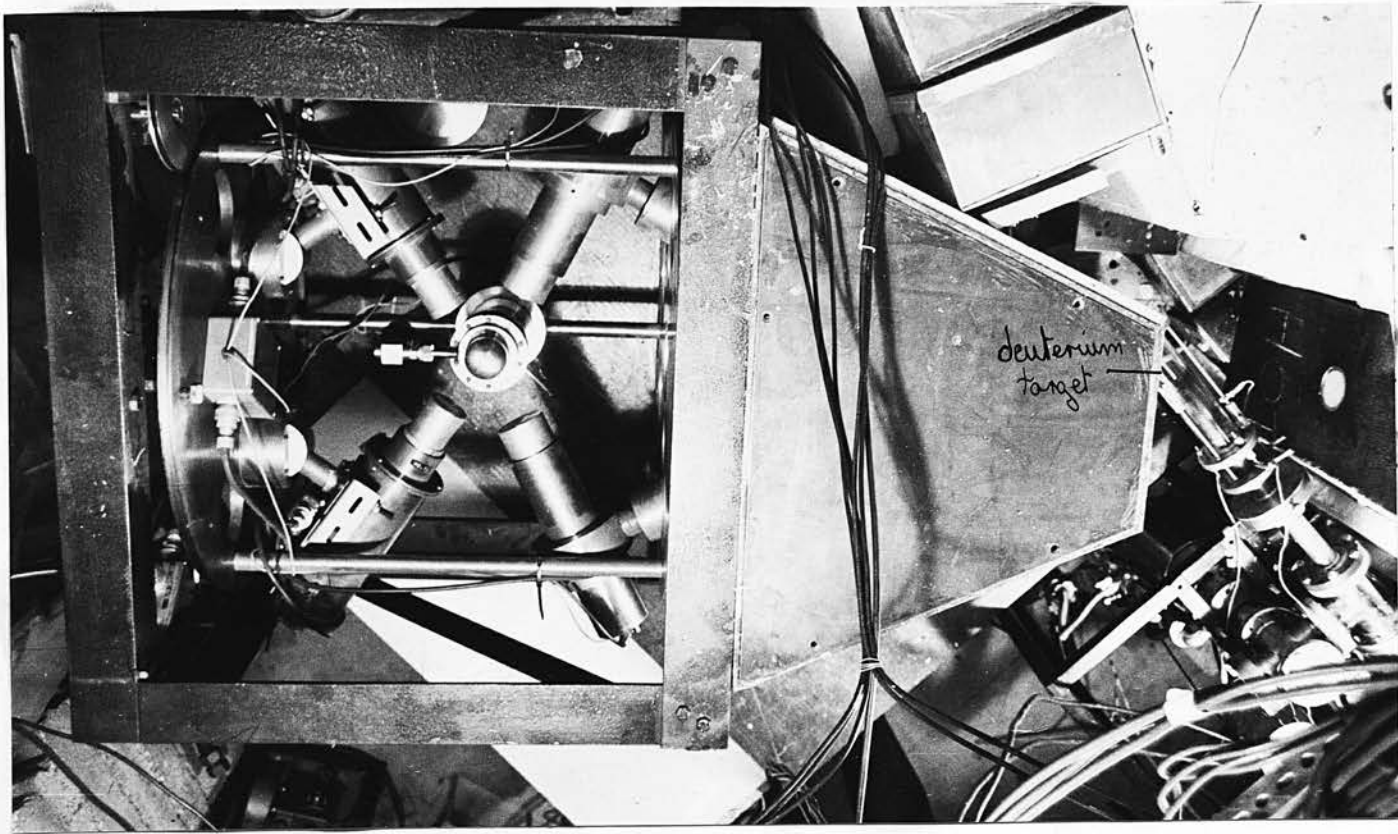
Fig. 4a The polarimeter / collimator system in plan and side elevation.

deuterium
target

d

Ti-D

n

quartz
tube

brass

cooling
water
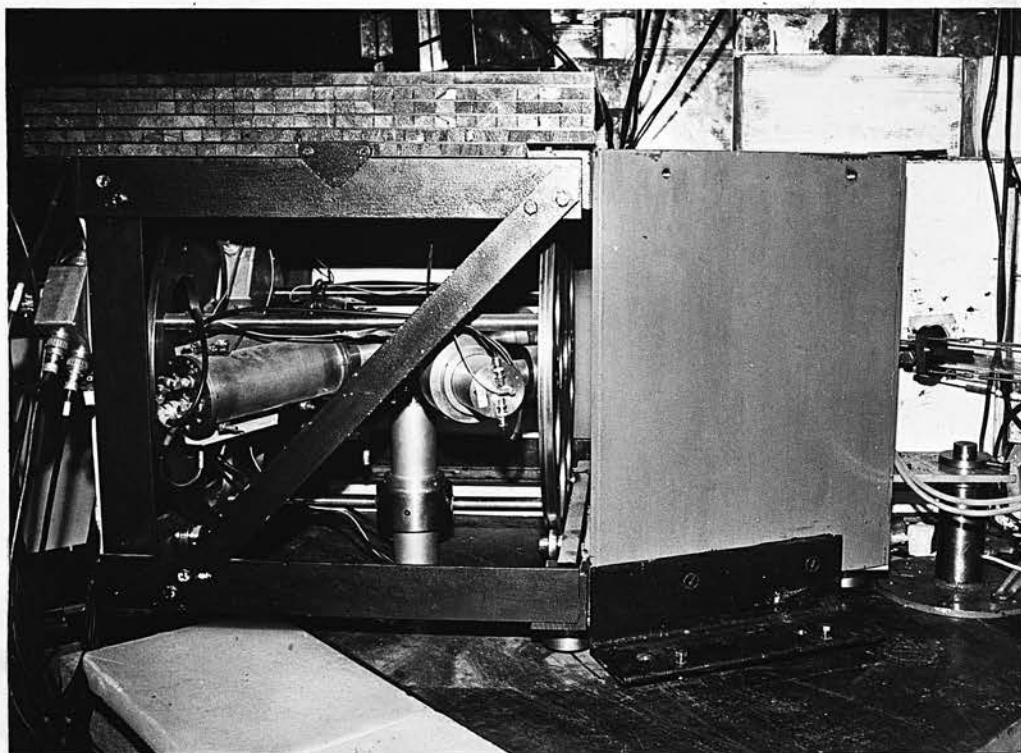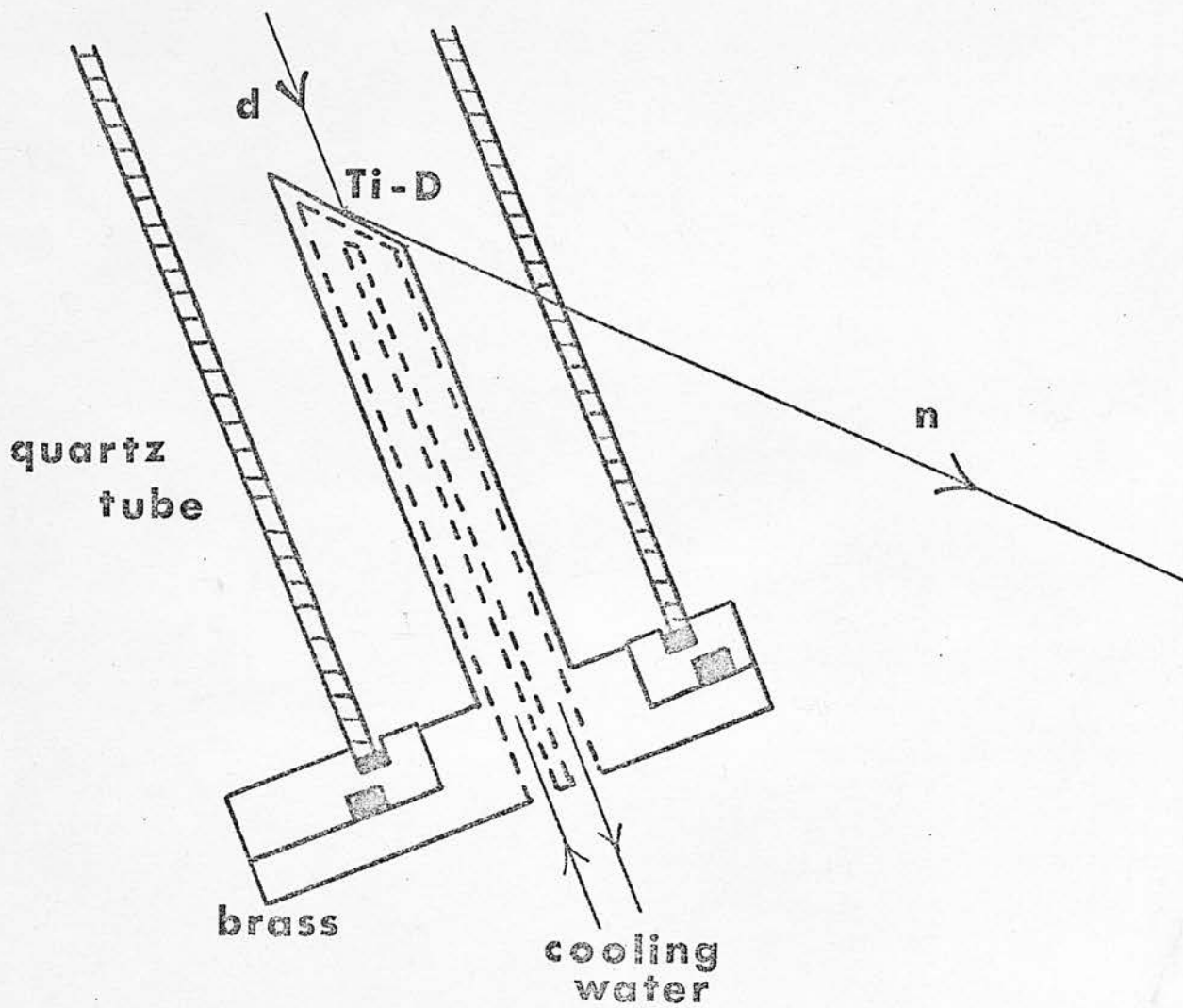
Fig. 4(b). Detail diagram of the deuterium target assembly.

Control of the accelerator was effected in the short term by a
corona feed-back stabiliser system with current monitors 1 metre
up the beam line from the target, and long term drifts in
accelerator function were controlled by a servo system monitoring
corona current and correcting the belt charge according to
transgression of set limits (Appendix A1).

The requirements of good statistics and running stability
favoured the continuous running of this accelerator. A fault
monitoring system was devised to detect the occurrence of
undesirable machine or beam conditions and give audible and
visible indication of this fault condition. The system was able
to cause accelerator shut-down in the event of such conditions
occurring during unattended operation (Appendix A2).

For measurements at higher energy, the 5 MV Van de Graaff
at Harwell A.E.R.E. was utilised. This provided resolved beam
intensities of 20 to 5μA according to accelerating voltage. The
beam spot could be observed with a television camera and was
again of about 2mm width in the reaction plane.

The target system was common to both accelerators. fig4b This has
been described elsewhere [5] but of prime importance is the target
finger construction which gave immunity from the effects of beam
spot wander since the target material projected in the direction
of interest could not exceed 3mm. The target material used in
these investigations was supplied by the Radiochemical Centre,

Amersham, and consisted of a copper backing, coated with a
titanium layer containing absorbed deuterium gas. The target
beam line was maintained at less than 4×10^{-6} torr by oil
diffusion pumping augmented by cold finger trapping for higher
energy runs.

2.3   The Neutron Polarimeter.

2.3.1   Polarimeter design considerations.

The polarization of neutrons is typically determined by
scattering the neutrons from a spin-zero target, and measuring
the left-right asymmetry in the scattering cross-section. This
asymmetry is given by:

$$\mathcal{E} \; = \; P_n A(\theta) \; = \; \frac{L - R}{L + R}$$

where P_n is the polarization of the incident neutrons, and
$A(\theta)$ is the analysing power associated with the spin-zero target.
L and R are the number of neutrons scattered to the left- and
right-hand detectors respectively at the angle θ for a particular
number of neutrons incident on the scatterer. A number of methods
have been employed to determine $\mathcal{E}$ including matched detectors at
left and right, one detector placed alternately to left and right
or a combination of these. The system of detectors and scatterer
must be mounted in a polarimeter cradle which rigidly maintains
their relative positions. The polarimeter may be required to
rotate about a well-defined axis in those systems relying on the

interchange of detectors to eliminate the effect of differences
in detection efficiency. A comparison of the alternative detector
arrangements and their application has been performed by Davie [6].

2.3.2 Experimental observations.

Bearing in mind the criticisms associated with past
polarimeter systems, as well as the requirements of future
observations, it was decided to construct a polarimeter which
overcame the shortcomings inherent in the earlier version used
by this group.

In the majority of previous systems the helium cell has been
placed perpendicular to the collimated neutron beam and observations
to be reported (section 4.1) show the advantages of this arrangement
particularly by comparison with the original polarimeter. In
considering the avoidance of possible causes of indirect scattering
paths within the rotating cradle, the re-design aimed at minimising
structural components and masses of metal near the detectors or
at forward scattering angles. The resulting assembly is illustrated
in figs. 5,6. Of immediate relevance is the lightening of the end
plates which served not only to remove material for the through
neutron beam but also to correct the imbalance created by the
helium detector's housing and mounting collar. Sighting pieces
were provided to fit the central holes for the purpose of cradle
alignment. The cradle has complete freedom of rotation about the
collimator axis on four single width ball bearings which are in
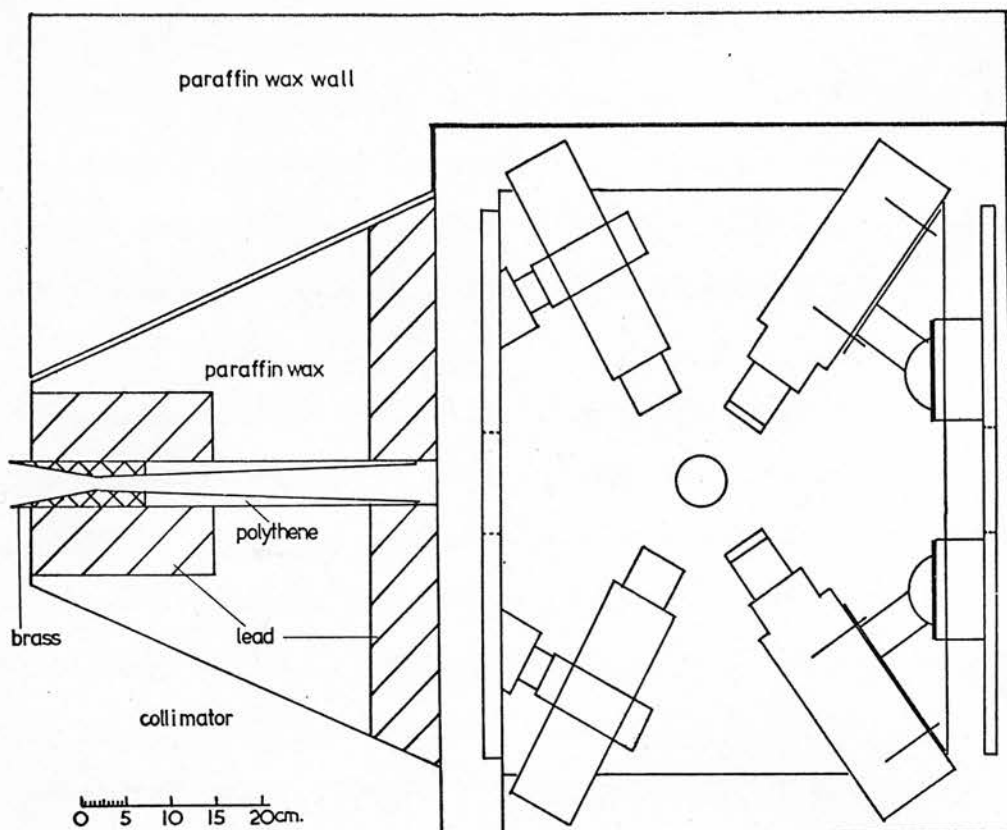
Figure 5. Plan view of polarimeter/collimator indicating shielding materials and scale.
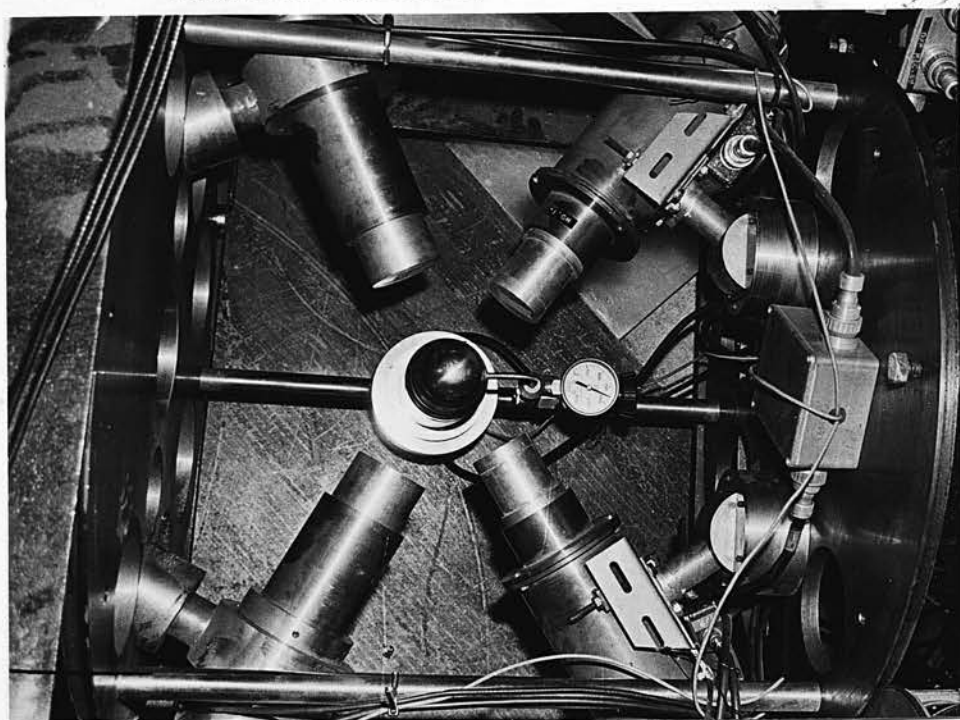
Figure 6. Detail view of rotating polarimeter.

turn secured to a 3 inch angle iron frame attached to the back plate of the collimator. Initial alignment was accomplished by shimming the bars holding the ball bearings. This and the structure of the frame has survived transport and handling on three visits to Harwell without requiring corrective adjustment.

The dimensions of the cradle were a compromise between allowance for both backward and forward scattering side detectors, and the need to keep the overall size within the "shadow" of the collimator. The precise position of the side detectors is dictated by the angles at which the magnitude of the analysing power is largest, at the neutron energies likely to be encountered, and by the acceptable solid angles subtended by the side detectors at the helium cell.

This compact arrangement of detectors facilitated the shielding, and the repositioning of the detectors at various phases of the experiment. The shielding requirements of the system were considerably reduced by the coincidence requirements to allow for random, background events. When necessary, as for instance at higher energy, the shielding was provided by paraffin wax and borated water. The collimator design itself was substantially unaltered from previous work [6] but was tapered and additional lithium fluoride doped paraffin wax was attached in a void beneath. The collimator/polarimeter was castor-mounted and could be rotated on a surface table about a pivot centred immediately below the target.

Alignment of the system was checked optically using inserts in both collimator and polarimeter and could be adjusted by variation of the target position to better than ± 0.25 mm. This procedure was repeated for every alteration of polarimeter angular position or replacement of target.

The automatic running of the experiment necessitated the design of a system for programmed rotation of the polarimeter. The details of this are given elsewhere [7], but basically the operation of the control circuitry was such as to enable movement of the polarimeter about its axis to the next in a selected sequence of positions upon receipt of a logic level transition. This rotation was performed by an eighth horse-power motor geared to one revolution per minute, which was disabled during actual data collection.

2.3.3 The helium scintillation detector.

The basic form of this detector is similar to that designed by Shamu [8]. Developments and tests directed towards more efficient performance are detailed in a later section (4.1). This detector served both as helium scattering sample and detector of helium recoil nuclei.

Figure 7 illustrates the main features of the helium cell. A 3 mm layer of smoked magnesium on the aluminium coated steel shell was used as an internal reflector. This was overcoated with 2 microns of di-phenyl stilbene as wavelength shifter. This aids the reflection of scintillations in the helium-xenon gas mixture used.

stainless
steel

nitrile
'o'ring

perspex
window

ebonite
slip ring

key slot

b

3cm.

0   1   2

stainless
steel

p.t.f.e.
'o'ring

fused silica
window

bolt
holes

a
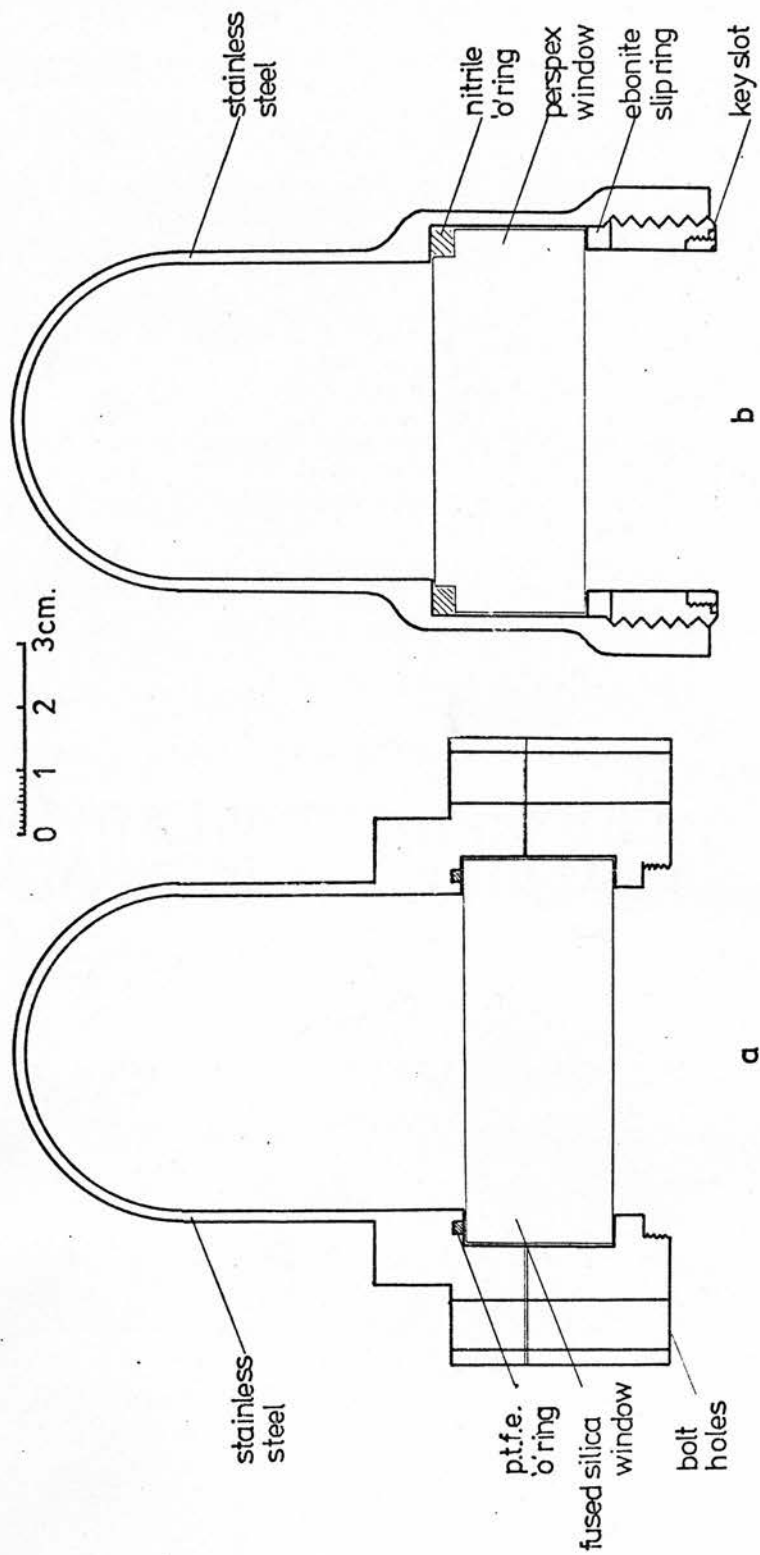
Figure 7. Helium cell a) original version, b) redesigned version.

The gas filling of the helium scintillator includes ten per cent by volume of xenon - a proportion found to be suitable by most experimenters to absorb the helium emission ($< 1000\text{Å}$) and re-emit at longer wavelengths ($> 1470\text{Å}$). The removal of impurities from the system relied chiefly upon flushing and filling with helium after initial bake-out and pump-down with a liquid nitrogen trapped diffusion pump.

The structural design of the scintillator aimed at reducing considerably the material around the window and closure. An internal screw fitting was substituted for the bolting arrangement previously used, and an ebonite ring acted both as a slip-ring and a cushion to the clamped window. A perspex window of 25 mm thickness was substituted for the quartz previously used, since the hydrogenous material should reduce further the number of neutrons mistakenly accepted as helium recoils.

In order to make fullest possible use of the scintillator light output, an RCA 8575 photomultiplier was selected for its high response in the blue end of the spectrum and its low dark current. A series of mishaps led to its replacement with an EMI 9814B, a tube with a similar bialkali photocathode response. The intrinsic resolution of the resulting helium scintillator detector was about 35% for D-d neutrons of 2.9 ± 0.2 MeV.

2.3.4 The scattered neutron detectors.

The neutrons scattered from the helium cell were detected
in one of four detectors, the two backward scattering detectors
as illustrated (fig.8) of a new design, and the forward detectors
being those described previously in connection with the original
polarimeter [6]. The figure shows the magnetic shielding and
internal preamplifiers of the new detectors with NE213
scintillators attached. EMI 9814B phototubes were used for their
good light and time response and in particular because their
physical dimensions best fitted the restricted space available.
The scattered neutrons were incident through the end face of the
bubble-free liquid scintillators, each with active volume dimensions
of 2"ϕx 2" length. The scintillators are rendered bubble-free
by incorporating capillary reservoirs, in the case of the
backward scattering detectors wound round the circumference, but
for the detectors inherited from the earlier configuration, the
capillaries are wound in the end cap.

The mounting arrangements were dictated by consideration of
maximum analysing power of n-alpha scattering and its energy
dependence. For backward scattering reference to Rhea's paper [4]
indicates fair agreement on the phase shifts involved and
insignificant variation in the angular position of the maximum
for neutron energies from 3 to 12 MeV. Accordingly, the supports
were rigidly angled to give a mean angle of scatter equal to
117°_{LAB} and allowed for axial movement. Axial alignment was

Figure 8   Backward scattering detectors with internal preamplifier
and bubble – free scintillator.

checked with dummy detectors and found to coincide with the helium scintillator axis to better than 0.2 mm. In the case of forward scattering, there is considerable disagreement in the reported phase shifts and a marked energy dependence. Therefore the forward detector mountings were designed to allow for clamping at angles from 35° to 75° in order both to check the analysing power and to position the detectors according to the energy dependent minimum in analysing power. The measurements reported were carried out for a scatter angle of 55°. The distance from the helium cell to the scintillator face was adjusted to give a standard deviation in angle of $\pm 8\frac{1}{2}^O$ for each of the four detectors (fig.18 shows the energy distributions corresponding to this angular spread).

For normalisation purposes three sources of data were considered. The total number of routed signals from the helium scintillator was selected as the only quantity useful for normalisation between different polarimeter positions. The target yield monitor (an NE400 Boron/ZnS(Ag) thermal neutron detector encased in 3" of paraffin wax as moderator) and for running on the 5MV Van de Graaff a Faraday Cup charge integrator were used to monitor machine trim and target deterioration.

CHAPTER 3.

ELECTRONICS AND DATA COLLECTION.

3.1 Polarimeter Electronics.

A slow coincidence system was used to derive routing pulses
for the analysis of helium recoils associated with different
neutron scattering events (fig.9).

3.2 Analogue and Logic System.

The system was developed from electronics designed for use
in earlier polarimeter experiments [6]. This served to produce
pulses identifying the detection of neutrons above a certain
energy and to analyse the helium recoil pulses according to the
side detector to which the associated neutron was scattered. By
the use of delayed coincidence it was possible to simulate the
conditions that gave rise to events in which background neutrons
were falsely identified as helium scattered neutrons - consequently
called random coincidences, and correct the 'real' spectra
accordingly.

Certain refinements were executed on this part of the system.
On the analogue side, additional pulse shape discrimination (PSD)
units were constructed for neutron identification for the extra
side detectors. The decision to build these in single width NIM
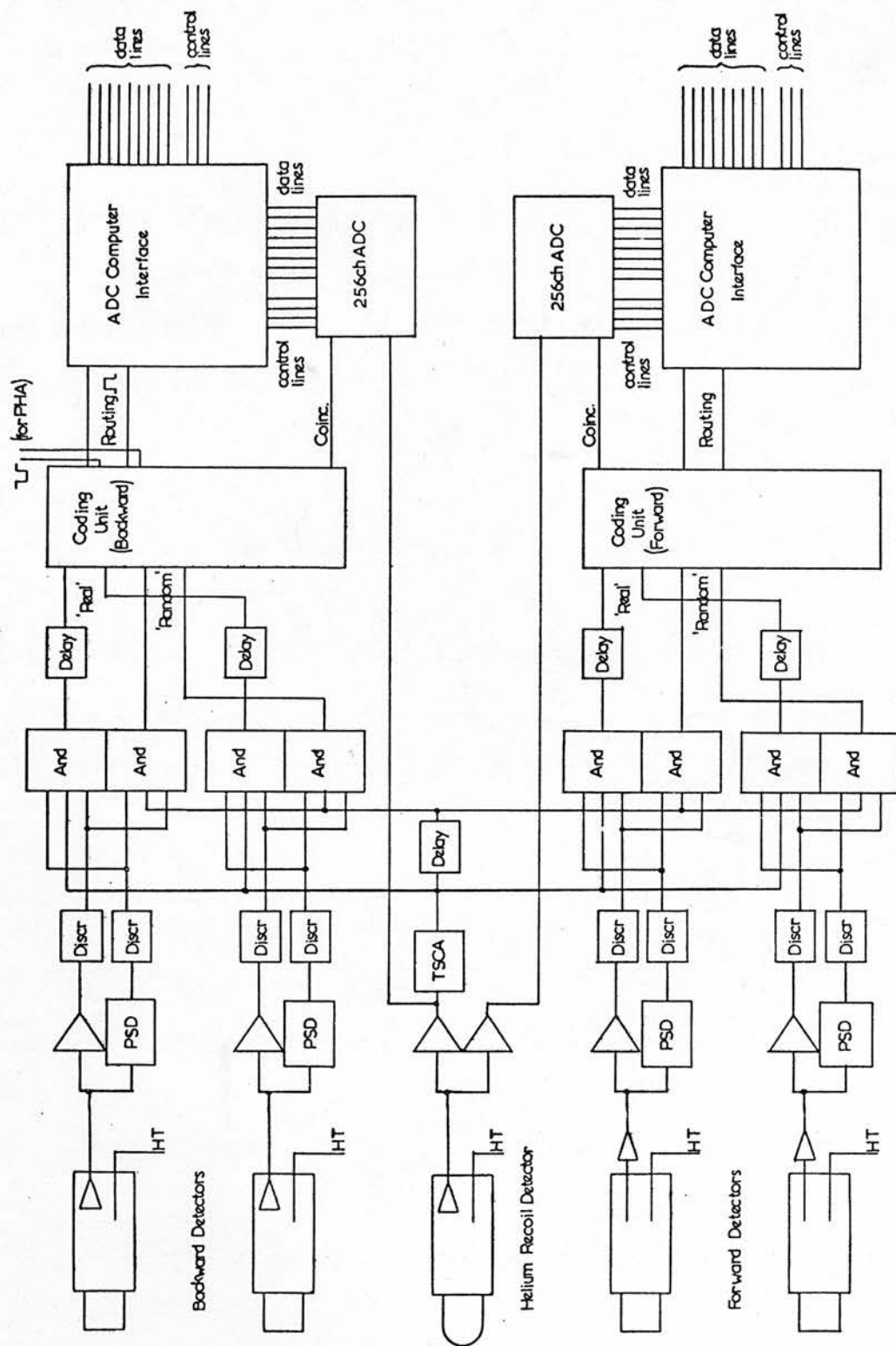
Figure 9. Block diagram of polarimeter electronics.

modules required the elimination of problems associated with layout and incorporating of component changes which produce a marginal improvement in performance (Appendix A3 and fig.10).

With regard to the logic, an attempt was made to reduce the counting of random events by the reduction of resolving times where acceptable. The leading edge discriminator on the helium scintillator amplifier output had provided a time datum with a walk approaching $0.5\mu s$. This was replaced by an Ortec Model 488 Timing Single Channel Analyser which provided a datum at the zero cross-over of the amplifier's bipolar output. This had a time walk of less than 100 ns above a voltage threshold of 100 mv. The time walk associated with the side detectors' discriminators was reduced by modifying the output pulse length to about 150 ns on those discriminators set on the outputs of the PSD units. Though these are leading edge discriminators, when the discrimination level was set between the pulse heights associated with gammas and neutrons it was sufficiently high that they operated with minimal walk. Since the detection of a neutron in any side detector then produced one identifying pulse with temporal precision there was no need for similar improvement to the discriminators associated with energy thresholds.

With these alterations, the time resolution of the system was investigated. The spread in the time of generation of helium recoil/side detector PSD logic pulse coincidences was measured as being about 120 ns with the aid of an Ortec 447 Time to Pulse
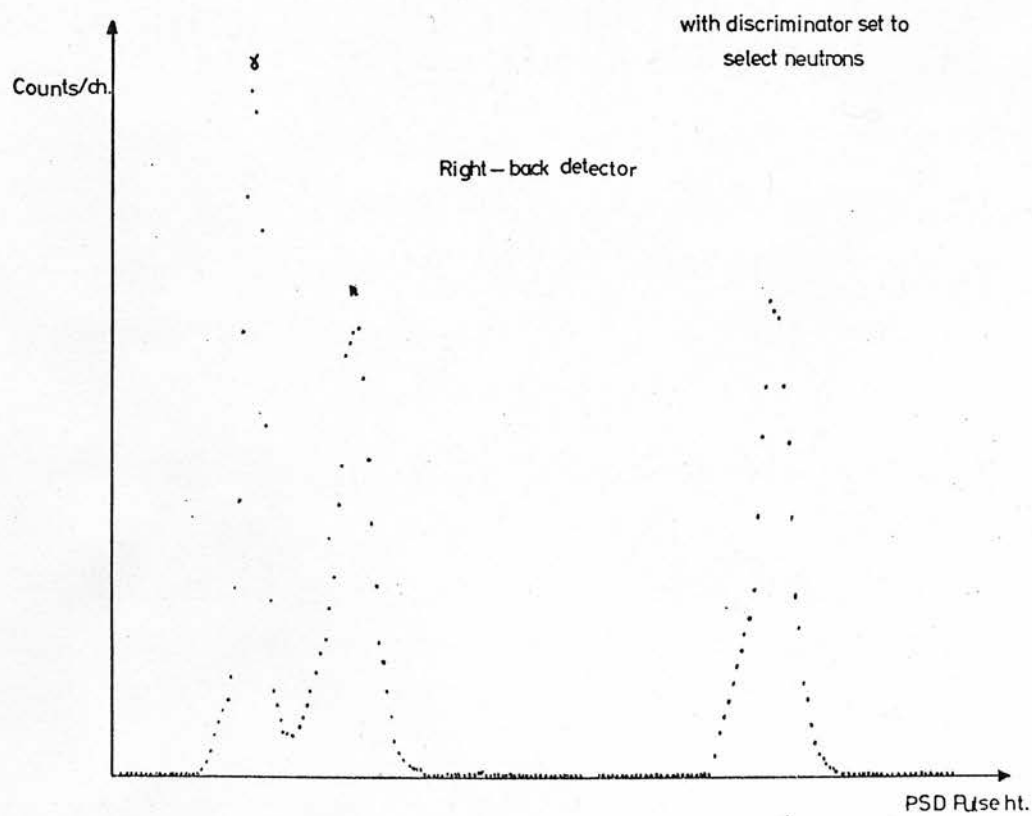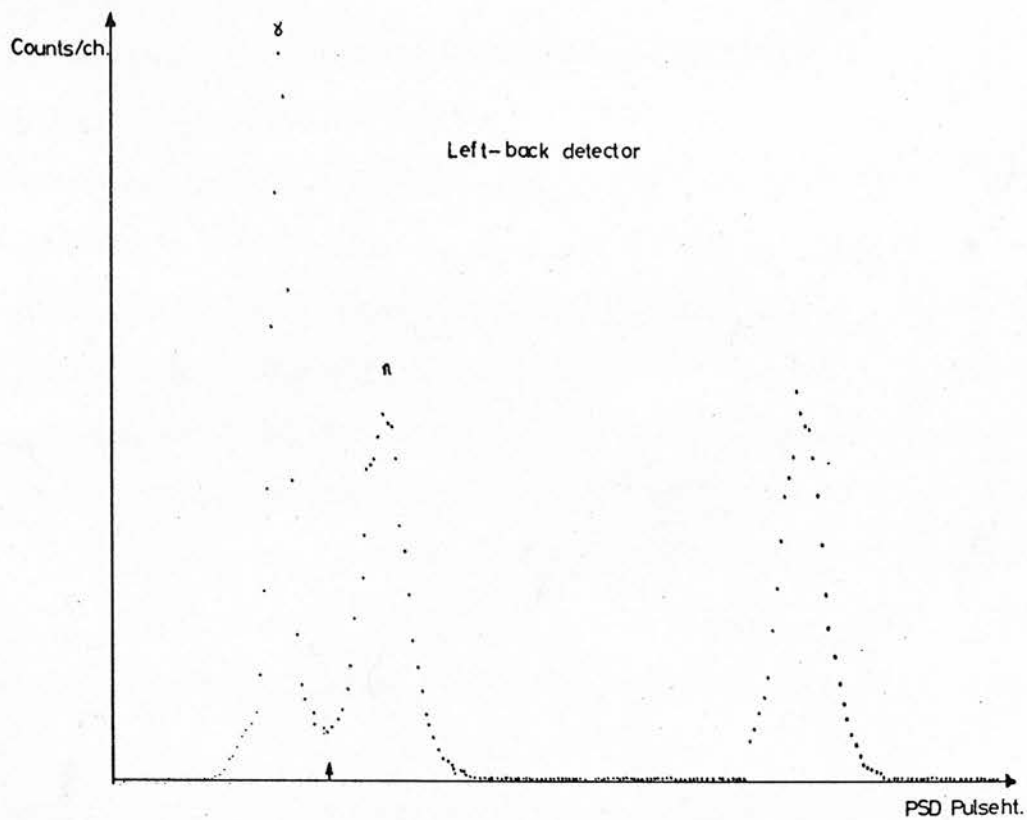
Figure 10. PSD spectra obtained with the backward scattering detectors.

Height Converter (with conversion calibrated at about 0.02v per ns).
The correlation with helium recoil energy was determined by
bidimensional analysis. These observations led to the conclusion
that the high proportion of small pulses - the so-called 'tail'
in the helium recoil spectrum (fig.11) was chiefly associated with
high energy neutrons which were initially forward scattered but
reached the side detector as a result of a second scattering in
the structure of the helium cell. The occurrence of extreme back
scattering of neutrons which then reached a side detector by a
subsequent unintended scattering was identified with a slight
broadening of the helium recoil spectrum on the high energy side.

The events contributing adversely to the low energy part of
the recoil spectrum may be ignored by critical adjustment of delays
since the associated high energy scattered neutrons give rise to
particularly prompt PSD logic pulses. The contribution to the
high energy part of the spectrum may be rejected by appropriate
setting of linear biases to reject the weakest neutrons. These
adjustments gave rise to a backward scattering recoil spectrum
with a peak-to-valley of 7 : 1 and 33% resolution as against
4 : 1 and 38% under previous best conditions. In the case of forward
scattering, it was found more difficult to effect this sort of
improvement probably because there is less distinction between
the desired angle of scattering and slightly diverted neutrons,
and the solid angle subtended by the forward scattering detector
corresponds to a much wider range of neutron energies (fig.18).
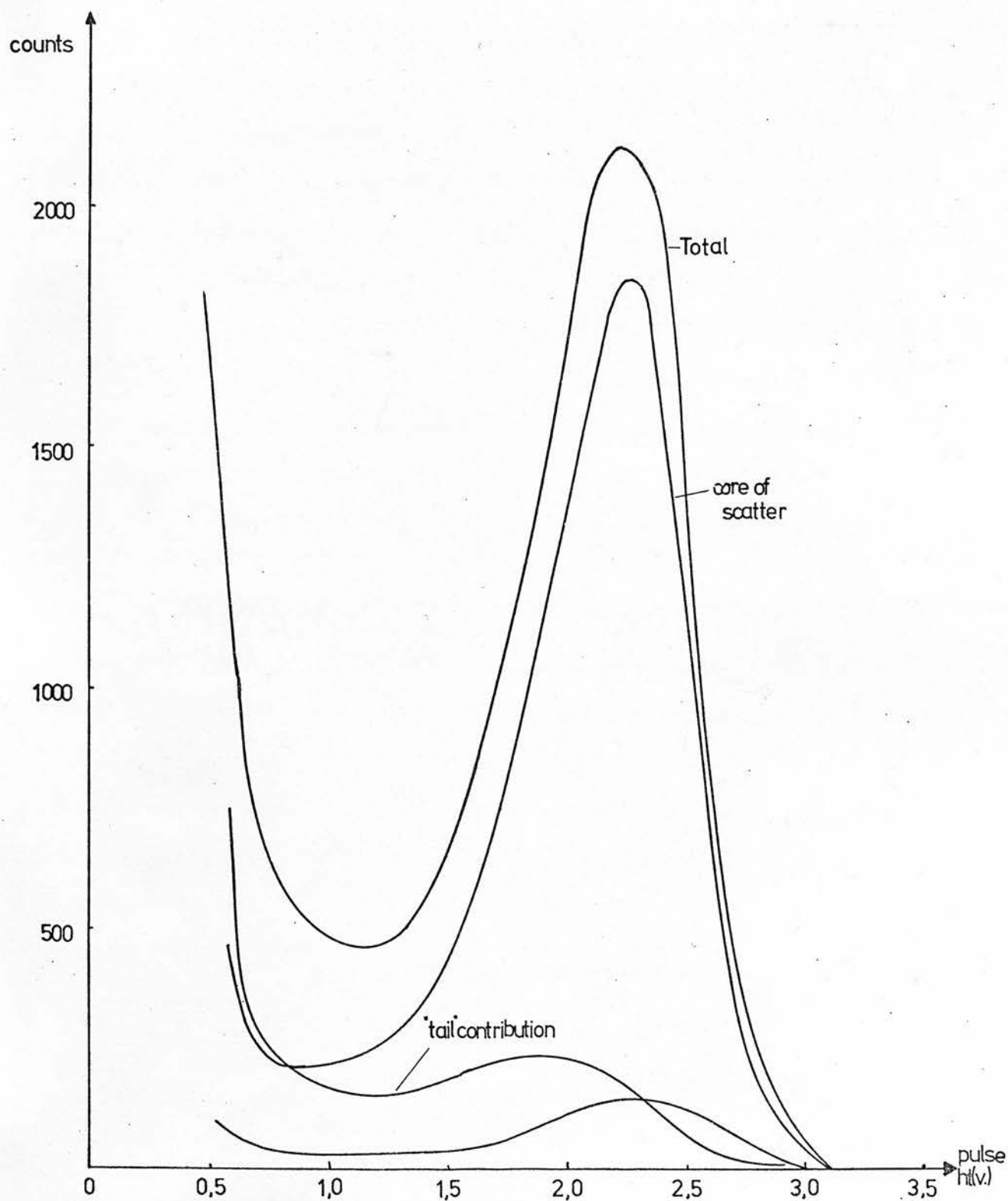
Figure 11. Breakdown of contributions to the helium recoil spectrum.

3.3 Interfacing and Routing.

To satisfy the routing requirements of the analysers used
with this system a two bit code must be created so that detection
of a neutron from a 'real' or random event in a particular side
detector results in correctly allocating a helium recoil pulse
to a subgroup of memory. Two coding units constructed as modules
of ISEP construction already existed and produced negative
routing pulses as required by LABEN analysers. This system was
extended to produce positive logic pulses with delays adjustable
to $12\mu s$, and a duplicate system incorporated to cope with the
similar routing requirements of the second pair of side detectors
(Appendix A4).

For simultaneous analysis with both backward and forward
scattering angles, two 256 channel LABEN Analogue-to-Digital
Converters (ADC's) of NIM modular design were used. The ADC's
operated independently, digitising the output from separately
amplified copies of the helium recoil pulse. The separate forward
and backward scattering logic electronics were used to derive
pulses uniquely identifying either kind of event and these were
used to gate the operation of the ADC's. The recoils associated
with forward and backward scattering had a relative magnitude of
approximately 2 : 5 and the amplifiers were adjusted accordingly
so that the dynamic range accepted at each ADC was similar.

The ADC's were interfaced for direct memory access to a PDP11/45. Interface units already in existence were adapted for this purpose. These units were basically designed for parallel line driving of nine bit words using common emitter buffer stages. For their present purpose the two routing pulses were adopted in each case as the most significant bits of the data word, additional logic being incorporated to hold the routing levels until transfer was complete (Appendix A5).

Since the processes of event identification and analysis was completely separate for the two angles of scatter from the helium cell, data collection at only one scattering angle (normally the backward angle) simply used half the system. When using a multi-channel analyser, spectra can only be collected for one angle of scatter, gating and routing pulses being applied in a manner similar to that for the interfaced ADC. Output from this device was by means of a High Speed Tape Punch.

3.4 Data logging system.

For setting-up purposes and normal running it was desirable to have scaler outputs associated with different events as well as collimated and target neutron yields. As the reliability of the data collection systems became proven, the scaler readings associated with the side detectors were increasingly redundant except for monitoring purposes; however, a record of total yields was useful for normalisation purposes.

-17-

A quad (4-unit) scaler module was developed to operate adjacent to the coding unit previously mentioned. This was designed specifically for the neutron polarization experiment but was accessible through the coding unit for any source of TTL/RTL pulses. Additional scalers were built in single width NIM modules and stop/start circuits were incorporated in all scalers to enable control of counting and resetting at the dictation of the computer or analyser supervising the experiment (Appendix A6).

With the adoption of fully automated running some means of automatic data logging became necessary. Accordingly, a line printer system was designed to be compatible with the Nuclear Enterprises range of scalers and timers (Appendix A7). The control and command signals were decided upon with consideration of pending International Electrotechnical Commission recommendations [9]. Data transfer is by 4 bit x 6 digit parallel data line and control by 7 lines with special separate wiring for interfacing to the quad scaler. This latter requires a 4 bit x 5 digit parallel data line plus 5 control lines. The quad scaler contains an additional blind 'run number' scaler, initialisable and incremented at the commencement of each run.

Provision was made for a flexible system of control. The stopping of the scalers is simultaneous with commencement of printing and may be instigated by manual push-button, an internal presettable timer (range 1×10^1 to 9×10^4 secs), or by an externally

-18-

sourced voltage (switch selectable to cope with positive or negative voltage levels for stop). A three-way switch allows selection of the source which will stop the scalers and start printing. There is an almost identical arrangement for the 'recycling' of the scalers, except that the selection of 'auto start' with the separate three-way recycle switch starts the scalers immediately the print-out has finished.

The line printer unit was constructed in a triple width NIM module but was separately powered so that it could be operated free standing if required. TTL integrated circuitry was used throughout and multiplexing techniques were applied to reduce power consumption in the scalers. The resulting system was compact and portable.

CHAPTER 4.

THE HELIUM SCINTILLATOR.

4.1 Tests on the scintillator.

The anomalies in previous polarization values have been attributed to incorrect interpretation of helium recoil spectra. Attempts have been made at computer aided fits to the peak [10] and the low energy tail [11] of typical spectra. These fits contain adjustable parameters to allow appropriate weighting of the various features associated with resolution and spurious scattering effects.

Suggestions concerning the relation between the helium scintillator's orientation and resulting recoil spectra have already been put forward [11]. In order to investigate these ideas, various positionings of detectors were improvised. Placing the helium detector vertical reduced the tail but failed to significantly affect the resolution or peak-to-valley ratio of the helium recoil peak (fig.12). With the aid of a program designed to simulate the spurious scattering processes possible, this was interpreted as indicating a reduction of events in which forward scattered neutrons were deviated from their path by the surrounds of the scintillator and consequently identified as backward scattering events. The lack of improvement in the peak-to-valley ratio was attributed to a failure to reduce the number
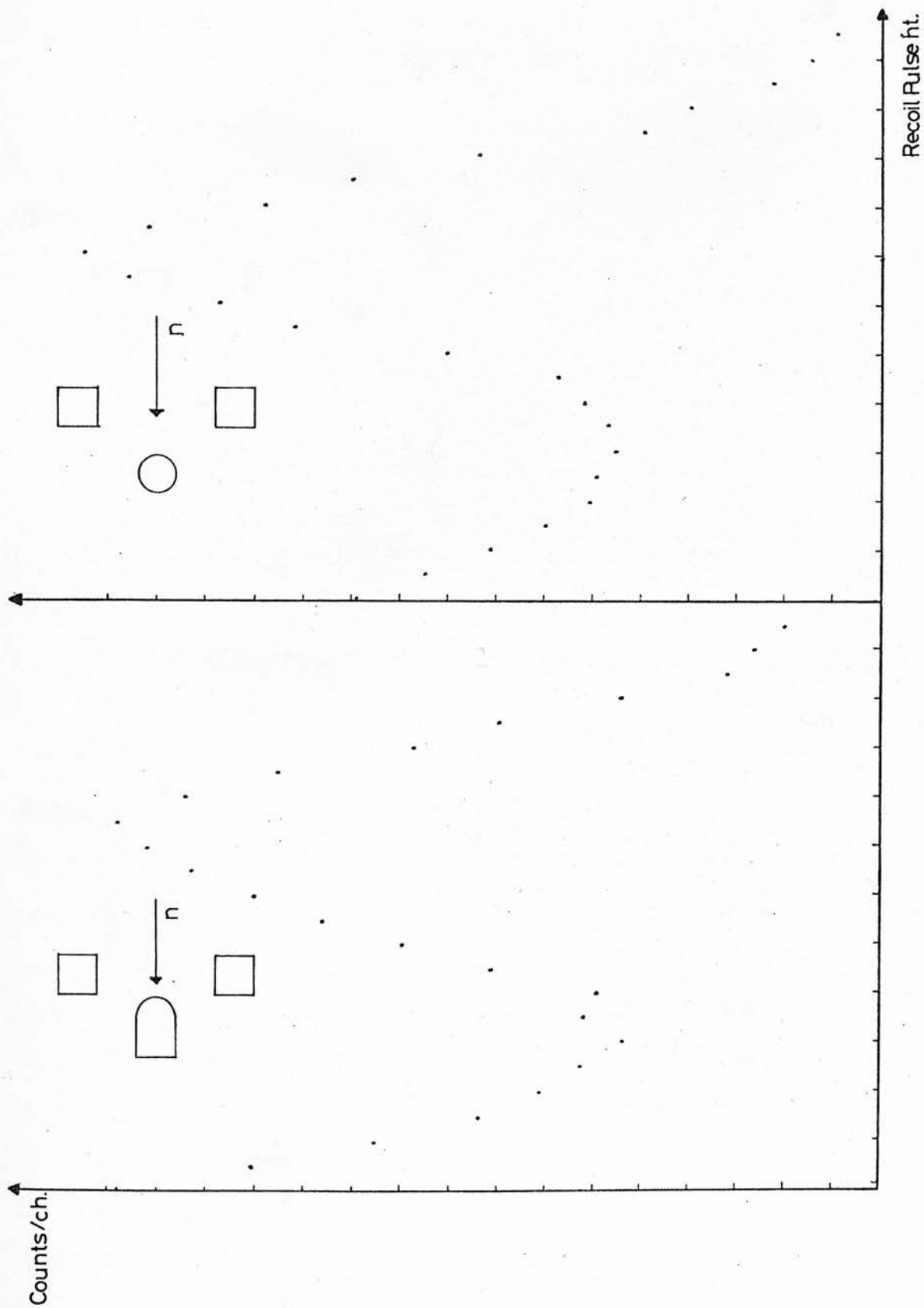
Figure 12. Comparison of coincidence recoil spectra for two orientations of the helium cell.

of neutrons interacting with the surrounds first and then being
back-scattered with a fairly strong associated helium recoil.

It was hoped that the reduction of metal construction contiguous
to the helium volume, the increase in pressure of the helium and
the replacement of the quartz window by hydrogenous material would
conspire to reduce these effects. The density of the scatterer,
helium, could be doubled if use is made of the maximum commercially
available gas pressure (2000 psi). While the use of liquid helium
increases the density and effective scattering by a further factor
of five, the cryostat and associated hardware introduce potential
scattering materials apart from the complications associated with
precession electromagnets. Such a further increase in density
also makes multiple scattering corrections important and can
thereby introduce further uncertainties into the results (Section 6.1,31)

The redesigned scintillator overcomes several structural
weaknesses of the previous versions (figs.7,13). Any shaping to
improve the light collection efficiency would have compromised
the requirements of volume and strength. Substituting perspex
for the previously used Spectrosil quartz window produced little
noticeable difference (fig.14) once the system gain is adjusted
for the poorer transmission of the former. The perspex has an
optical cut-off at 3000Å as opposed to 1700Å for Spectrosil
and an attempt was made to compensate for the poorer transmission
by the use of wavelength shifters. The most efficient and
frequently used is pp'-diphenyl stilbene and reference to

Fig. 13 Comparison of the original and re-designed helium scintillators.
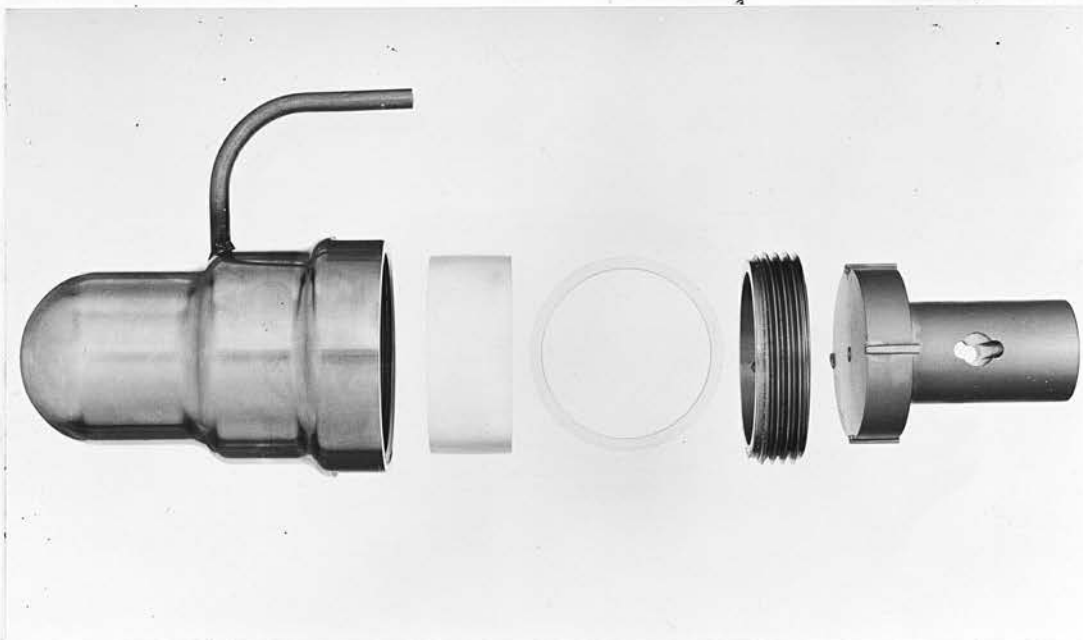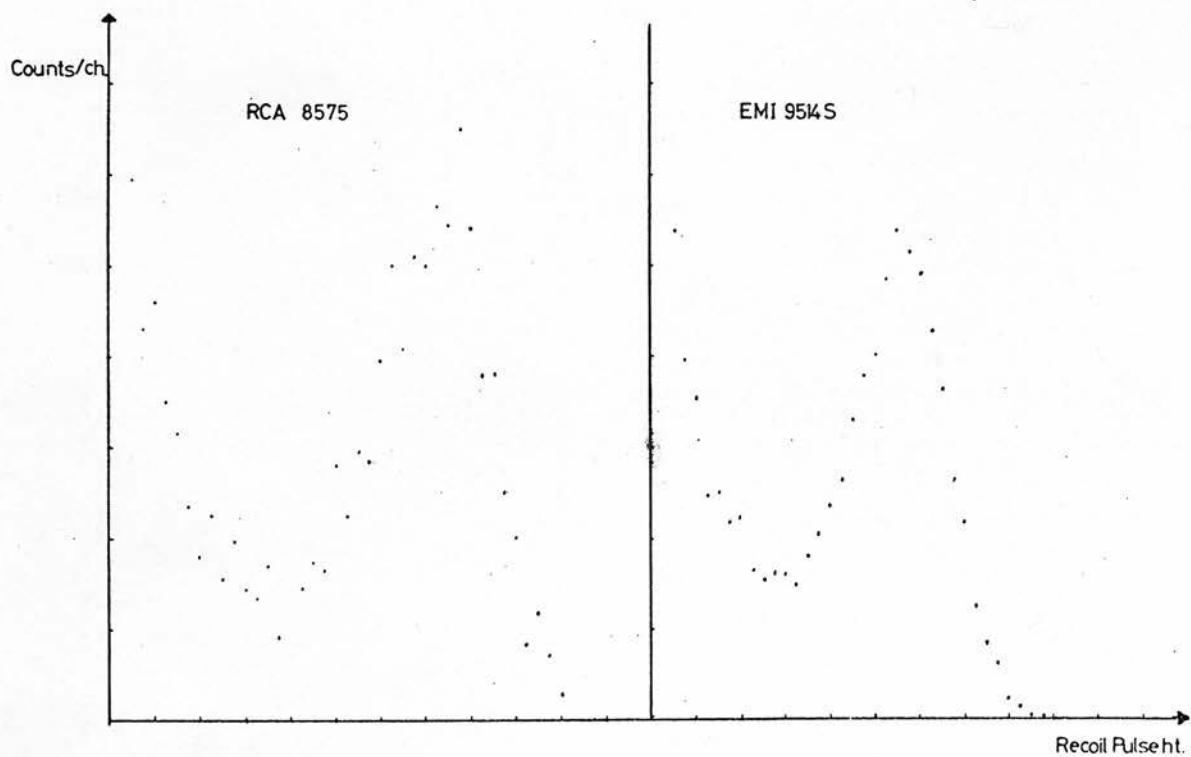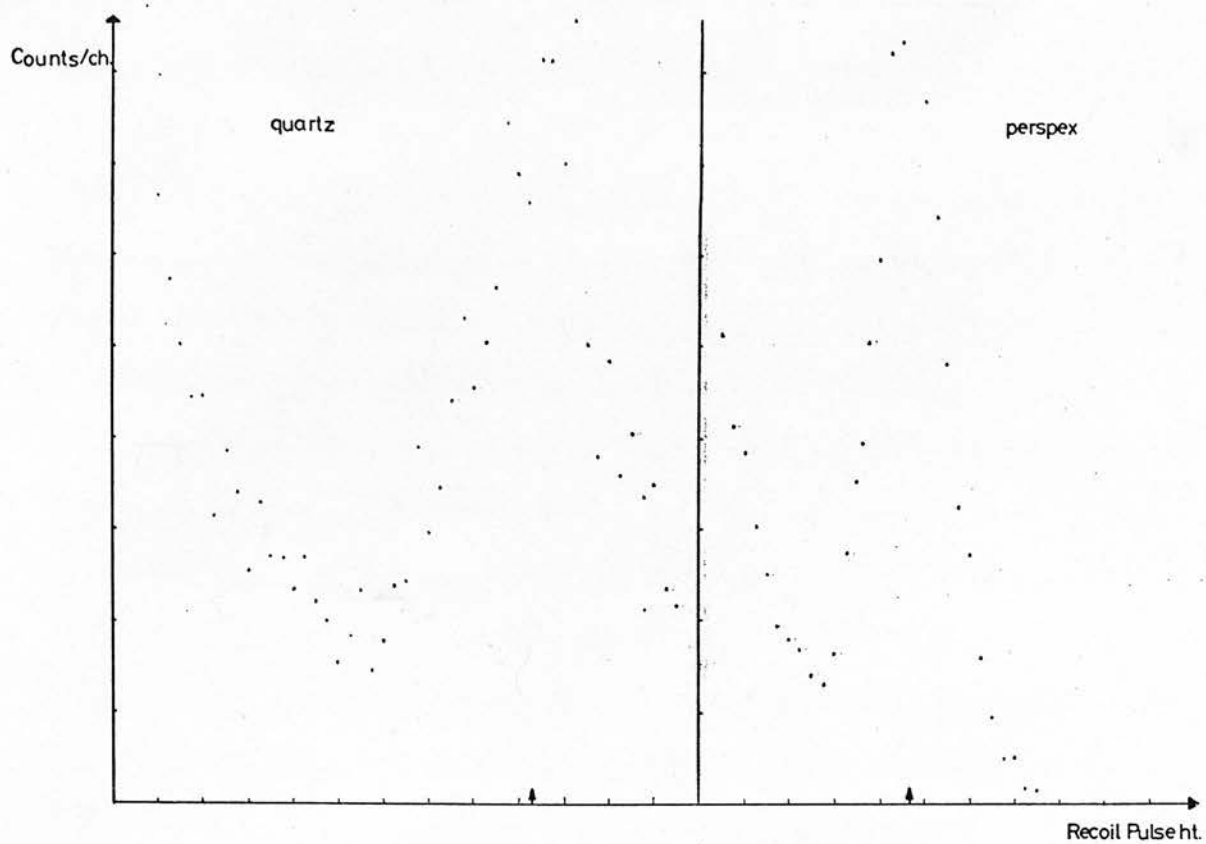
Figure 14. Comparison of performance with different windows and
different photomultipliers.

Berlman's [12] list of emission spectra led to the selection of 2,5 - Di(2-napthyl) - 1,3,4 - oxadiazole(β -NND) as a possible alternative. The coating thickness (2 microns) is a compromise between efficiency of conversion and attenuation. The use of these materials led to a staggering loss of light output (about a factor of 10) which is attributed to poisoning of the wavelength shifter [13] by the known outgassing tendencies of perspex. Of more promise is the effect of an antireflection and sealing layer of magnesium fluoride (900Å thick). This produced an apparent 5% to 10% improvement in light output but this is similar to the variation obtained between different gas fillings and so was considered inconclusive. The solution to the outgassing problems associated with perspex involve the use of a protective quartz faceplate [14] but the complications of sealing and seating such a perspex-quartz combination in the high pressure cell outweighed the advantages of longer intervals between flushing and refilling with fresh gas.

4.2 Beam profiles.

The extent to which neutrons interact with the material of the helium scintillator may be judged from the distortion of beam profiles as observed from behind the scintillator. Beam profiles also serve to illustrate the degree to which the collimator inserts define the dimensions of the neutron beam.

Several points arose out of the measurements of beam profile. The use of a 3mm thick stilbene crystal allowed discrete and detailed analysis of the neutron flux variation and the helium scintillator itself allowed a means of normalising against changes in yield and accelerator conditions. Repetition of a sequence of measurements for various orientations of the helium cell enabled a complete picture of the beam profile to be gained and the figures illustrate the marked attenuation of flux associated with the earlier cell and its heavy collar. The figures (figs, 15,16) show the cell outline projected onto the plane in which the stilbene detector scanned the beam. With the present version of the cell it appeared possible to adjust the cell height so that the attenuation of the neutron beam in the collar was comparable with that in the dome of the cell.

To assess the attenuation of neutrons due to the helium – xenon mixture alone the pressure in the cell was reduced by a factor of two. In this way a ten per cent flux increase was observed in the stilbene detector for a reduction in pressure of 1000 psi while still being able to normalise data. A profile with the helium cell removed gave an increase in flux of 30% at the stilbene detector. This indicates an attenuation of approximately 10% associated with the shell.

Further observations were made for a variety of positions of the throated collimator inserts. These measurements established that a line-of-sight interpretation of the area of neutron irradiation was valid. The solid angle defined by the collimator
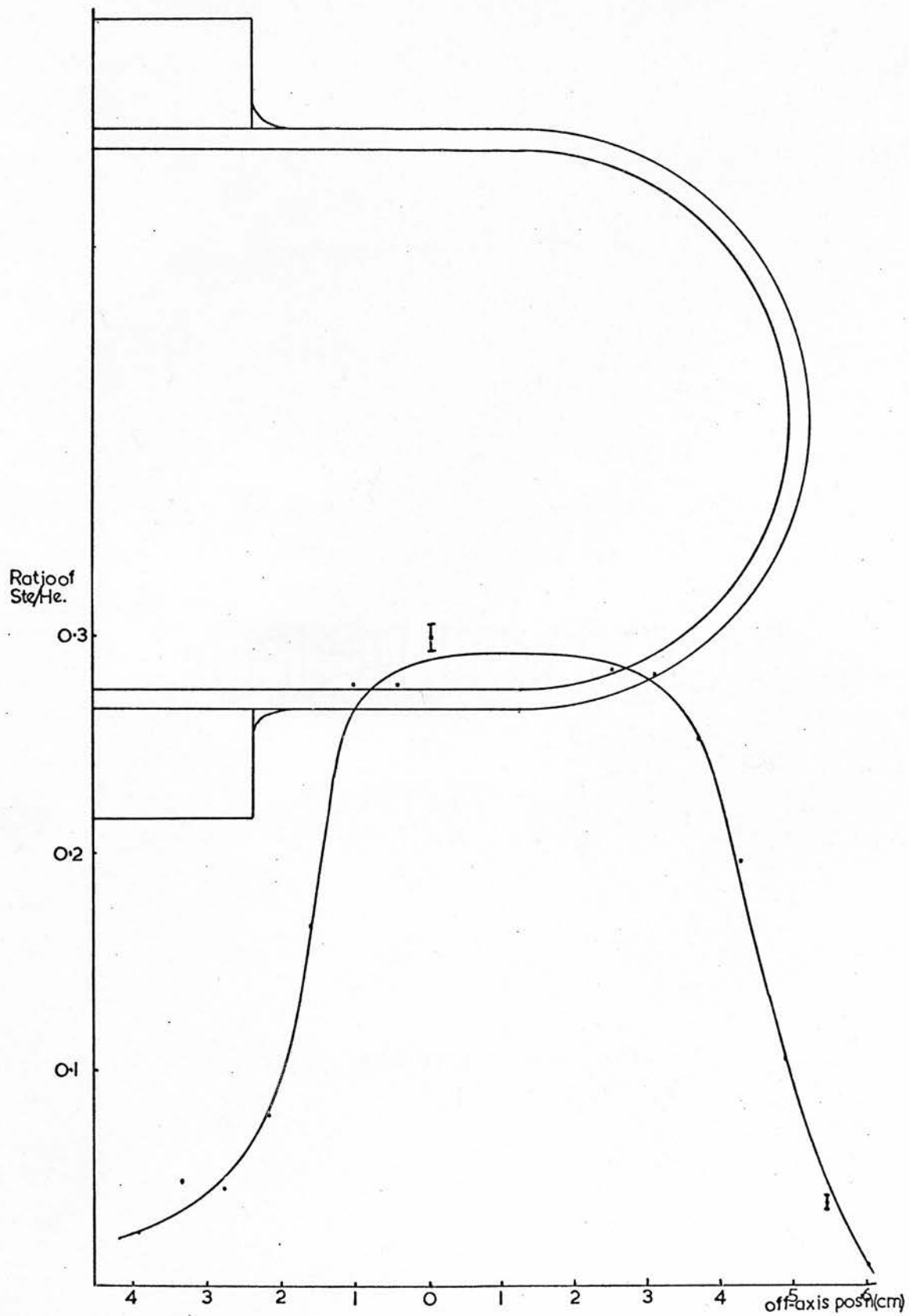
Figure 15. Beam profile for the original helium cell.
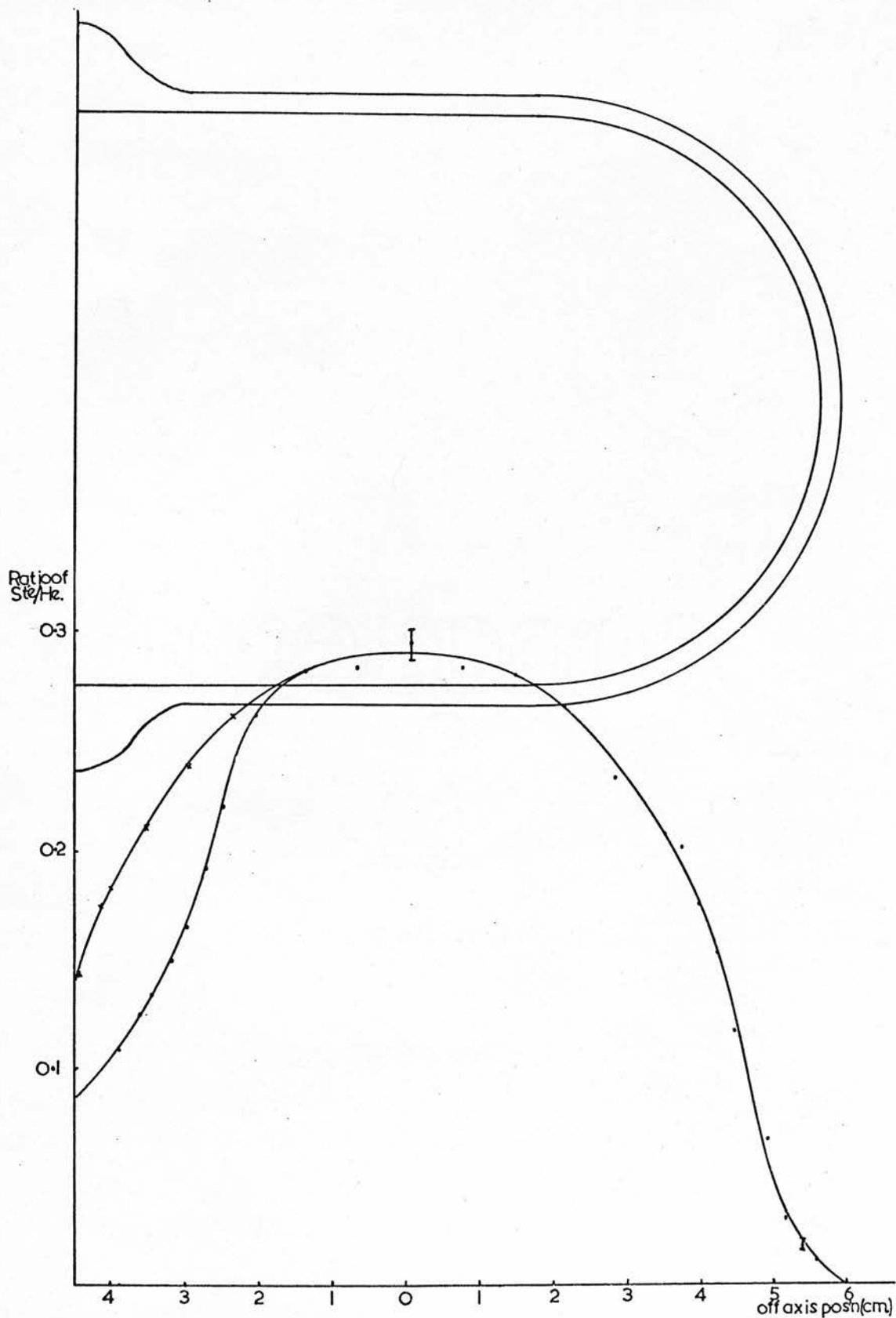
Figure 16. Beam profile for the redesigned helium cell showing the peak
normalised profile without helium cell.

throat corresponded precisely with the half maximum flux points on the corresponding beam profiles (fig.17).

4.3 Experimental implications.

These observations imply that the design and configuration of the new system was a basic improvement on the original polarimeter; however the system involved certain compromises in performance inevitable to attain an adequate counting rate in the experiment. The side detectors have been positioned as previously described so that mean solid angles of about 17° were subtended at the centre of the helium cell. For the backward scattering detectors this solid angle for neutron detection results in the acceptance of a corresponding range of helium recoil energies; this contributes about 15% to the resolution in the helium spectrum. However, for forward scattering neutrons, the spread of recoil energies contributes about 65% to the resolution. These effects are illustrated in fig. 18 where E_o represents the incident neutron energy and E_n, E_{he} the energies of the scattering products. Reaction dependent effects contribute to the resolution to a smaller extent: the range of neutron energies associated with the target thickness (over the range of experimental conditions encountered) and the solid angle subtended at the target affect the resolution by 4% to 5%.
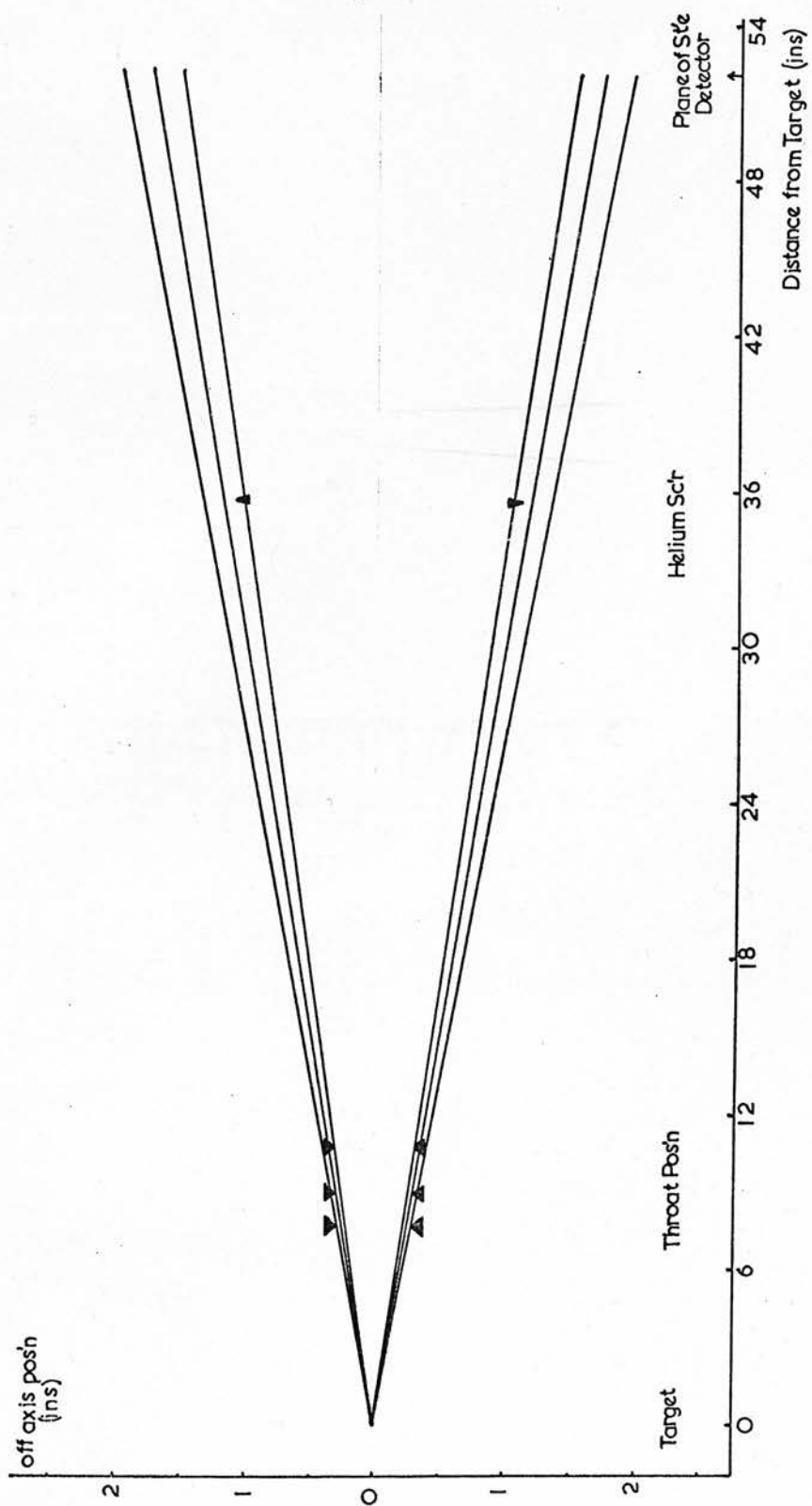
Figure 17. Illustration of the solid angle defined by the collimator throat.
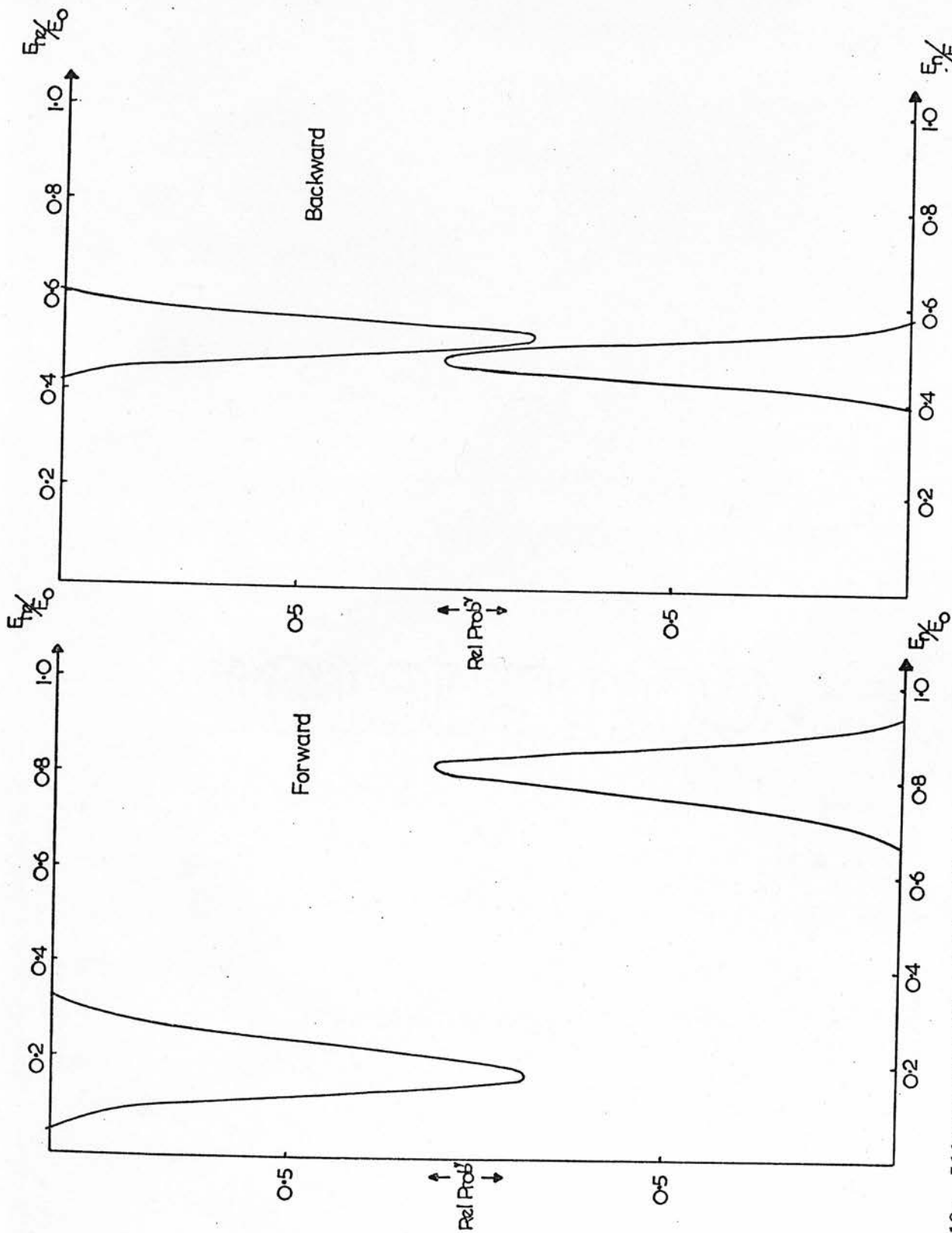
Figure 18. Illustration of relationship between neutron and recoil helium for forward and backward scattering indicating the resolution effect associated with the solid angles subtended by the side detectors.

CHAPTER 5.

REDUCTION AND CORRECTION PROCEDURES FOR
NEUTRON POLARIZATION DATA.

5.1 Computer file handling.

The approach to file handling was directed by certain
experimental constraints. As previously noted, data from the
polarimeter was accumulated with 'left' and 'right' detectors
interchanged for alternate runs. This allows their different
efficiencies to be averaged out, using the total number of
recoils in either position to normalise. Consideration of the
stability of the accelerator and electronics decided the run
time - normally 2000 or 4000 seconds. A means of determining
the statistical accuracy achieved as the experiment progressed
had also to be provided.

A program was devised to supervise the allocation of
memory, and to simplify later analysis by the creation of
summing files that accumulated separately the spectra collected
for different orientations of the polarimeter. In this way
decisions about sets of data collected under different machine
conditions or after changes in helium scintillator response
could be postponed. Further programs enabled comparisons of
spectra and integration between selected limits for normalisation
purposes. The summation of 'real' spectra and the subtraction

of spectra simulating the effect of chance coincidences were all performed by specially developed subprograms.

Further analysis was performed with little assistance from the computer. Extreme tail corrections were drawn in free-hand on corrected spectra. The figure (fig. 19) illustrates a typical spectrum with the left-right asymmetry calculated for consecutive strips from the 'valley' over the extent of the peak. It has been argued [10] that the tail should have zero asymmetry and so plausible tail extrapolations should give asymmetry values over the peak which form a set self-consistent within their statistical errors. The selection of part of the recoil spectrum can thus be justified, rejecting those parts of the spectrum where the statistics are poor and inaccuracies in tail correction most telling.

This analysis led to a 'measured' asymmetry with an associated error which is part statistical and part representing the spread of asymmetry values for extreme but acceptable tail corrections.

5.2 Corrections to the measured asymmetries.

Besides the graphically determined tail correction there were second order effects to be taken into account. Multiple scattering within the helium gas contributes a correction of the order of 1% [6]. Effects associated with background reactions

-26-
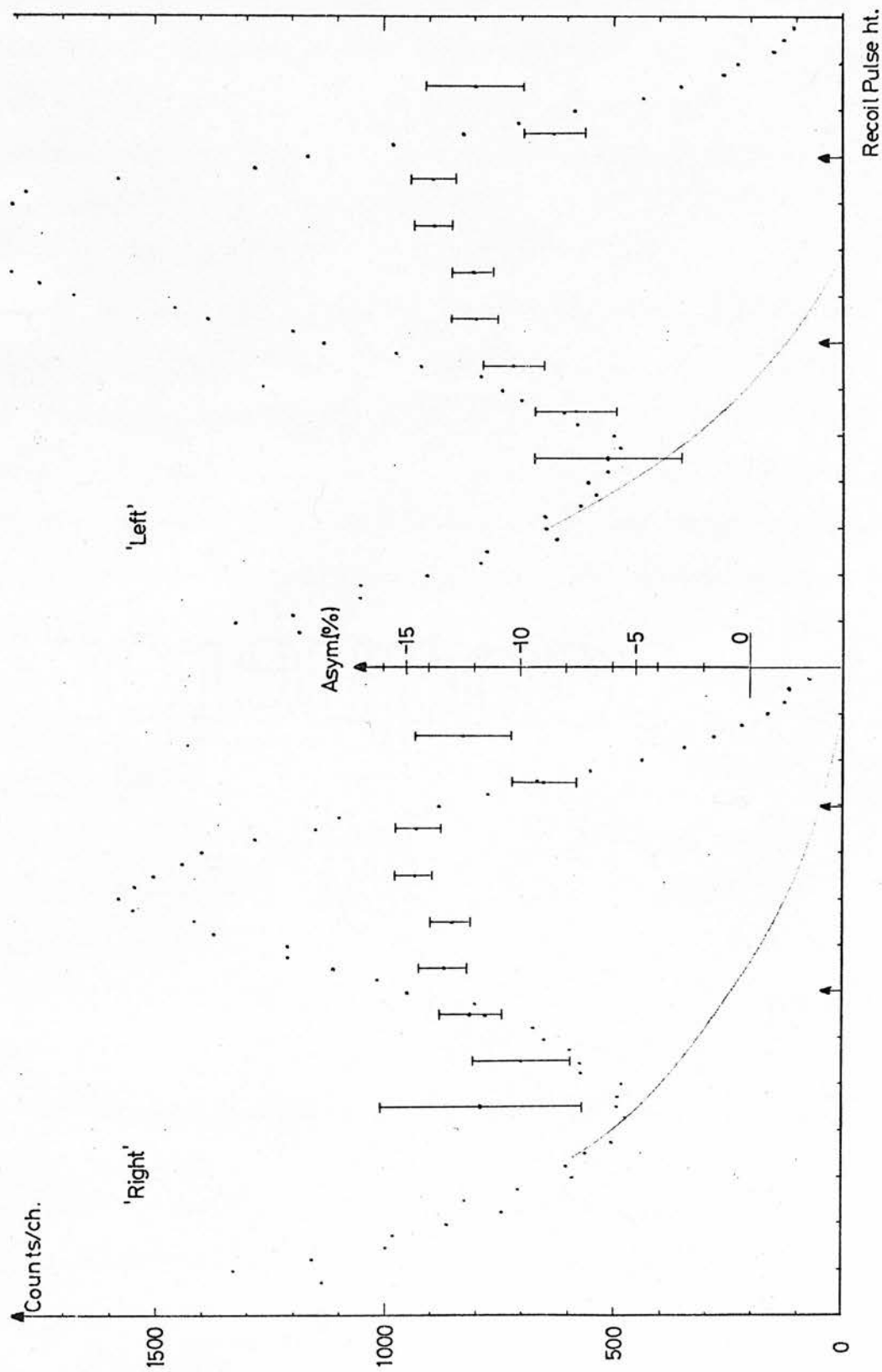
Figure 19. Example of recoil spectra with asymmetries plotted for two extreme tail corrections.

only became of any significance for incident deuteron energies in excess of 3.5 MeV. Runs with dummy targets normalised by the use of integrated charge collected were used to correct the 'real' spectra by subtraction in a manner similar to that used in 'random' or chance spectrum removal.

Taking account of the finite geometry in the experiment involved firstly allowance for the variation of the reaction differential cross-section over the range of angles subtended by the helium cell, and secondly an assessment of the distribution of n-alpha scattering angles, and corresponding range of helium recoil energies for the solid angle the side detectors subtend at the helium cell. A program to calculate the correction for reaction differential cross-section has already been described [6] and requires as input only an estimate of the reaction polarization and a precise value for the change in differential cross-section across the diameter of the cell. Reference has been made to the configuration of the detectors and its consequences (Section 4.3).

The techniques for simulating the scattering and the consequent determination of mean analysing powers are detailed in the enclosed report [15]. This investigation was extended to determine the angular distribution of scatter for the various detector configurations concerned, and the relative importance of slight variations in these distributions. Fig. 3 of this report illustrates the agreement between 2-D and 3-D simulated

constructions of angular distribution implying that the
approximations involved in the simpler modelling of the situation
were negligible. These distributions are plotted without
inclusion of energy dependent factors but are shown against the
analysing power curves at 3 MeV as derived by two research groups
(Wisconsin [16] and Duke [17]). From this it may be concluded that
the original polarimeter came closer to selecting the maximum
analysing power, but in practice this made an insignificant
difference to the system's ability to detect asymmetries in
neutron scattering.

The investigation of mean analysing power is taken a stage
further in figure 4 of this report. This explores the variation
of the uncorrected mean analysing power at backward angles as a
function of neutron energy for the two polarimeters. The heavy
curve illustrated in both cases takes account of the azimuthal
angle dependence (as $\cos \emptyset$) of the analysing power which in
general approaches a two per cent correction to $A(\theta)$.

The determination of the false asymmetry with the variation
of the reaction differential cross-section is an integral part
of the analysing power program [6]. The cross-sections of
Liskien [1] were taken as a reliable source and the computed
corrections to the asymmetry were of the order of or less than
half a per cent for all but the 5.5 MeV runs.

5.3 Determination of target effects.

Throughout these measurements the target thickness was selected to give a sensibly discrete observation as regards deuteron energy. The actual range of energies corresponding to the target thickness was derived from the stopping cross - sections of Coon [18], due account being taken for the angle at which the deuteron beam met the target. The mean energy of deuteron used in calculations of neutron energies produced was derived with reference to the reaction yield curves of Seagrave [19] and the polarization measurements are given with these corrected mean deuteron energies and a range corresponding to their energy spread. Taking a typical situation in which the incident neutron energy is 500 keV, the target thickness is selected to give a 95 keV range in energy and the yield curves imply a mean deuteron energy of 460 keV. The spread in neutrons produced at 45° LAB from this reaction is also about 95 keV but the range of angles subtended by the helium cell superimposes a further 40 keV spread in the energy of incident neutrons.

The variation in the reaction differential cross-section across the helium cell has been mentioned as an appreciable correction to the measured asymmetries. The figure (fig. 20) illustrates that this function has a positive gradient even down to 40° LAB at the higher energies investigated and due care should be taken of the manner in which this correction is applied.
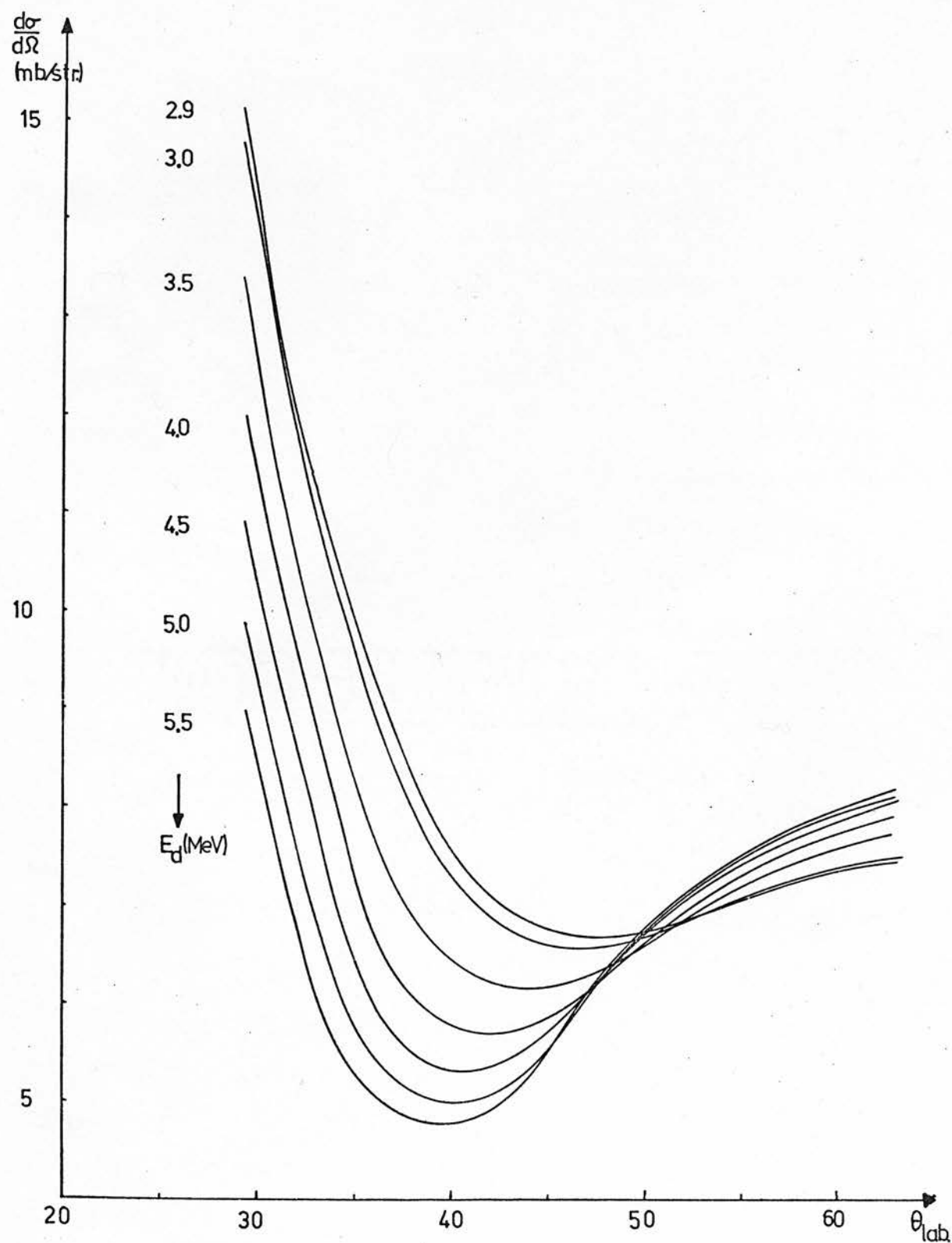
Fig. 20 Differential cross-section in the LAB-frame for the D(d,n)³He reaction [1].

CHAPTER 6.

EXPERIMENTAL RESULTS AND INTERPRETATION.

6.1 High energy data.

As mentioned in the introduction, polarization measurements
in the 4 to 6 MeV region are scarce and basically show
discrepancies between the data from the Duke group [27] and the
recent results of Smith and Thornton [28]. The measurements
performed by the Edinburgh group using the 5 MeV Van de Graaff
at A.E.R.E. Harwell should resolve these discrepancies.

As illustrated (fig. 21) the trend of measurements presently
reported agrees with the trend of the Duke group observations and
implies a natural extrapolation to their measurements at higher
energies [29, 30]. The polarization reported for 4 MeV incident
deuteron energy at 45° LAB (Table 1) is an exception to this
trend. Repetition and independent analysis of the data indicated
that the results were reproducible to within their experimental
error limits and this apparent discontinuity remains unexplained.
This measurement alone falls in with the trend reported by Smith
and Thornton [28] which is consistently smaller throughout. While
their polarization values may satisfactorily be extrapolated to
agree with those of the Duke group, including the re-measurement
by Spalek et al [30], they imply that at 45° LAB the polarization
changes sign below 5 MeV deuteron energy whereas the presently

Fig. 21a Polarization of neutrons from the ^{2}H(d,n)^{3}He reaction as a function of incident deuteron energy for laboratory angles of about 45° (symbols as in [2]) with additional recent measurements.
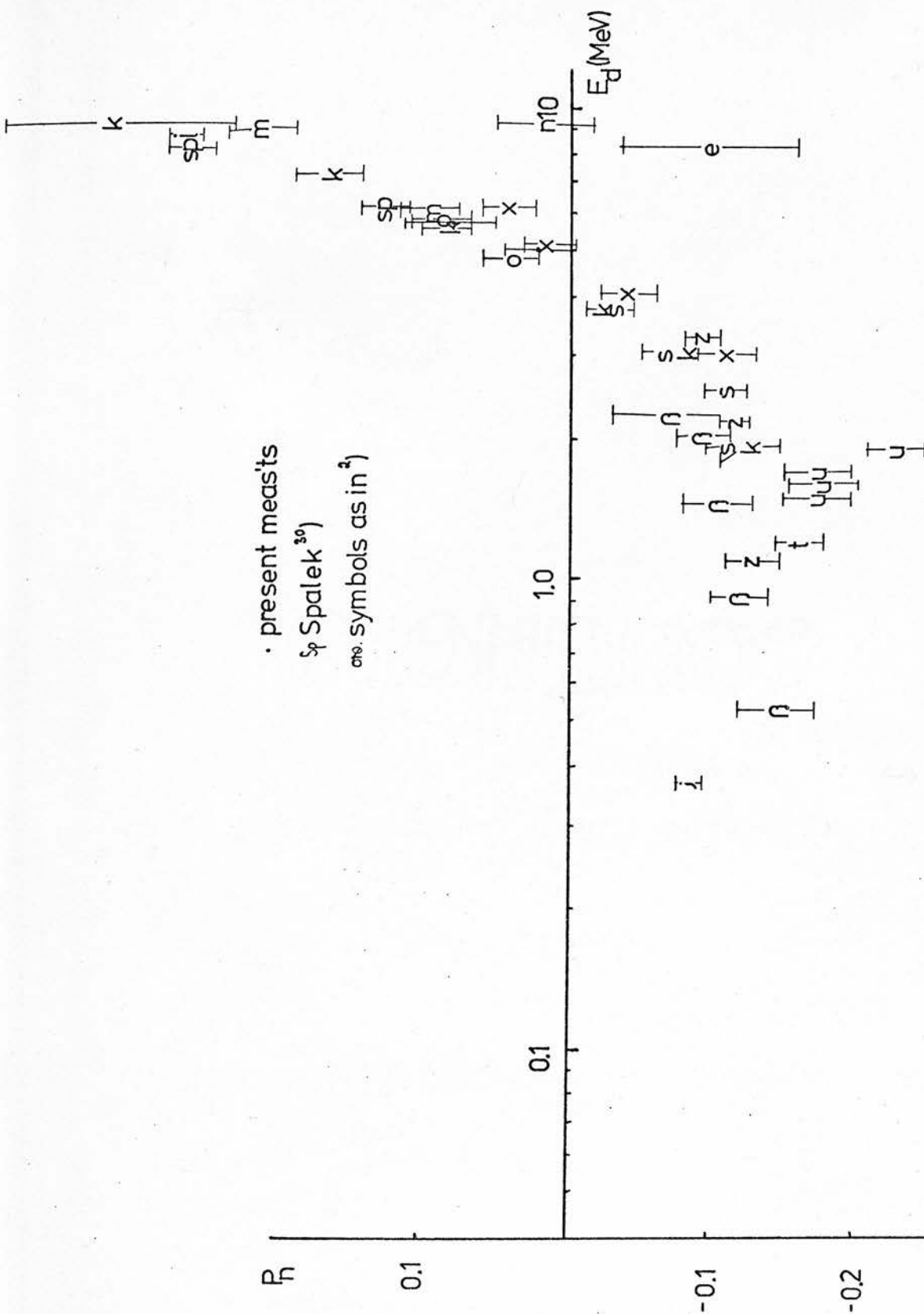
Fig. 21b Polarization of neutrons from the ^{2}H(d,n)^{3}He reaction as a function of incident deuteron energy for laboratory angles of about 33° (symbols as in 2)) + recent measurements.

Table 1 - High Energy Data.

E_d (MeV)	Target thickness (MeV)	Lab. angle	Measured asymmetry	Fractional var'n of $\sigma(\theta)$ (D-d)	Analg. Power	Polarization
2.88	0.24	45°	-0.133	-0.0009	0.882	-0.150 ± 0.016
3.88	0.24	45°	-0.032	0.0020	0.873	-0.039 ± 0.009
4.93	0.14	45°	-0.023	0.0059	0.866	-0.033 ± 0.011
5.45	0.10	45°	-0.018	0.0067	0.863	-0.029 ± 0.02
4.93	0.14	33°	+0.003	-0.0138	0.861	$+0.020 \pm 0.026$
5.45	0.10	33°	+0.057	-0.0138	0.858	$+0.083 \pm 0.033$

^{3}H$(\vec{p},d)^2$H Data [76]

E_d + 1.53	Lab. angle	Polarization
3.53	47°	-0.058 ± 0.021
4.53	50°	-0.033 ± 0.015
5.53	46°	$+0.010 \pm 0.017$
7.53	45°	$+0.107 \pm 0.012$

reported data indicates that the polarization is still negative at 5.5 MeV.

A possible explanation for this discrepancy would involve the degree of correction applied to the recoil spectra. An alternative consideration is the effect of multiple scattering in a large geometry configuration using liquid helium as opposed to the small volume gas scintillators used by the Duke and Edinburgh groups. Stinson [31] has indicated the marked reduction in effective analysing power associated with double scattering in such systems and an underestimate of these effects would obviously give lower polarization values (Section 2.3.1).

The corrections applied to the spectra and resulting asymmetries were outlined in Chapter 5. Recoil spectra taken in coincidence with the left and right side detectors are illustrated in fig. 22 with the subtracted random background superimposed. Free hand extrapolations of extreme tail curves are sketched in as examples of the means by which the true helium scattering events were selected. The random background contained no asymmetry other than that associated with the reaction differential cross-section and thus served as an indication of the form of the appropriate tail correction. The scale and extent of the tail corrections chosen is justified to some degree by the detailed analysis of the recoil spectrum which clearly associates those events in the tail with multiple scattering events in the helium gas and materials of the cell. The Harwell measurements were conducted
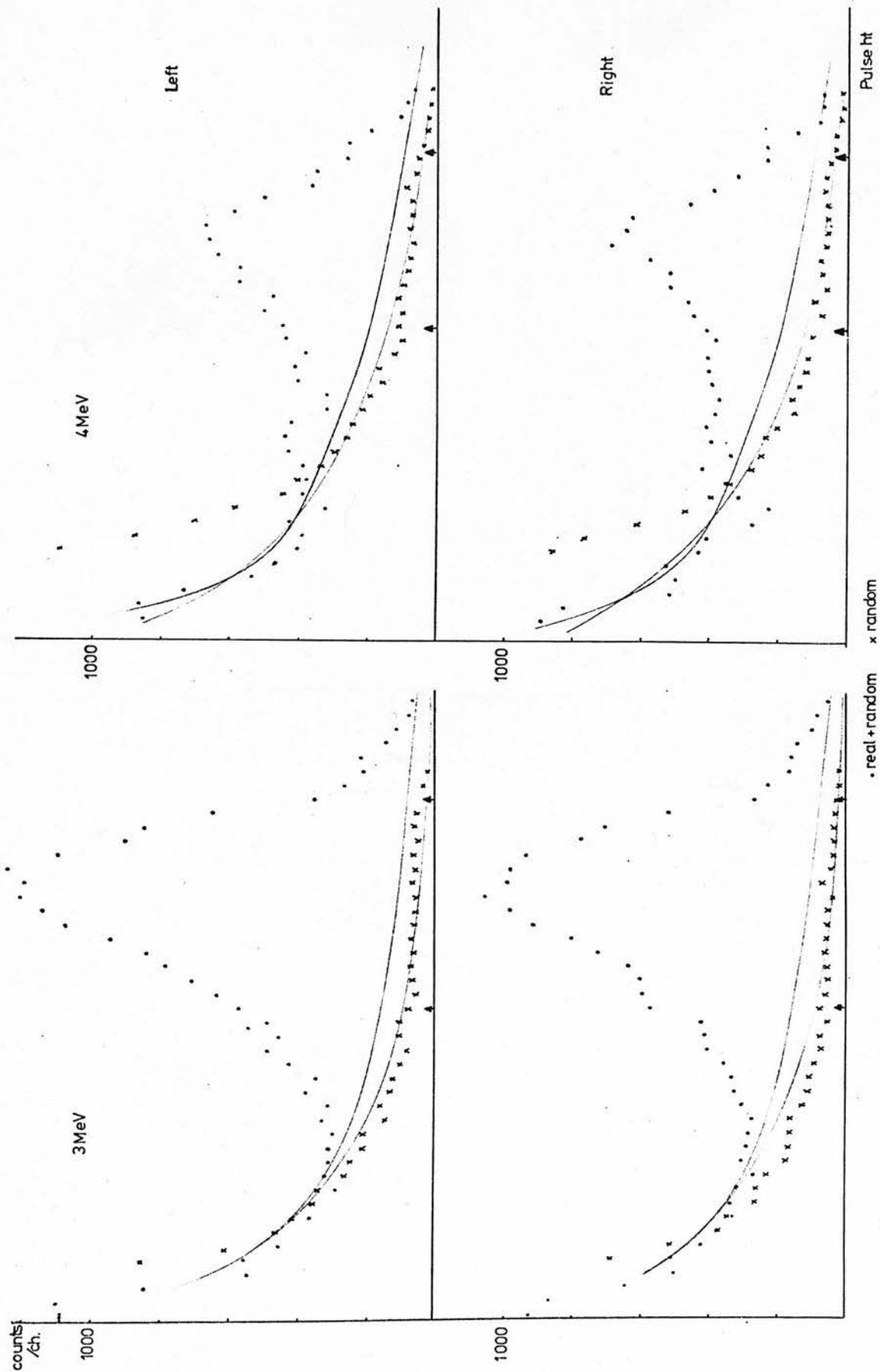
Fig. 22a Recoil spectra obtained for neutron asymmetry determinations at deuteron energies of
3 to 4 MeV at 45° LAB.
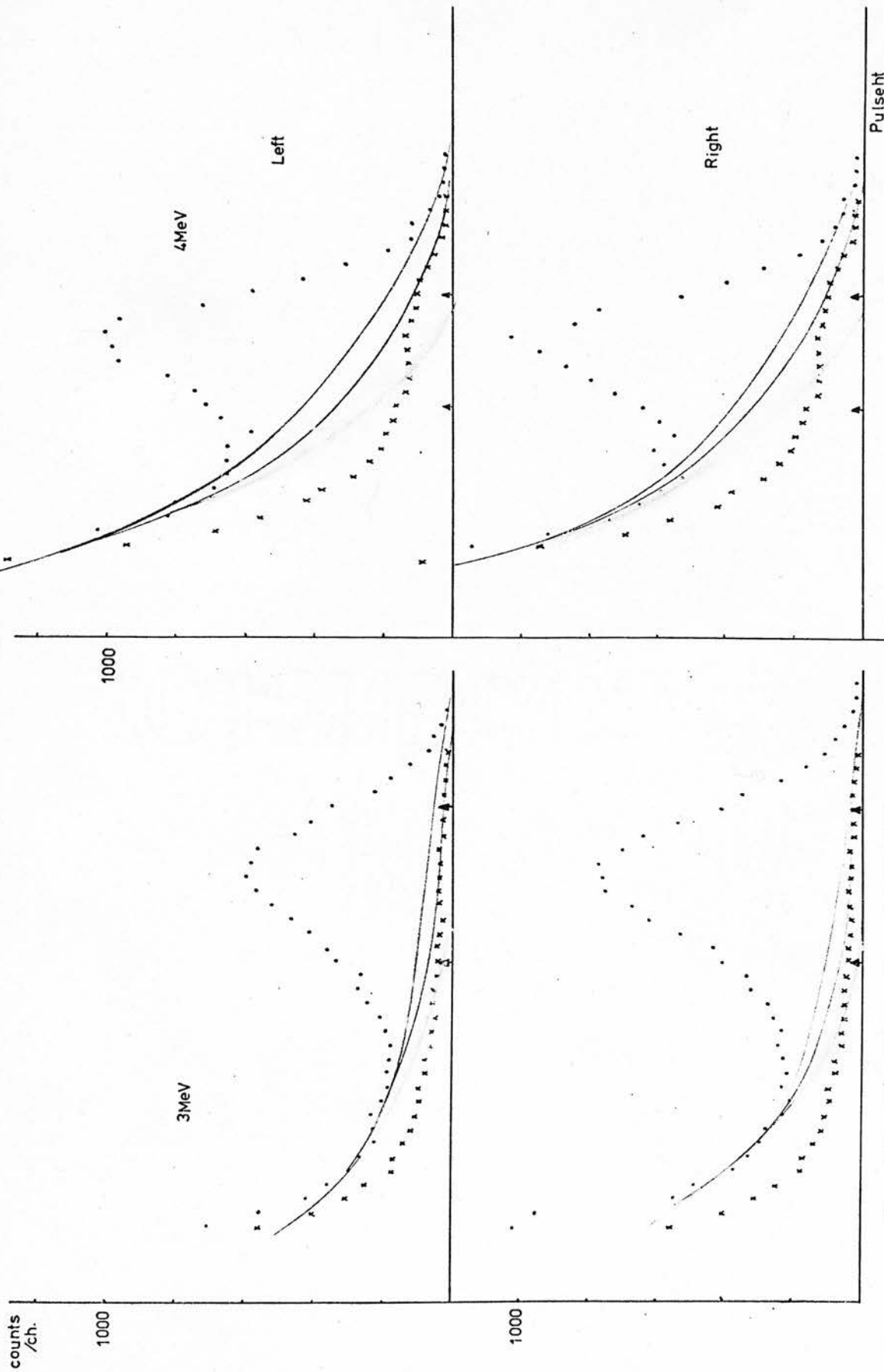
Fig. 22b Recoil spectra obtained for neutron asymmetry determinations at deuteron energies of 3 to 4 MeV at 45°_{LAB} - repeat measurement.
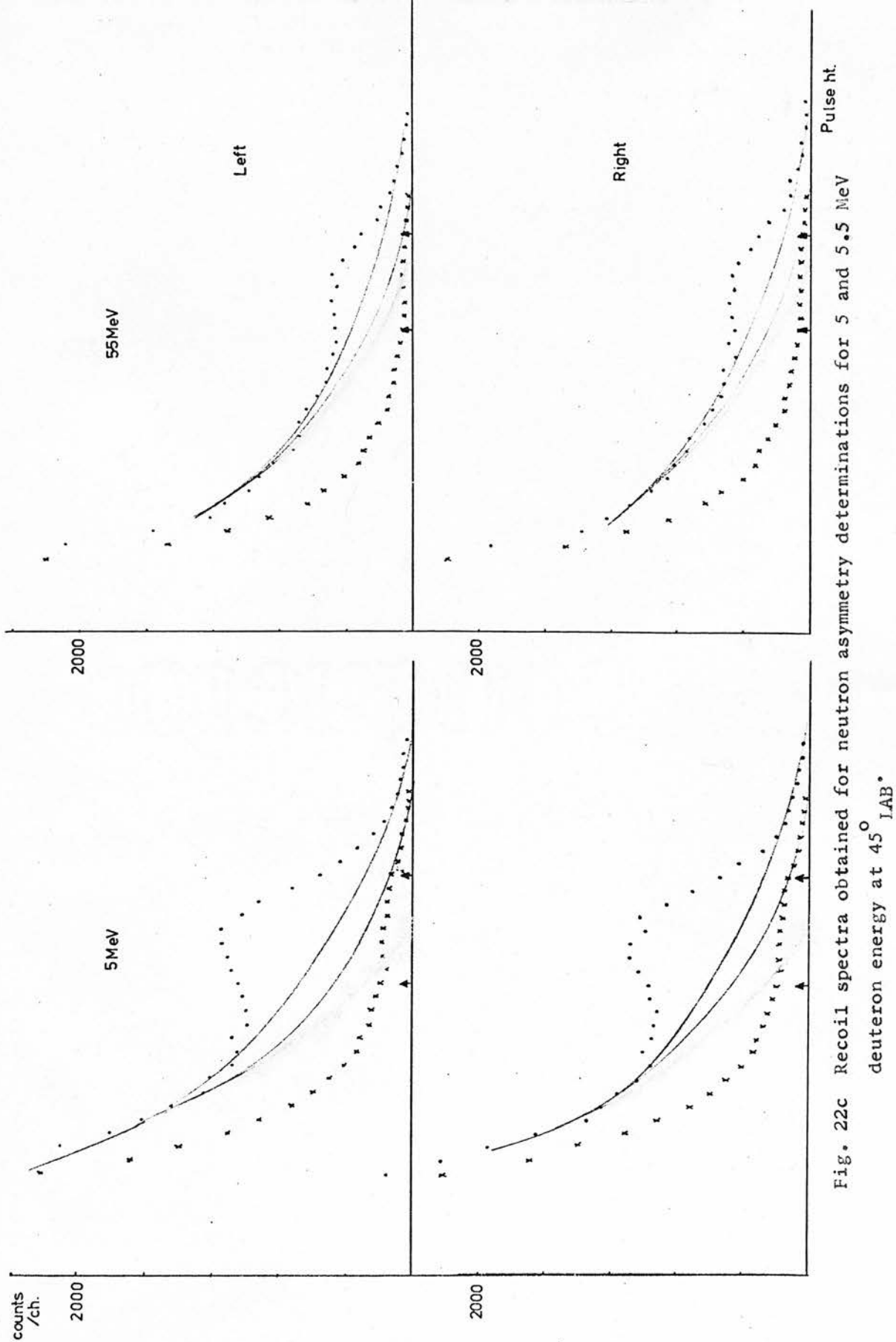
Fig. 22c Recoil spectra obtained for neutron asymmetry determinations for 5 and 5.5 MeV deuteron energy at 45° LAB.
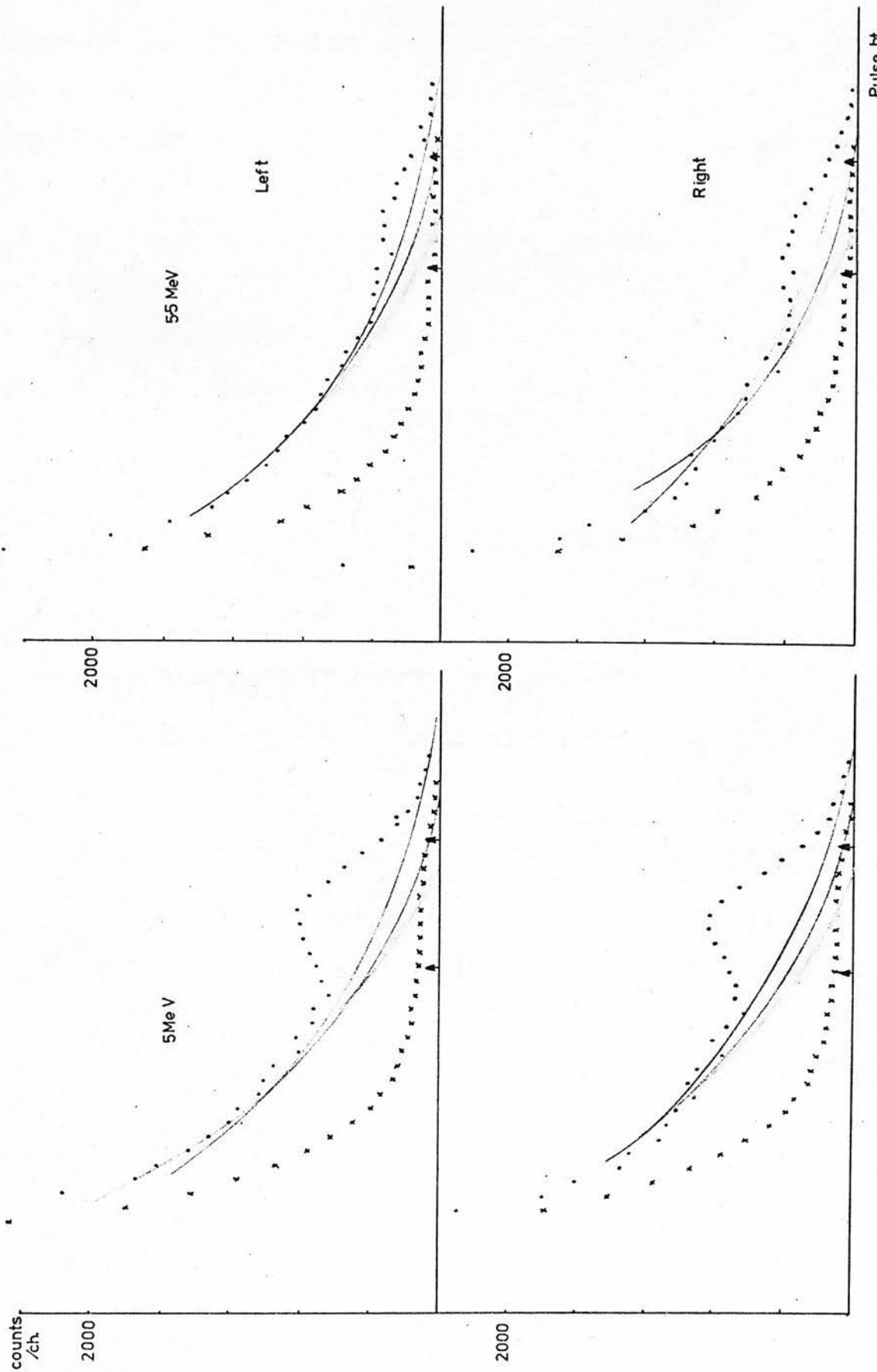
Fig. 22d Recoil spectra obtained for neutron asymmetry determinations for 5 and 5.5 MeV deuteron energy at 33°_{LAB}.

using the earlier version of the helium scintillator and multiple scattering was more prevalent than in later experiments using the redesigned helium cell.

The tail extrapolations could be performed with confidence at lower energies, but as the background contributions increased with energy a larger uncertainty existed in making these corrections. Of assistance in drawing a sensible extrapolation was the known linear relationship between the response of the helium scintillator detector and the energy of incident neutrons.

Other checks and corrections were performed in the process of running but these did not lead to any serious modification to the calculated asymmetries. At incident deuteron energies of 4 MeV or more a plain copper target was found to give rise to counts over the whole spectral range indicated. Dummy runs were performed with such a target and normalised for subtraction from the 'real' spectra using the integrated charge as measured with the Faraday Cup charge integrator. The ^{65}Cu(d,n) [32] and C(d,n) [33,34] reactions were identified as the chief source of such neutrons, there being no evidence of the creation of a 'drive-in' target during the exposure of fresh targets at each energy.

Further runs were performed to determine the contribution to the spectra of neutrons scattered indirectly through the shielding. To do this the collimator was blocked with well-fitting solid inserts, 6 of polythene, 3 of brass, and the resulting spectra

showed this contribution to be quite insignificant.

A check against false asymmetries was performed at several energies by looking for asymmetries at right angles to the reaction plane. Such measurements are easily interpolated with runs in the reaction plane, and the technique is well established as a means of detecting asymmetries created by cabling and detector faults. A more realistic check on such false asymmetries could be performed by attempting to obtain a null measurement at 90° CM reaction angle since for this the detector orientations would more closely resemble that during the reported measurements. Such observations confirmed the absence of any such instrumental effects and a long history of such checks have failed to indicate any systematic or significant deviations from zero in these false asymmetry measurements.

6.2.1 <u>Angular dependence of polarization.</u>

The variation of neutron polarization with reaction angle has been measured at closely spaced energy intervals above 800 keV incident deuteron energy (fig. 2). Below this energy, the only thin target set of observations was performed by Boersma twelve years ago [35]. In an effort to fill this gap in measurements and increase our knowledge of the D-d reaction at lower energies, the neutron polarization was determined at several reaction angles for incident deuteron energies of 340 keV and 500 keV. Thin targets were used so that these observations corresponded

-33-

to discrete energy ranges: the mean deuteron energies were
calculated as 290 keV and 460 keV.

Figure 23 shows the helium recoil spectra taken in coincidence
with one position of the side detectors, and table 2 lists the
reaction parameters and derived observations. Tail extrapolations
are sketched in and corrections made as described earlier. In
addition the asymmetries are entered as calculated for corresponding
strips of "left" and "right" recoil spectra. The tabulated
asymmetries are calculated on the parts of the spectra between
pointers where the values are acceptably consistent, indicating
that inaccuracies in the subtracted tail are negligible and the
large statistical errors at the high energy end of the spectrum
are excluded.

Mention has previously been made of the checks and tests
required to confirm the reliability of the data collection. Rather
than checking against false asymmetries by placing the side
detectors normal to the reaction plane, measurements were performed
in the reaction plane with the polarimeter rotated to $82\frac{1}{2}^{o}$ LAB
reaction angle. The position corresponds to centre of mass angles
of 89° and 91° at 290 keV and 460 keV deuteron energy respectively.
The small negative and positive asymmetries obtained at $82\frac{1}{2}^{o}$ LAB
accord with expectations and imply that any false asymmetries
are less than $|-0.01|$. This magnitude derives from the
assumption that the asymmetries are in reality equally disposed
about zero for these two centre-of-mass angles. Earlier tests
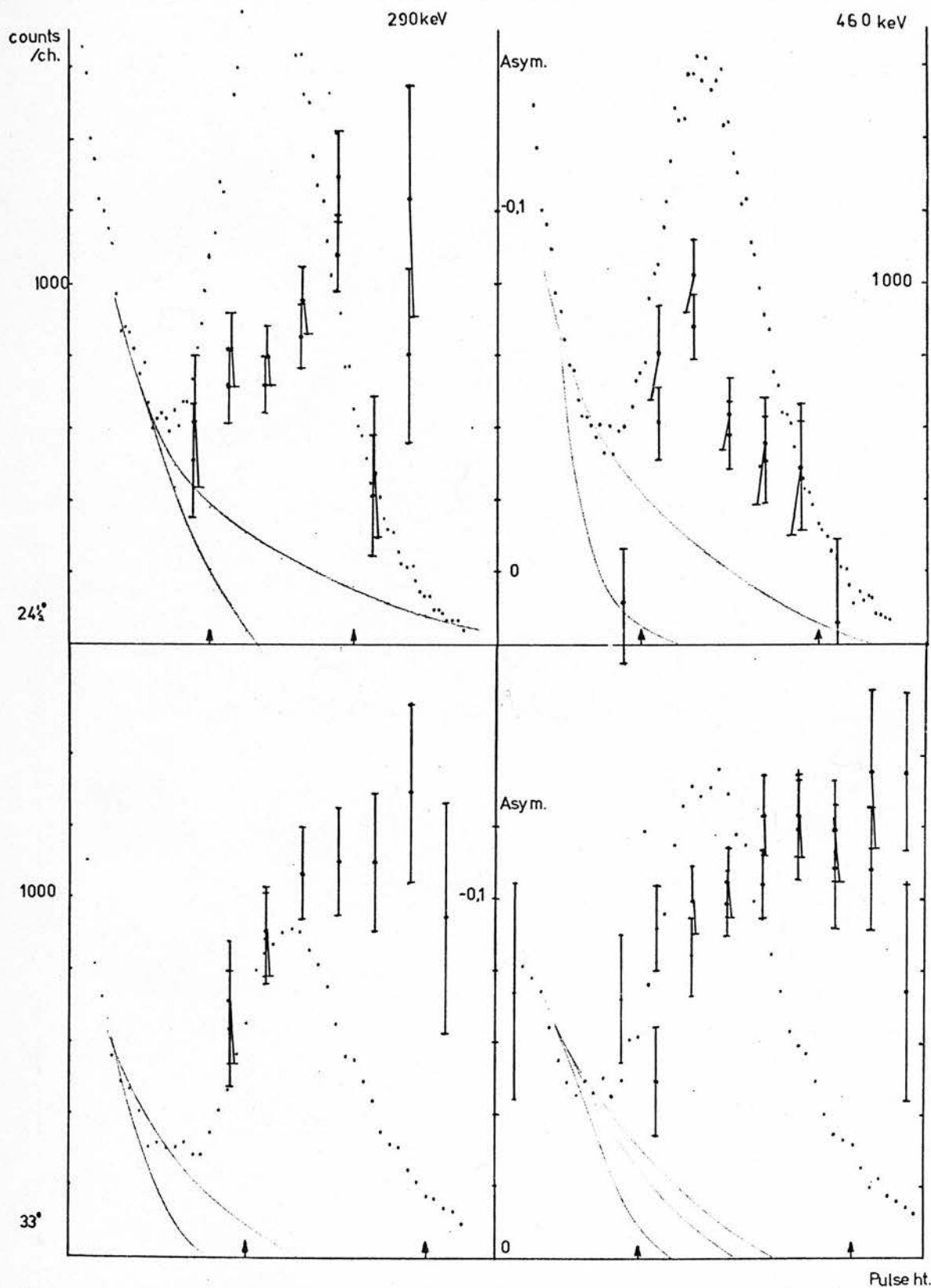
Fig. 23a   Recoil spectra obtained for neutron asymmetry determinations
at mean deuteron energies of 290 and 460 keV for laboratory
angles of $24\frac{1}{2}^{\circ}$ and 33°.
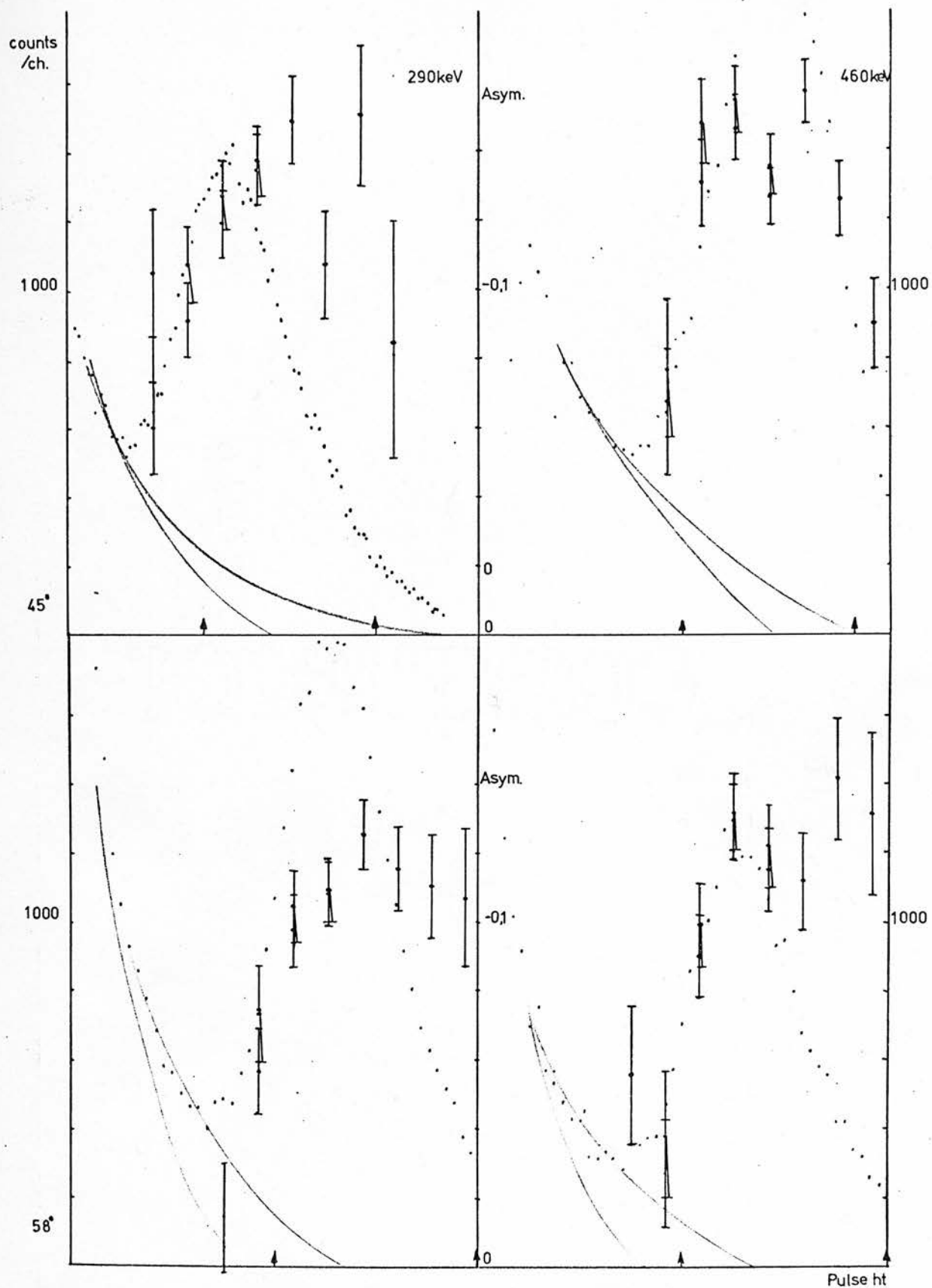
Fig. 23b Recoil spectra obtained for neutron asymmetry determinations
at mean deuteron energies of 290 and 460 keV for laboratory
angles of 45° and 58°.
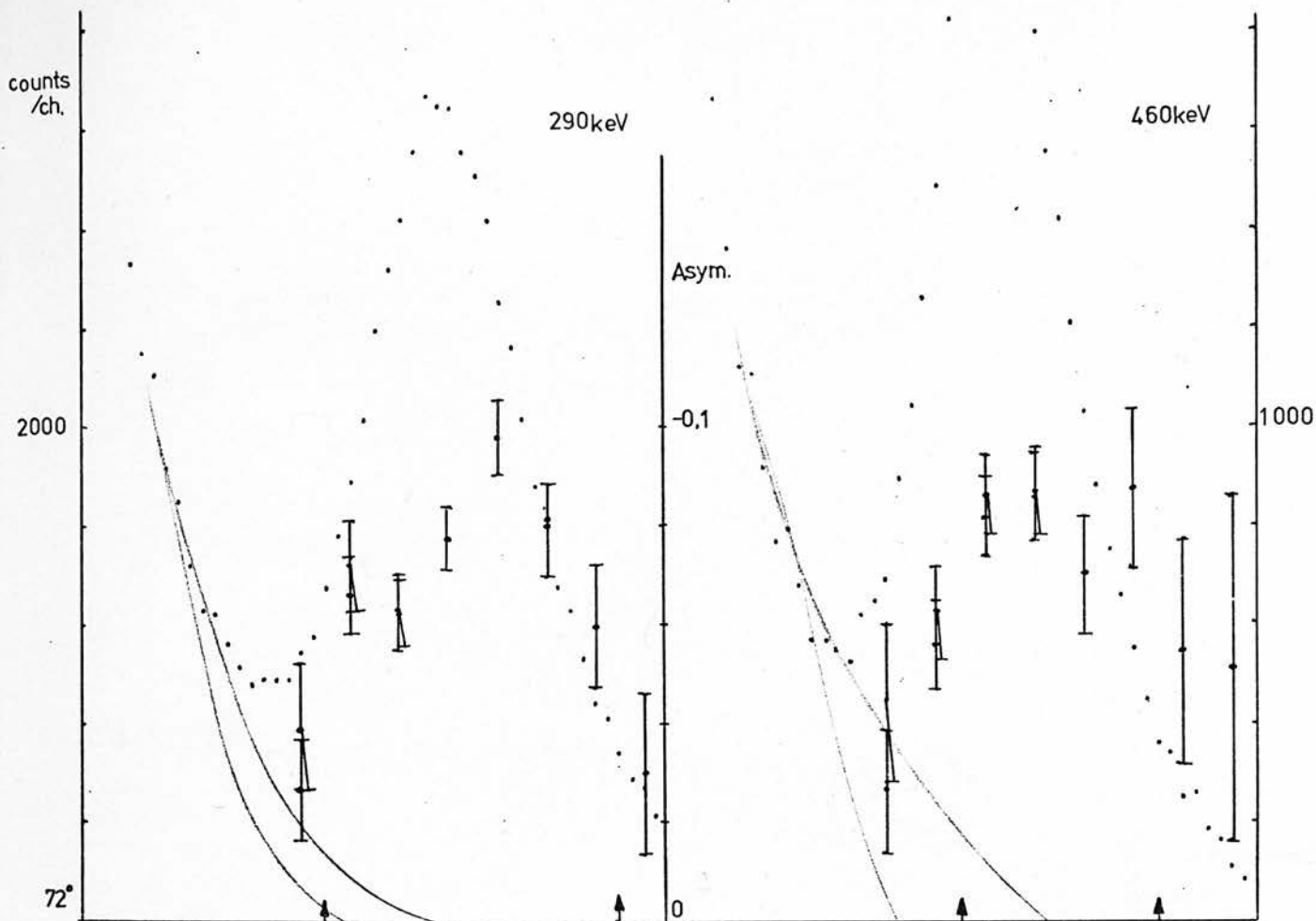
Fig. 23c   Recoil spectra obtained for neutron asymmetry determinations at mean
deuteron energies of 290 and 460 keV for a laboratory angle of 72°.
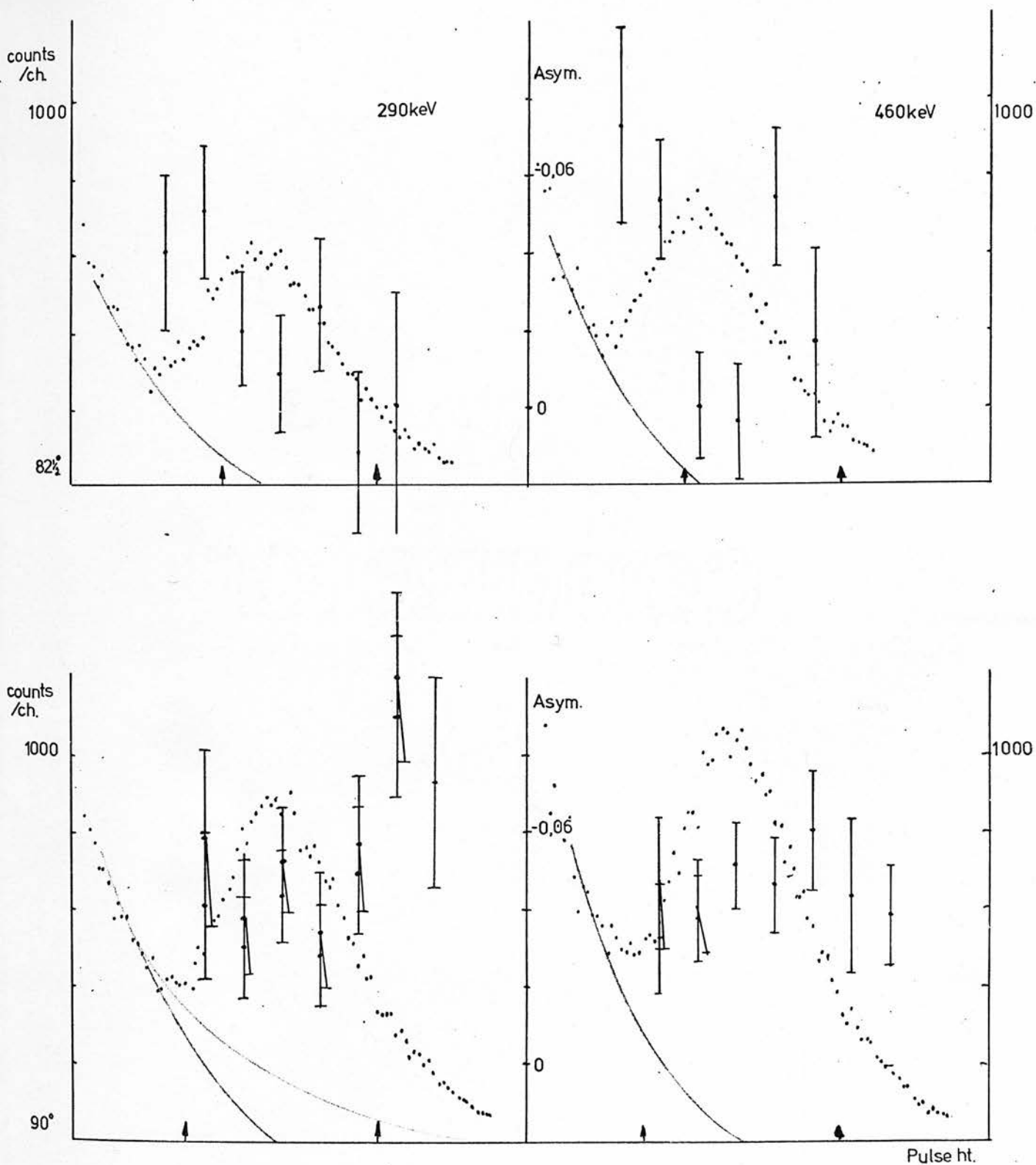
Fig. 23d   Recoil spectra obtained for neutron asymmetry determinations at
mean deuteron energies of 290 and 460 keV for laboratory angles
of $82\frac{1}{2}^{\circ}$ and 90°.

Table 2 — Angular dependence of polarization

$\overline{E}_d$ = 290 keV, target thickness = 105 keV

Lab. angle	CM angle	Measured asymmetry	Analysing Power (46)	Analysing Power (16)	Fractional var'n of $\sigma(\theta)(D-d)^1$	Polarization
90°	97°	+0.042	0.828	0.822	0.0004	0.042∓0.011
82½°	89°	-0.013	0.836	0.832	-0.0007	-0.015∓0.008
72°	78½°	- 0.076	0.848	0.842	-0.0011	-0.088∓0.004
58°	64°	-0.112	0.859	0.854	-0.0022	-0.128∓0.006
45°	50°	-0.123	0.866	0.859	-0.0024	-0.139∓0.008
33°	37°	-0.105	0.871	0.865	-0.0019	-0.118∓0.007
24½°	27°	-0.066	0.874	0.869	-0.0016	-0.074-0.010

$\overline{E}_d$ = 460 keV, target thickness = 95 keV

Lab. angle	CM angle	Measured asymmetry	Analysing Power (46)	Analysing Power (16)	Fractional var'n of $\sigma(\theta)(D-d)^1$	Polarization
90°	99°	+0.047	0.832	0.828	0.0005	0.056∓0.007
82½°	91°	+0.002	0.844	0.839	-0.0006	0.003∓0.010
72°	80°	-0.082	0.855	0.852	-0.0014	-0.094∓0.006
58°	65°	-0.116	0.867	0.863	-0.0027	-0.131∓0.007
45°	51°	-0.135	0.874	0.870	-0.0026	-0.151∓0.012
33°	38°	-0.106	0.880	0.876	-0.0030	-0.117∓0.006
24½°	28°	-0.050	0.882	0.879	-0.0016	-0.055-0.010

using a gamma source carefully secured within the rotating polarimeter also indicated an absence of asymmetry greater than 0.8% for all four side detectors.

Uncertainties in asymmetry are inseparable from errors in the measurement of reaction angle. The angle between the polarimeter and beam line axes may be determined to less than $\frac{1}{2}^o$ but the assumption that the beam axis is parallel to the beam line is often ill-founded. In a sequence of runs with similar beam steering a systematic error will probably occur. A realistic limit of $1\frac{1}{2}^o$ may be placed on this source of error (see fig. A3). Again the measurements at $82\frac{1}{2}^o$ LAB may be taken to indicate the precision with which the reaction angle is determined; an overestimate of about 1° in the angle measurement would explain the displacement of the plotted points from any fitting curve obliged to pivot about 90° CM.

Modification of the shielding was performed for each angle change (fig. 5) and proved to be sufficient to reduce to negligible proportions the neutrons scattered indirectly into the polarimeter. Greater care in shielding was necessary for those positions of the polarimeter approaching 90° to the beam line where the polarimeter was more exposed to direct radiations from the analysing magnet and beam line.

The trend of the data is closely similar at these two energies. In particular best fit curves indicate a maximum

polarization at $52.5° \pm 1°$ with peak values of -0.142 ± 0.012
and -0.153 ± 0.012 at 290 keV and 460 keV respectively. This
trend agrees with that previously and currently reported by this
group (fig. 24). The measurements were extended beyond 90° CM to
indicate the antisymmetric behaviour of the polarization about
this angle.

The differential polarization $P(\theta) \, \sigma_c(\theta)$ which can be
expanded as $\sum_n a_n \sin 2n\theta$ in centre-of-mass coordinates [36]
provides a convenient parameterization for comparing measurements
with one another as well as with models of the reaction. The
normal equations for the unknown coefficients in the expansion
were solved with the unequally weighted observations input as
parameters (Appendix B). These coefficients are listed in table 3.

Several conclusions may be drawn from these results.
Remembering the similarity of the angular distributions at these
two energies the difference in these coefficient sets must be
predominantly associated with the corresponding change in the CM
differential cross-sections. The a_2 and a_3 coefficients at both
energies are compatible with zero. Best fit curves derived by
plotting $\frac{1}{\sigma_c(\theta)} \sum_n a_n \sin 2n\theta$ at the two energies are shown in fig. 25,
the coefficient errors being used to derive the range of fit
associated with each solution set. The three term fit achieves
better 'coverage' of the data at both energies, though the fit
at $24\frac{1}{2}°$ LAB is still unsatisfactory. However the introduction
of a_3 has a negligible effect on the value of the first coefficient.
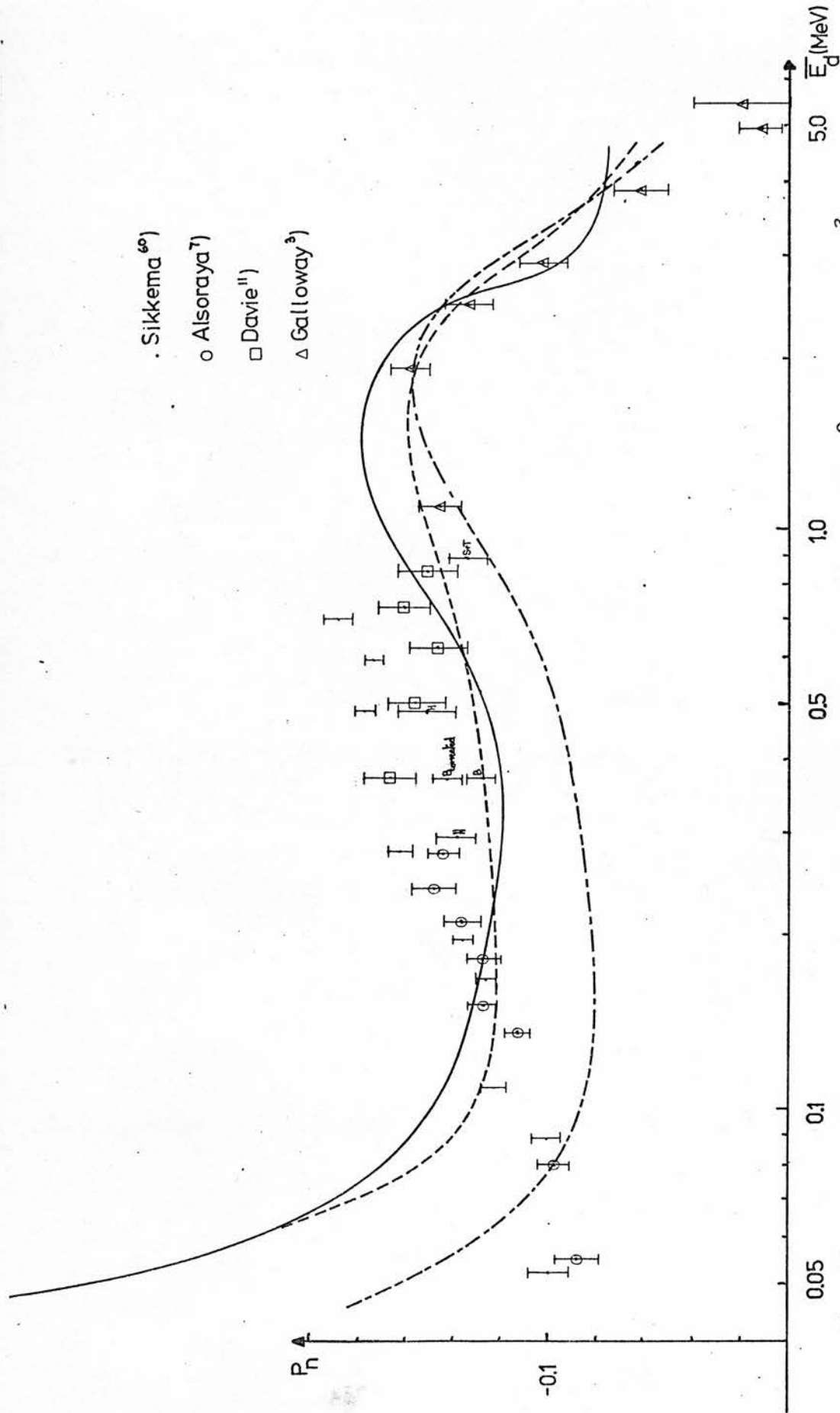
Fig. 24 Polarization of neutrons emitted at a laboratory angle of about 45° from the D(d,n)³He reaction as a function of deuteron energy.

Table 3 — Best fit coefficient values for the differential polarization expansion $\sum_n a_n \sin 2n\theta$.

$\overline{E}_d$ = 290 keV, target thickness = 105 keV

	a_1	a_2	a_3
three coeff. fit	-0.588 ± 0.021	-0.029 ± 0.027	-0.016 ± 0.019
two coeff. fit	-0.582 ± 0.020	-0.011 ± 0.016	

$\overline{E}_d$ = 460 keV, target thickness = 95 keV

	a_1	a_2	a_3
three coeff. fit	-0.798 ± 0.030	$+0.005 \pm 0.042$	-0.015 ± 0.033
two coeff. fit	-0.801 ± 0.029	$+0.011 \pm 0.023$	
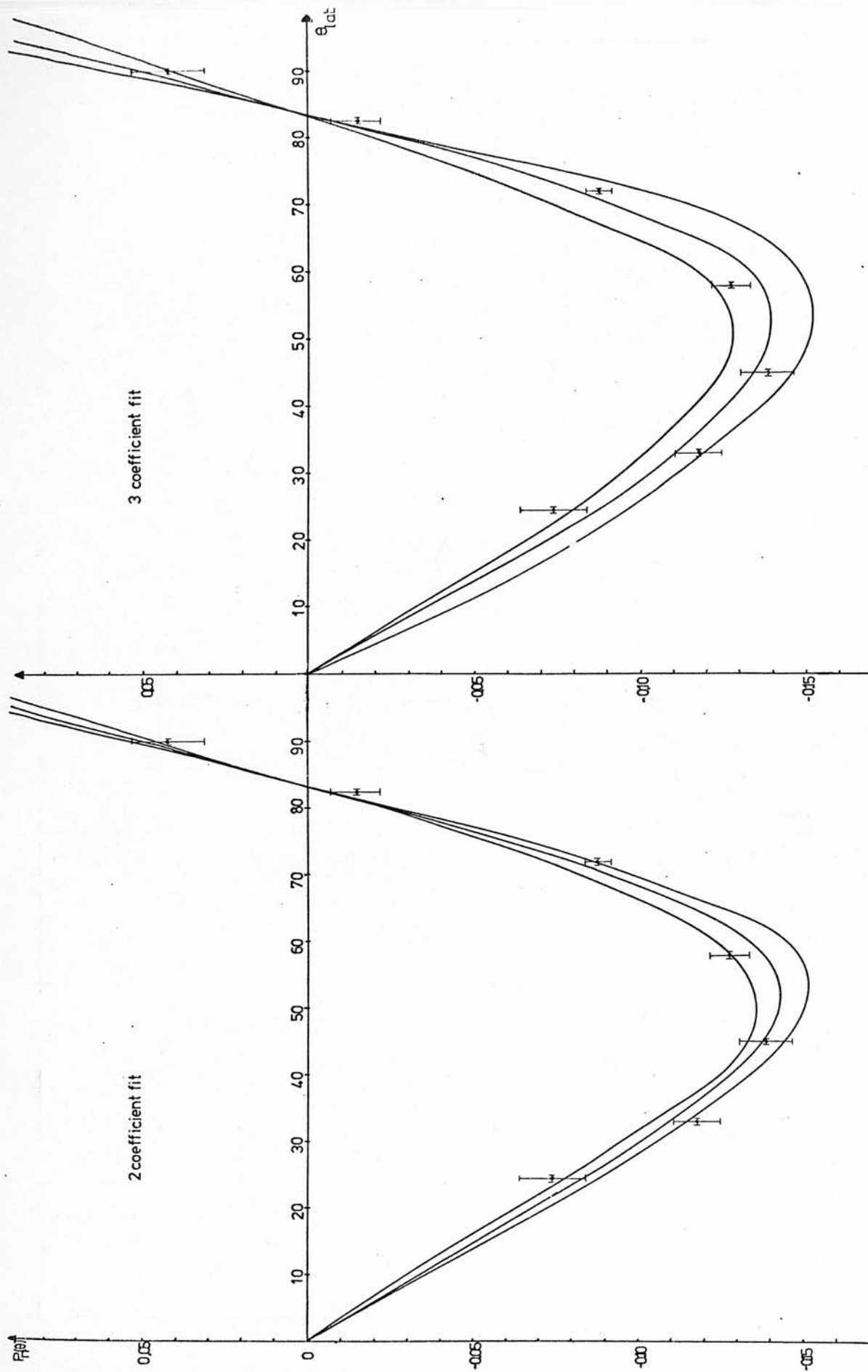
Fig. 25a Angular variation of neutron polarization in the $D(d,n)^3He$ reaction for a mean deuteron energy of 290 keV with two and three coefficient fitting curves.
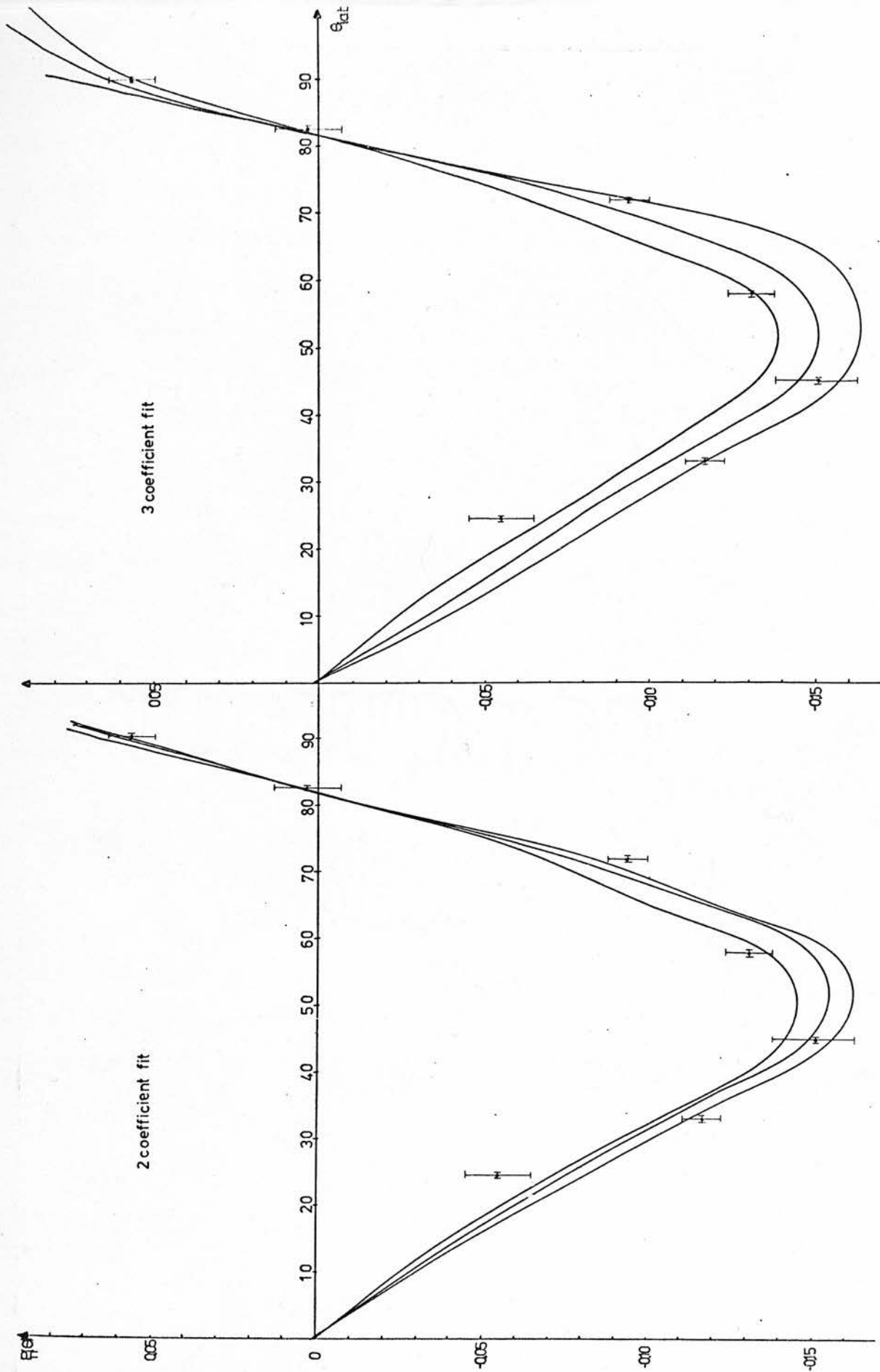
Fig. 25b Angular variation of neutron polarization in the D(d,n)³He reaction for a mean deuteron energy of 460 keV with two and three coefficient fitting curves.

The expansion coefficients may be compared with others over a wide energy range (fig. 26) [3]. However, the only neighbouring thin target measurements are those of Boersma at 350 keV [35]. The presently reported values for two coefficient fits appear compatible with Boersma's measurements but imply the need to increase the magnitude of the a_1 fitting curves described in a recent paper [3]. This conclusion is supported by the trend of the polarization values at 45° LAB around 0.4 MeV as shown in fig. 24 compared with the values predicted by the fitting curves. In this context it is worth noting that Boersma's 46° LAB measurement as originally reported falls significantly below the expected trend; but applying the corrections for instrumental asymmetries mentioned by Walter [37] gives a more satisfactory value. Such corrections applied to Boersma's entire angular distribution polarization measurements would raise the magnitude of a_1 at 350 keV by 10% - 15% lending further support to the suggested behaviour of a_1 in this energy region.

A more precise determination of the behaviour of a_1 and a_2 would serve as a useful parameterization for neutron polarization as well as casting light on models of the reaction. It is appropriate at this stage to consider the theoretical basis for these coefficients.
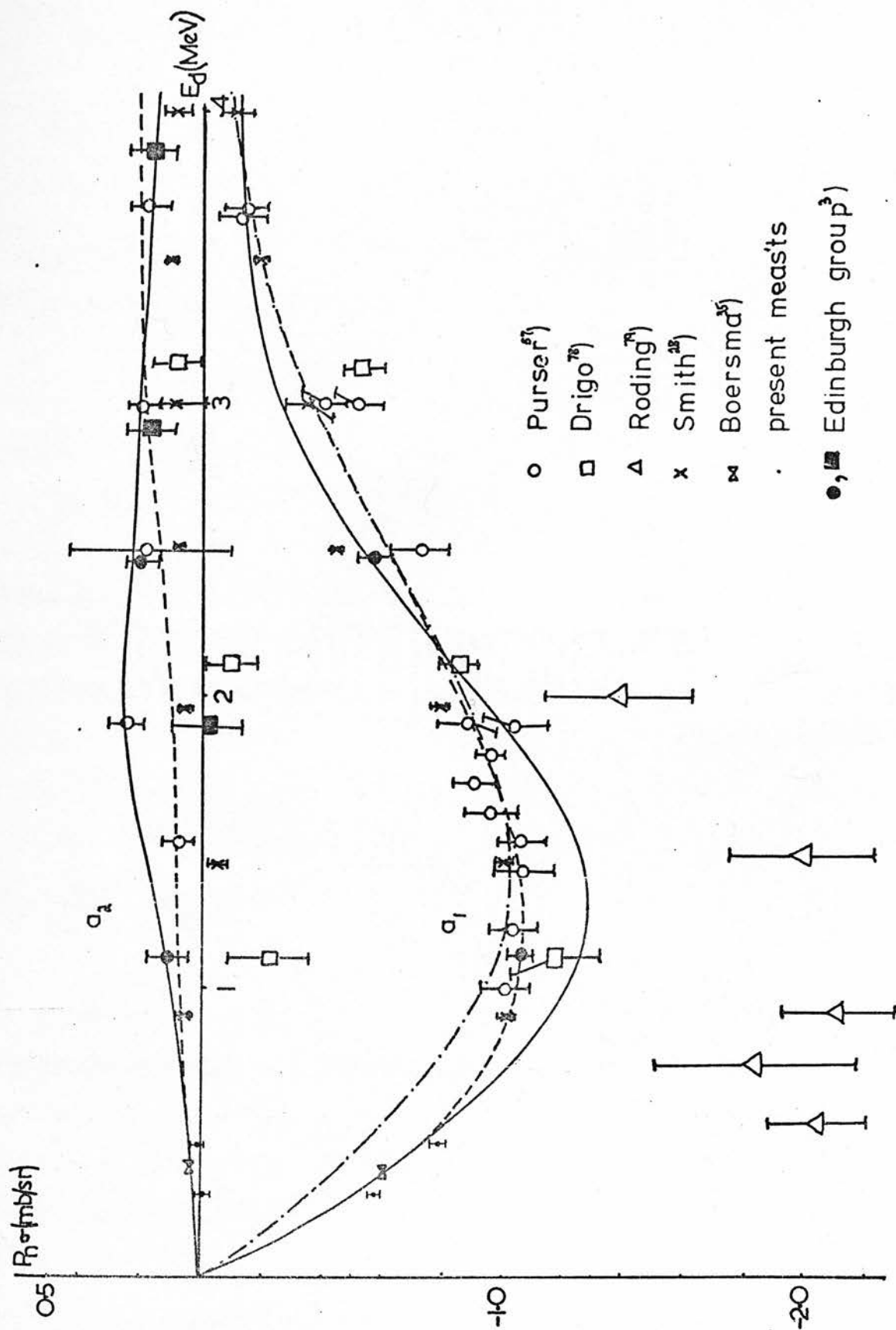
Fig. 26 The differential polarization coefficients a_1 and a_2 for deuteron energies up to 4·MeV showing present measurements.

6.2.2 Theoretical background to the differential polarization expansion coefficients.

The differential polarization is conventionally expanded as:

$$\pi(\theta) = P_n(\theta)\sigma(\theta) = B_2 P_2'(\cos\theta) + B_4 P_4'(\cos\theta) + \ldots$$
$$= \sum_{n \text{ even}} B_n P_n'(\cos\theta) \tag{1}$$

and the differential cross section as:

$$\sigma(\theta) = A_0 + A_2 P_2(\cos\theta) + A_4 P_4(\cos\theta) + \ldots \tag{2}$$

Boersma [38] gives expressions for the coefficients A and B in terms of the transition matrix elements. In the low energy treatments of Konopinski and Teller [39] and of Boersma [38] the coefficients A_2 and B_2 only differ by an energy-independent factor. An alternative expansion form for the differential polarization has been used by numerous workers as referred to earlier:

$$\pi(\theta) = P_n(\theta)\sigma(\theta) = a_1 \sin 2\theta + a_2 \sin 4\theta + \ldots \tag{3}$$

Thus as a result of the equivalence of these expansions in the low energy approximation we have:

$$B_2 = CA_2 = \frac{2}{3} a_1 \text{ or } a_1 = \frac{3CA_2}{2} \tag{4}$$

These coefficients may be written in terms of the modes of interactions involved. They are made up of rather complicated combinations of elements of the scattering matrix and angular momentum coefficients. The properties of the polarization and selection rules have been discussed by various authors and summarised by Simon and Welton [40]. Their complexity rule

established the connection between n_{max} and the highest value of angular momentum contributing to the reaction. Their selection rules additionally indicate that polarization requires the introduction of spin-orbit coupling and the involvement of incident or final state waves with $l > 0$. In the notation of Purser [27]:

$$q_l(E) = a \sigma_1 + \alpha (\sigma_0 \sigma_2)^{1/2} + \beta \sigma_2 + b (\sigma_1 \sigma_3)^{1/2} + c \sigma_3 \tag{5}$$

where σ_l are the approach cross-sections introduced by Konopinski and Teller [39] to describe the energy dependence of the penetration probability for a pair of deuterons possessing a certain relative orbital angular momentum, and the coefficients of the σ_l are the energy independent intrinsic probabilities and indicate the relative importance of the contributions. It is assumed that the resulting polarization is to no extent dictated by transitions in the exit channel and this seems plausible for low deuteron energy as a consequence of the high Q-value for the $D(d,n)^3He$ reaction (+ 3.269 MeV) and the absence of any confirmed resonances. The form of equation (5) introduces sufficient degrees of freedom that fits to experimental measurements may be obtained by skilful selection of the coefficients rather than as a result of correct model predictions of approach cross-sections.

One way to check our understanding of the underlying mechanism is by comparing observations with the mirror reactions $D(d,p)^3H$ and $D(d,n)^3He$. The difference in angular distributions and polarizations between these reactions was thought to

indicate a charge symmetry violation until Hardekopf et al [41] showed that the characteristics of the reactions were very comparable if analysed at the same exit channel energy. A dependence on the exit channel may be involved in equation (5)(p.39) by supposing that the coefficients are also energy dependent; that these intrinsic reaction probabilities must be related to the relevant total cross sections was first pointed out by Boersma [42].

Speculation [41] as to the implications of this exit channel energy dependence leads to a resurgence of interest in the role of $l = 0$ stripping in these reactions. This interpretation of the reaction mechanics has been successful down to $E_d = 5$ MeV [43-45] and it would be in line with direct reaction theory to associate polarization effects with spin - dependent distortions in the entrance and exit channels. Taking surmise a step further it might be suggested that the extent to which a direct - reaction process is involved should be a function of incident deuteron energy and angle of emission.

A more powerful experimental technique is required to critically examine such conjecture. The use of polarized deuteron beams allows the individual elements in the transition matrix to be determined and thereby separates out the contribution of different angular momentum states. Simmons et al [46] investigating the $D(d,n)^3He$ reaction at $0°$ with a polarized

deuteron beam (at energies in the range 4 - 15 MeV) concluded
that "to a great extent the outgoing neutron retains the
polarization it had in the incident deuteron". Subsequent
observations [50 - 52] have confirmed this interpretation, the
deficit in polarization being associated with the D-state of the
deuteron and additionally for the (d,n) reaction with some
reaction spin-dependent effect. Blyth et al [53] have proposed an
alternative crude but effective explanation for this behaviour
based on geometrical and spin selection considerations. Greubler
et al [47] compared the reactions as suggested by Hardekopf and
obtained improved agreement in tensor analysing powers (T_2) for
the two reactions but discrepancies in the vector analysing
power (T_1) were increased. Hilscher [48] also found discrepancies
in T_1 at backward angles but obtained a quantitative explanation
using DWBA calculations with potentials differing in electro -
magnetic terms only. On the other hand Salzman [49] found no need
for such treatment of his measurements on the (d,n) reaction at
forward angles. It may be observed that the differences in
analysing powers and experimental errors make meaningful
comparisons of the reactions at different energies more difficult
than for unpolarized beams. One may also consider that the issue
is being complicated by the introduction of spin-dependent
effects in the deuteron channel.

In deriving the elements of the transition matrix from
such experiments one can associate dominant terms with
resonances in the compound nucleus interpretation of the reaction.

Such investigations have been performed by Seiler and some
tentative conclusions appear in a recent paper [54]. The suggested
approach is to make an independent analysis of the reaction at
low energies where there are only few contributing matrix
elements. Below 1 MeV many reactions have strongly resonant
states induced primarily by s - wave deuterons. Having determined
the various elements, interference terms and combinations of
such terms one may extrapolate to higher energies using an energy
dependent parameterization such as an R - matrix fit [55].

For the d-d reactions the analysis is tentative partly
because of the conflicting evidence concerning resonances in the
neighbourhood of the d-d threshold and partly due to the absence
of polarized deuteron measurements in the 0.5 to 3 MeV range.
Seiler refers to the possibility of partial overlap of two levels
of opposite parity in the compound nucleus as being consistent
with the data. However this is only one of several explanations
of low energy observations and the present state of knowledge
thus makes an unsatisfactory starting point for extrapolation
to higher energies.

Fick has demonstrated [56] how the BPK approach at low
energies may be incorporated in R - matrix theory with specific
boundary conditions. The model dependence previously pointed out
by Boersma [42] was more forcefully illustrated here by the fact
that the boundary condition of a hard sphere led to physically
meaningless results. It is thus reasonable to apply the BPK

approach in the low energy region both to compare with earlier workers findings in the context of approach cross-sections and to investigate the above mentioned model dependence. However at higher energies and small lab. angles a contribution from direct interactions may be anticipated.

A possible way of formalising this approach was suggested by Thornton et al [63] in the context of the $^9Be(d,n)^{10}B$ reaction. The various contributions are there related as :

$$P_{expt}(\theta) = P_{DI}(\theta)\,\sigma_{DI}(\theta)/\sigma_{expt}(\theta) + P_{CN}(\theta)\,\sigma_{CN}(\theta)/\sigma_{expt}(\theta) + \text{interference term}$$

where the interference term averages to zero when the direct interaction (DI) is dominant and $\langle P_{CN}(\theta)\,\sigma_{CN}(\theta)\rangle$ is zero when the mean compound nucleus (CN) level width is much greater than the mean level spacing.

It is recalled that the coefficients in equation (5) p.39 indicate the contribution made by different forms of interaction. In particular there is interest in the spin-orbit interaction required to explain the presence of polarization, and whether a tensor force alone is involved or that internucleonic forces of the $\underline{\ell}.\underline{s}$ form are present. Purser [57] initiated the procedure of plotting the variation of the expansion coefficients of equation (3) as a function of energy. Fitting expressions for a_1 and a_2 (equation(3) p.38) to the experimental points enables the relative importance of the different terms to be determined. The validity of the approach cross-sections obtained on the basis of different

nuclear models may also be investigated in this way. For example
Fierz [36] has pointed out that α and β in equation (5) must
vanish if only central and tensor forces contribute and using the
BPK values for σ_ℓ [58] the solid and dash-dot curves in fig. 26
(see also ref. 3) were obtained. (The solid curve differs in that
Boersma's measurement at 350 keV [35] was taken into account).
The dashed line provides a better fit to all the data points by
also including the terms associated with a spin-orbit interaction.
Such an analysis ignores the suggested limitation of this approach
to the low energy region and relies on the multiparameter format
of equation (5) to accomplish a fit. Rook and Goldfarb [59] were
able to fit the energy dependence of the measured neutron
polarization below 700 keV using only the first two terms in
equation (5).

From the foregoing resume it appears that the mechanisms
involved in the D-d reaction may be investigated by a variety of
means but the theoretical interpretation must respect the
limitations of the theory and take account of the possible
presence of competing processes.

6.2.3 Analysis and interpretation of available data.

A more precise determination of the behaviour of a_1 and a_2
would serve as a useful parameterization for neutron polarization
in the D-d reaction and lead to a better interpretation of the
interactions involved. In the energy range below 1 MeV further

data for both these purposes has only recently become available. Firstly Alsoraya's measurements [7] provide a detailed and precise account of the neutron polarization below 300 keV (fig. 24). This data is corroborated by Sikkema's thin target measurements [60] which however deviate significantly from the trend exhibited in fig. 24 at higher energies. There is thus no such clearly defined behaviour attributable to the neutron polarization in the 0.5 - 1.0 MeV deuteron energy range. The only other relevant information is the angular distribution at 0.87 MeV reported by Smith and Thornton [28] as one of a sequence of accurate determinations of differential polarization Legendre expansion coefficients. The recalculation of the coefficients and their errors in the $\sum a_n \sin 2n\theta$ expansion was performed by Maayouf [61]. Measurements near $45^o{}_{LAB}$ from the various angular distributions considered are also displayed in fig. 24.

With this new data a more accurate determination of the behaviour of the expansion coefficients at low energy may be obtained. Firstly the fitting curves referred to in the previous section and depicted in fig. 26 may be used to predict the polarization at $45^o{}_{LAB}$ and the energy dependence of this polarization is illustrated in fig. 24. Even the fits which took account of Boersma's original measurements [35] fail to give a satisfactory account of the polarization both in the 0.2 - 0.6 MeV range and also in the low energy region (< 0.12 MeV). Accordingly Alsoraya's measurements [7] were used to derive values for a_1 below 300 kev. Using available thin target measurements at about

45°_{LAB} the behaviour of a_1 was traced in a similar manner up to 840 keV. In this approach it was not possible to take the a_2 term into account and this resulted in an error in a_1 which increased with energy and θ_{cm}. At 275 keV, taking a value of 0.02 for a_2 indicated an overestimate in the magnitude of a_1 of the order of 1%, and at 875 keV, using Smith and Thornton's data [28], of about 3%. However these inaccuracies are small by comparison with the errors associated with the derived values of a_1.

The data used in constructing figs. 24 and 27 appear in Table 4. Sikkema's data [60] was obtained at a range of neutron lab. angles from 46° to 50° and is included to indicate the agreement with Alsoraya's measurements [7] at low energy (at $\theta_{\text{LAB}} = 45^\circ$). As previously mentioned Sikkema's measurements deviate from the trend established earlier by the Edinburgh group [11] which is also tabulated. Table 4b lists the angular distribution measurements used in fig. 27 along with representative values at about 45°_{LAB} used in fig. 24.

A first natural step in attempting a fit to these coefficients is to test the validity of the low energy approximation as expressed in equation (4) of the previous section. The values of A_2 were derived from Liskien's tables [1] and the value of C' adjusted to give precise agreement for the measurements at 180 keV. This procedure indicates the dominance of the first term in the differential polarization expression (equation (3)) up to 300 keV
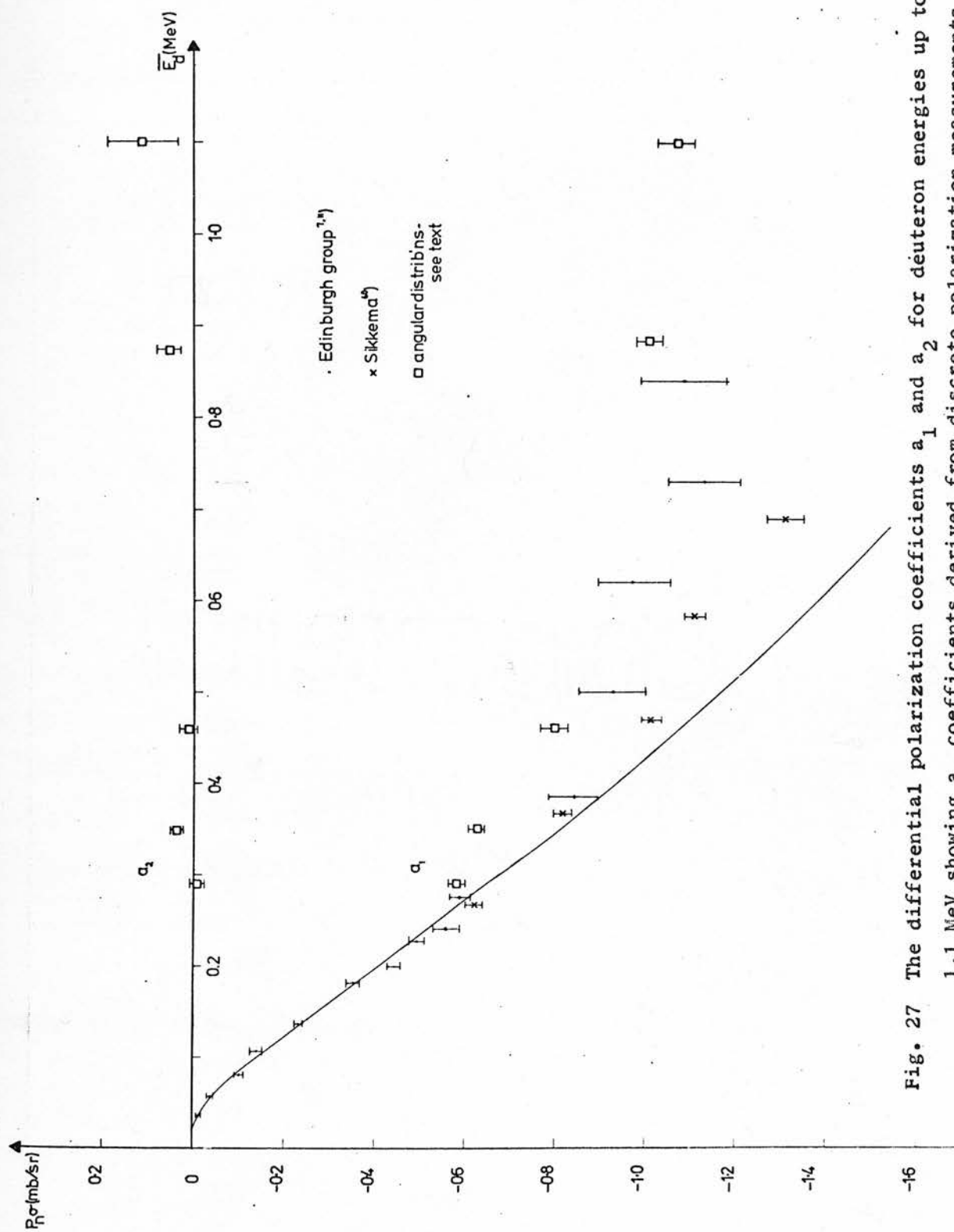
-46-

Fig. 27 The differential polarization coefficients a_1 and a_2 for deuteron energies up to 1.1 MeV showing a_1 coefficients derived from discrete polarization measurements with thin targets at a laboratory angle of about $45°$.

Table 4 — Values used in plot of figures 24 and 27.

a) Discrete polarization measurements up to 1.1 MeV.

E_d (MeV)	P_n	θ_c	σ_c (mb/ster.)	a_1	Sources & conditions
0.035	-0.078 ∓ 0.011	46.4	0.22	$-0.0172 \mp 0.0024.$	
0.055	-0.091 ∓ 0.009	47.1	0.47	$-0.0411 \mp 0.0041.$	
0.080	-0.101 ∓ 0.007	47.6	1.00	$-0.1014 \mp 0.0070.$	
0.105	-0.093 ∓ 0.010	47.9	1.50	$-0.1402 \mp 0.0151.$	Edinburgh group [7]
0.135	-0.117 ∓ 0.005	48.4	2.00	$-0.2357 \mp 0.0101.$	. symbol He gas scint.
0.180	-0.127 ∓ 0.006	48.9	2.78	$-0.3564 \mp 0.0168.$	2 interchangeable
0.198	-0.147 ∓ 0.005	49.0	3.00	$-0.4453 \mp 0.0151.$	neutron detectors;
0.225	-0.144 ∓ 0.005	49.3	3.40	$-0.4952 \mp 0.0172.$	45°_{LAB} thin targets.
0.240	-0.154 ∓ 0.009	49.5	3.60	$-0.5607 \mp 0.0328.$	
0.275	$-0.147 - 0.006$	49.7	3.98	$-0.5930 - 0.0242.$	
0.385	-0.166 ∓ 0.011	50.3	4.99	$-0.8428 \mp 0.0558.$	
0.500	-0.155 ∓ 0.012	52.4	5.80	$-0.9295 \mp 0.0720.$	as above [11]. symbol
0.620	-0.146 ∓ 0.012	53.0	6.43	$-0.9770 \mp 0.0803.$	46°_{LAB}; thin targets.
0.730	-0.160 ∓ 0.011	53.6	6.76	$-1.1320 \mp 0.0778.$	
0.840	$-0.150 - 0.013$	54.1	6.88	$-1.0860 - 0.0941.$	
0.052	-0.099 ∓ 0.008	52.3	0.43	-0.0440 ∓ 0.0036	
0.087	-0.100 ∓ 0.006	52.9	1.01	-0.1050 ∓ 0.0063	
0.114	-0.122 ∓ 0.005	52.3	1.59	-0.2004 ∓ 0.0082	
0.154	-0.126 ∓ 0.004	51.7	2.23	-0.2890 ∓ 0.0092	
0.165	-0.124 ∓ 0.006	51.9	2.39	-0.3059 ∓ 0.0148	Groningen group [60] x
0.193	-0.136 ∓ 0.004	52.2	2.76	-0.3875 ∓ 0.0114	x symbol MWPC [62];
0.268	-0.162 ∓ 0.005	52.9	3.70	-0.6229 ∓ 0.0192	$46 - 50^\circ_{LAB}$ thin
0.368	-0.166 ∓ 0.004	52.6	4.77	-0.8206 ∓ 0.0198	targets.
0.473	-0.177 ∓ 0.004	53.3	5.51	-1.0178 ∓ 0.0230	
0.586	-0.173 ∓ 0.004	54.0	6.12	-1.1129 ∓ 0.0257	
0.692	$-0.188 - 0.006$	53.4	6.68	$-1.3118 - 0.0419$	

b) Angular distribution measurements. ◻ symbol

E_d (MeV)	a_1	a_2	θ_L	P_n	Sources
0.29	-0.582 ∓ 0.020	-0.011 ∓ 0.016	45	-0.139 ∓ 0.008	Sect. 6.2.1 [37]
0.35	-0.627 ∓ 0.016	$+0.037 \mp 0.014$	45.8	-0.127 ∓ 0.006 [35]	$-0.142 - 0.006$
0.46	-0.801 ∓ 0.029	$+0.011 \mp 0.023$	45	-0.151 ∓ 0.012	Sect. 6.2.1
0.87	-1.008 ∓ 0.027	$+0.051 \mp 0.027$	45	-0.134 ∓ 0.008	[28]
1.10	$-1.069 - 0.037$	$+0.110 - 0.075$	47	$-0.145 - 0.009$	[3]

and shows the compatability of the angular distribution data
with the recent low energy polarization measurements for
$C = -0.155$.

Next the expression of a_1 in terms of the approach cross
sections, σ_ℓ , may be investigated (equation (5)). The σ_ℓ of
BPK [58] (fig. 28a) were empirically derived in a successful
attempt to explain the energy dependence of the differential
cross section in the D-d reaction up to 4 MeV. These parameters
were taken to be model independent within their formalism and
this was upheld by Rook and Goldfarb [59]. The fitting of
equation (5) to the data displayed in fig. 27 may be considered
from two angles: the fit to the measurement of Alsoraya [7] below
300 keV may be optimised and then extrapolated to higher energy
data with modifications as required; alternatively a fit to the
angular distribution measurements available up to 1.1 MeV may
be attempted and this then extrapolated beyond this range to
determine its compatability with other results. Boersma's value
for a_1 at 350 keV [35] as referred to earlier (p.37) was omitted
from these calculations because the corrections required to this
point were unknown.

The computational procedure involved in these best fits is
outlined in Appendix B and the results are detailed in the
adjoining table (Table 5). The magnitude of the errors associated
with the coefficients was taken as a measure of the fit obtained,
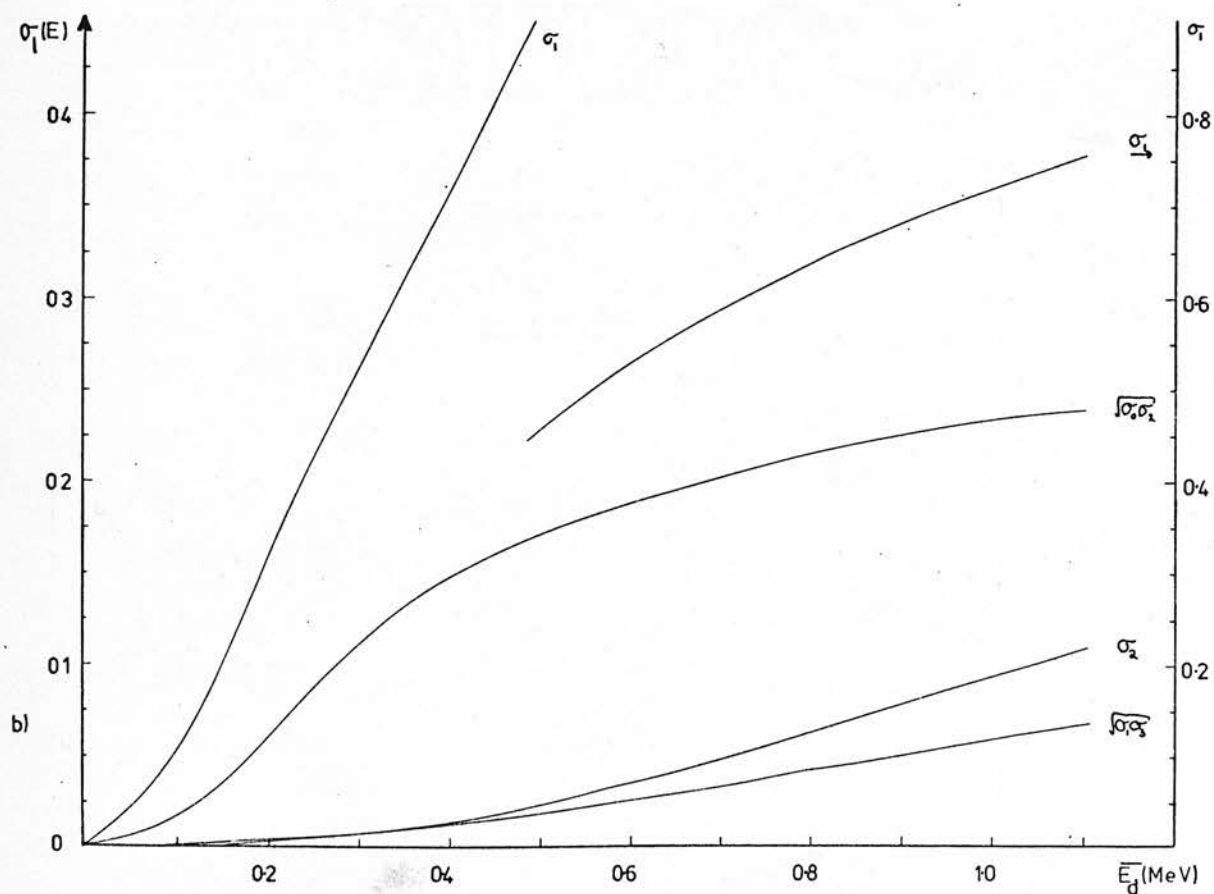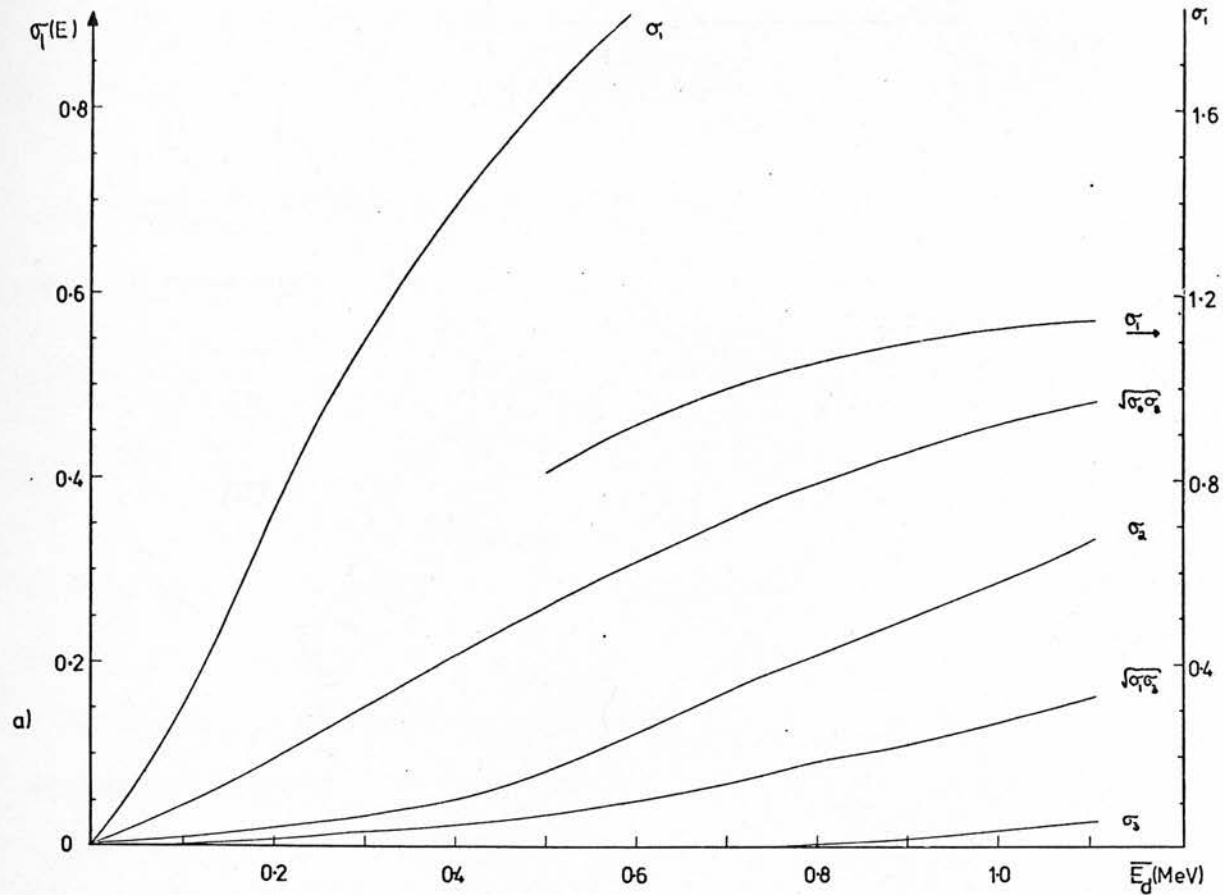and the size of the coefficients gave an indication of the

-47-

Fig. 28 Approach cross sections as functions of the deuteron energy :
a) according to BPK [58], b) according to Boersma – black nucleus
model [42].

Table 5 — Best fit functions for a_1 coefficients in figure 27.

BPK approach cross-sections: figure 29.

0 — 300 keV
$$a_1 = -2.679\ \sigma_1 + 0.095\ \sqrt{\sigma_0\sigma_2}$$
$$\begin{array}{cc} +0.129 & +0.314 \\ -0.129 & -0.314 \end{array}$$
a

0.29 — 1.1 MeV

$$a_1 = -2.295\ \sigma_1 + 10.517\ \sqrt{\sigma_1\sigma_3}$$
$$\begin{array}{cc} +0.093 & +1.364 \\ -0.093 & -1.364 \end{array}$$
b

$$a_1 = 1.022\ \sigma_1 - 7.644\ \sqrt{\sigma_0\sigma_2}$$
$$\begin{array}{cc} +0.324 & +0.939 \\ -0.324 & -0.939 \end{array}$$
c

v

$$a_1 = 1.227\ \sigma_1 - 0.867\ \sqrt{\sigma_1\sigma_3} - 8.161\ \sqrt{\sigma_0\sigma_2}$$
$$\begin{array}{ccc} +1.383 & +4.612 & +3.174 \\ -1.383 & -4.612 & -3.174 \end{array}$$
d

'a' extended to 1.1 MeV
$$a_1 = -2.679\ \sigma_1 + 26.288\ \sqrt{\sigma_1\sigma_3} - 6.971\ \sigma_2$$
$$\begin{array}{cc} +3.369 & +2.228 \\ -3.369 & -2.228 \end{array}$$
e

Boersma black nucleus approach cross-sections: figure 30.

0 — 180 keV
$$a_1 = -3.903\ \sigma_1 + 10.482\ \sqrt{\sigma_0\sigma_2}$$
$$\begin{array}{cc} +0.625 & +2.234 \\ -0.625 & -2.234 \end{array}$$
a

0 — 300 kev
$$a_1 = -4.347\ \sigma_1 + 11.813\ \sqrt{\sigma_0\sigma_2}$$
$$\begin{array}{cc} +0.772 & +2.870 \\ -0.772 & -2.870 \end{array}$$
b

0.29 — 1.1 MeV

$$a_1 = -1.408\ \sigma_1 + 1.167\ \sqrt{\sigma_0\sigma_2}$$
$$\begin{array}{cc} +0.106 & +0.289 \\ -0.106 & -0.289 \end{array}$$
c

$$a_1 = -1.405\ \sigma_1 + 1.152\ \sqrt{\sigma_0\sigma_2} + 0.015\ \sigma_2$$
$$\begin{array}{ccc} +0.106 & +0.289 & +0.013 \\ -0.106 & -0.289 & -0.013 \end{array}$$
d

$$a_1 = -1.613\ \sigma_1 + 2.086\ \sqrt{\sigma_0\sigma_2} - 1.322\ \sqrt{\sigma_1\sigma_3}$$
$$\begin{array}{ccc} +0.239 & +0.962 & +1.329 \\ -0.239 & -0.962 & -1.329 \end{array}$$
e

'a' extended to 1.1 MeV
$$a_1 = -3.903\ \sigma_1 + 10.482\ \sqrt{\sigma_0\sigma_2} + 8.779\ \sqrt{\sigma_1\sigma_3} - 9.003\ \sigma_2$$
$$\begin{array}{cc} +2.002 & +0.946 \\ -2.002 & -0.946 \end{array}$$
f

importance of different terms. The fitting procedure was applied
to σ_1 and combinations of one or two other approach cross
sections.

Firstly the σ_ℓ of BPK were considered. Examination of fig. 28a
indicates that only σ_1 and $\widehat{\sigma_0 \sigma_a}$ terms might be expected to
contribute at low energies, and the best fit ('a') indicated that
the latter was insignificant; however at higher energies it
appears that the $\widehat{\sigma_1 \sigma_3}$ term makes a strong contribution (fit 'b').
Figure 29 illustrates these fits. The relation 'b' has been
extended (dashed curve) to lower energies to indicate the
tolerance on the σ_1 coefficient value. The fit 'a' was taken as
giving the correct σ_1 dependence and the fitting procedure used
to determine appropriate coefficients for the σ_a and $\widehat{\sigma_1 \sigma_3}$
terms which become significant above 0.25 MeV. This led to the
parameterization 'e' with somewhat larger errors and is also
shown on figure 29. This procedure may be successfully pursued
to higher energies with the use of a σ_3 term but doubt has
already been cast on this as an aid to theoretical interpretation.
The two fits agree satisfactorily as to the basic σ_1 dependence
and thread the given data points in an acceptable manner. In
particular the 46°_{LAB} measurements of this group from 500 to
900 keV [11] are compatible with these curves though they were not
used in the fitting procedure. Fits 'c' and 'd' were discarded
when judged by these criteria and because of their larger
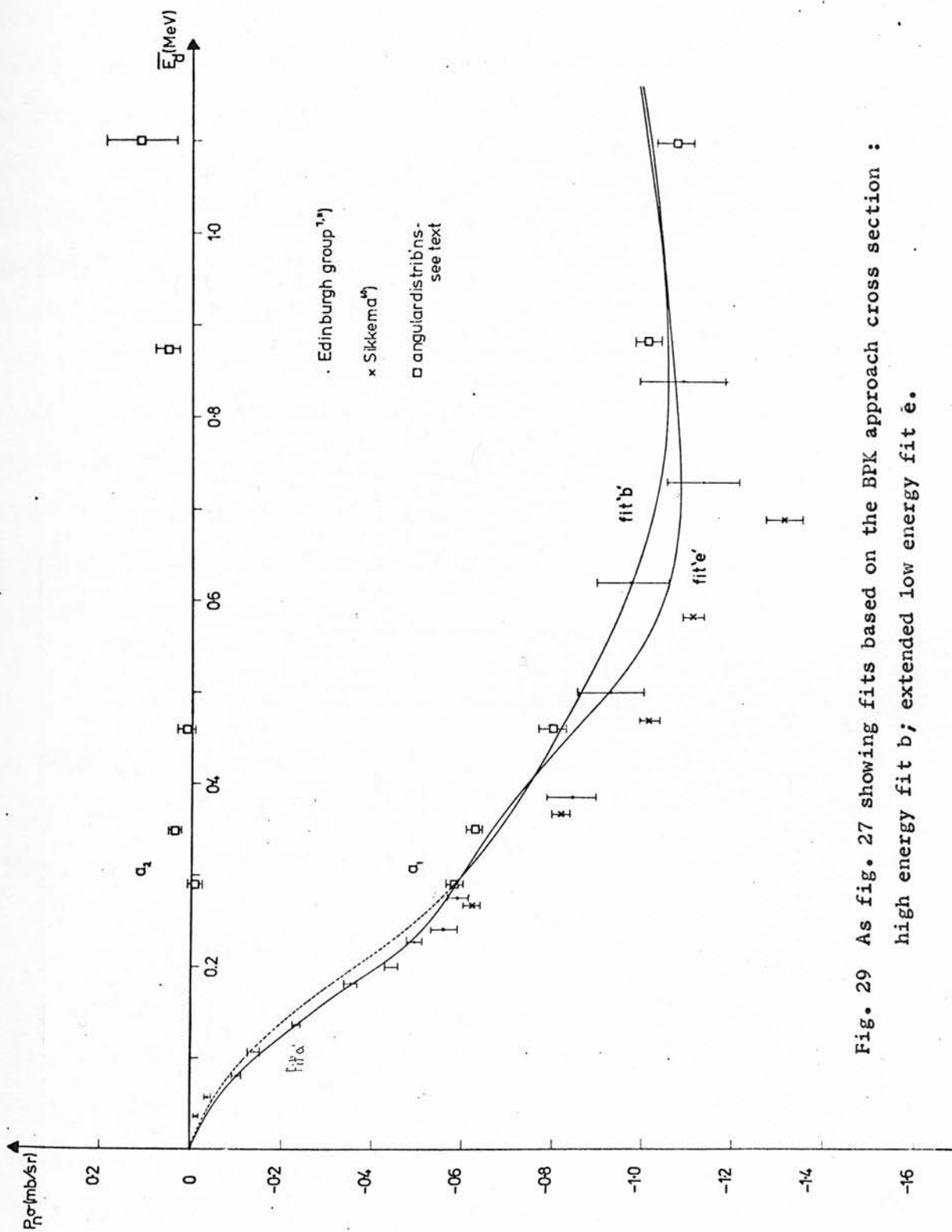coefficient errors.

Fig. 29 As fig. 27 showing fits based on the BPK approach cross section :
high energy fit b; extended low energy fit b.

Secondly Boersma has produced approach cross-section plots [42]
derived on the basis of black nucleus and hard sphere models. This
he did to illustrate a criticism of the supposed model independence
so fundamental to BPK's theoretical discussion. Performing a
similar analysis with Boersma's black nucleus σ_ℓ (fig. 28b)
produces the fitting equations in Table 5, of which two are shown
on figure 30. The treatment is complicated by the need to
consider contributions by $\sqrt{\sigma_0 \sigma_3}$ and σ_2 terms down to 150 keV
and by the apparent importance of the $\sqrt{\sigma_0 \sigma_2}$ term. Thus the
extrapolation to higher energies took fit 'a' as giving the
basic dependence, the resulting parameterization ('f') bore
little resemblance to the dependence indicated in fits to the
0.3 - 1.1 MeV data. The fit 'e' was selected as giving the best
fit at higher energies.

Boersma's hard sphere σ_ℓ failed to give a converging fit
as might be expected since all but the σ_0 term are practically
zero below 300 keV, thereby excluding the possibility of their
use in explaining low energy polarization measurements.

These calculations have confirmed the model dependence of
the approach cross-section formalism as argued by Boersma.
However, the σ_ℓ of BPK are more realistic, being empirically
derived from angular distribution measurements, and also in
their favour is the consistency of dependence indicated by best
fit relations derived for different energy ranges. For these
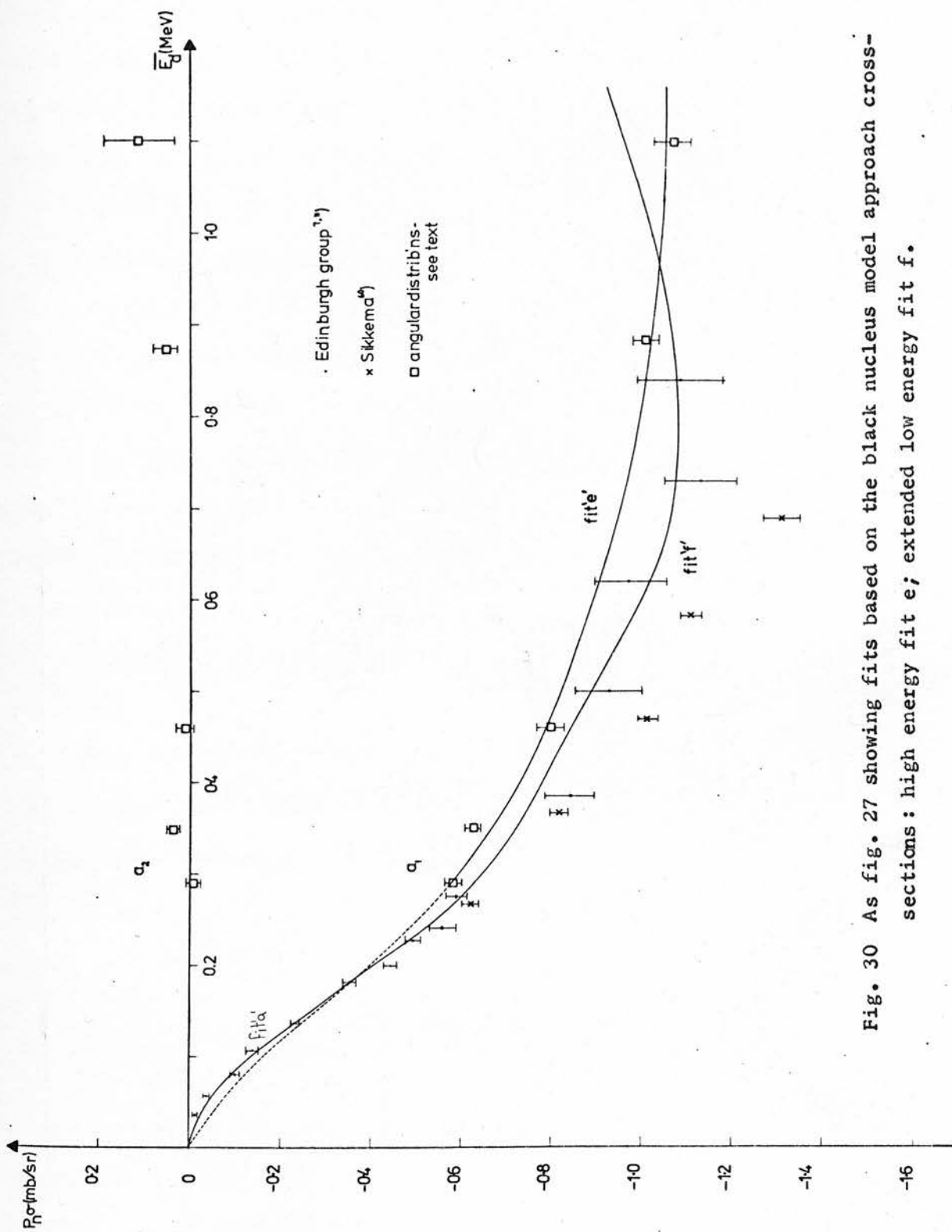reasons these fitting relations have greater promise as a useful

Fig. 30 As fig. 27 showing fits based on the black nucleus model approach cross-
sections : high energy fit e; extended low energy fit f.

means of parameterizing the differential polarization. In common with all other σ_ℓ sets however, there are significant discrepancies in the fit below 200 keV which are only avoided in the low energy approximation fit (fig. 27) which relies strongly on recent measurements of $\sigma(\theta)$ in this region.

The theoretical interpretation is similarly confused by the appearance of model dependence. Whereas the BPK σ_ℓ give rise to a_1 relations involving σ_1 and $\sqrt{\sigma_1\sigma_3}$ but not $\sqrt{\sigma_0\sigma_2}$, the Boersma σ_ℓ lead to a marked though ill-defined dependence on $\sqrt{\sigma_0\sigma_2}$. Thus on the basis of the former Fierz' analysis (p. 32) would lead one to conclude that l.s coupling is not involved in the interaction but in the latter leads to the reverse conclusion.

6.3.1 Neutron - helium scattering.

The analysing power in n-^{4}He elastic scattering for a particular angle and incident neutron energy may be determined using the formula:

$$P = - \frac{2\mathfrak{I}_m(g^*h)}{g^2 + h^2} \qquad 64) \text{ and internal report }^{16)} \text{ for definitions.}$$

and a selected set of phase shifts. At an applied level such phase shift sets may be regarded as a convenient parameterization allowing interpolation between energies for which actual measurements are available. There are slight inconsistencies between the reported phase shift sets but

it has recently been shown [4] that these variations appear as quite gross differences in the forward scattering analysing power (even selecting data reported in the last decade) and that the situation deteriorates with increasing incident neutron energy.

A knowledge of the phase shifts and their energy dependence may lead to a physical understanding of the nuclear potential involved or to some model representation of the interaction. Thus it is very important to have accurate n-^{4}He phase shifts, for both theoretical and experimental reasons.

Some independent means of checking the analysing power is therefore required. One possible approach is to use a source of neutrons with accurately known polarization [67]. However for the D-d neutrons determinations of polarizations have been plagued by discrepancies greater than the attributed errors. Double scattering experiments on ^{4}He offer a way of overcoming this , but such techniques suffer from very low counting rates and extreme background problems [68]. The approach adopted in the presently reported experiment is to investigate the ratio of analysing powers at backward and forward angles. Since there is fair consistency in the value of the derived analysing power in the region of about 120°_{LAB} up to 15 MeV such an experiment can test the value of analysing power at about 60° with some sensitivity.

The left-right asymmetry in the scattering of polarized neutrons is directly proportional to the analysing power according to:

$$\mathcal{E} = P_n A(\theta)$$

In the polarimeter as described this means that the ratio of the asymmetries measured in the backward and forward detectors is equal to the ratio of the corresponding analysing powers. In practice these analysing powers are weighted means obtained with due account of features of the geometry and reaction cross-section. It is also important to approach the derivation of asymmetries from the recoil spectra in the same manner for all sets of data.

The spectra shown (fig. 31) are the product of a continuous 300 hour run under uniform machine conditions. The polarimeter was sited at a lab angle of 45° with an incident deuteron energy of 340 keV. The target was of the same material as used for the angular distribution measurements but the target finger was angled at 45° giving an effective target thickness of 150 keV. Consideration of the yield curve for this target (fig.36)[19] gave a mean incident deuteron energy of 273 keV and a corresponding neutron energy of 2.97 MeV at $45^\circ{}_{LAB}$. The dimensions of the target were 3 x 20mm, the long side being in the reaction plane and the alignment achieving concurrence of the colimator/polarimeter axis and the target surface to $\pm$ ½mm.
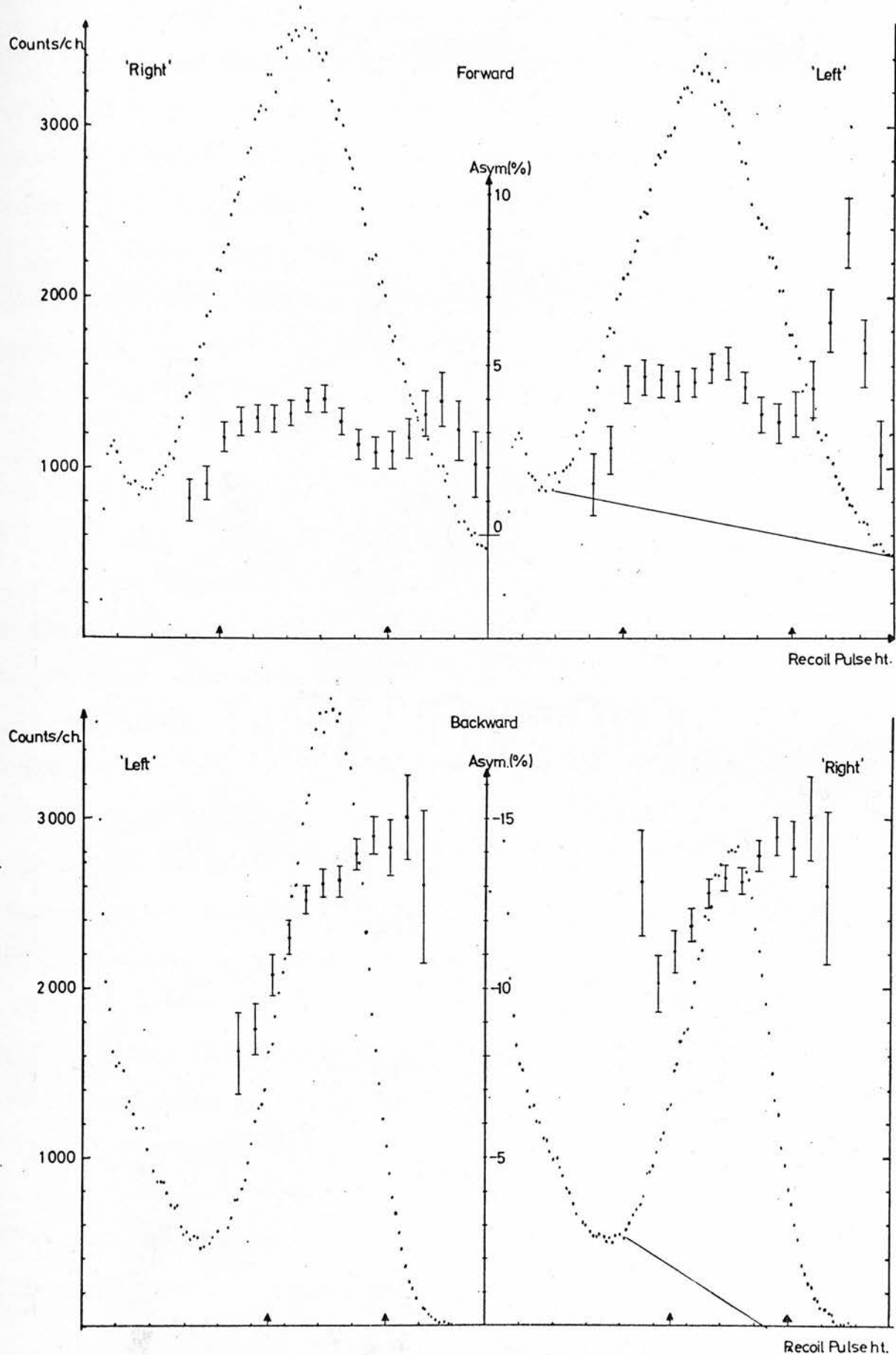
Fig. 31 Recoil spectra obtained for forward and backward scattered neutrons
of 2.97 MeV mean energy; asymmetries shown with and without tail
correction.

The geometrical position of the side detectors in the polarimeter corresponded to n-^{4}He lab scattering angles of 117° and 55°. A weighted mean of scattering accounting for finite volume, beam dispersion, and helium differential cross-section, $\sigma_{He}(\theta)$, shows that these angles are more correctly quoted as 116.9° and 53.5°. The greater adjustment required to the forward scattering is associated with the rapid variation of $\sigma_{He}(\theta)$ in this region (fig.32)

6.3.2 Analysis and interpretation of n-^{4}He scattering.

The asymmetries derived from the spectra of fig.31 are -0.1288 $\pm$ 0.0025 for backward scattering and +0.0460 $\pm$ 0.0027 for forward scattering. The errors given account for uncertainties in tail corrections as well as statistical error limits. The value of the neutron polarization under these experimental conditions has been independently evaluated as 0.15 $\pm$ 0.01 using the small angle scattering technique. From these figures the backward and forward effective analysing powers may be determined as respectively 0.86 $\pm$ 0.02 and -0.31 $\pm$ 0.01 and these values may be compared with those obtained using various phase shift sets. Alternatively the ratios of asymmetries and of analysing powers at backward and forward angles may be directly compared.

These comparisons are made on Table 6 which also shows the effect of further corrections. The analysing powers from various
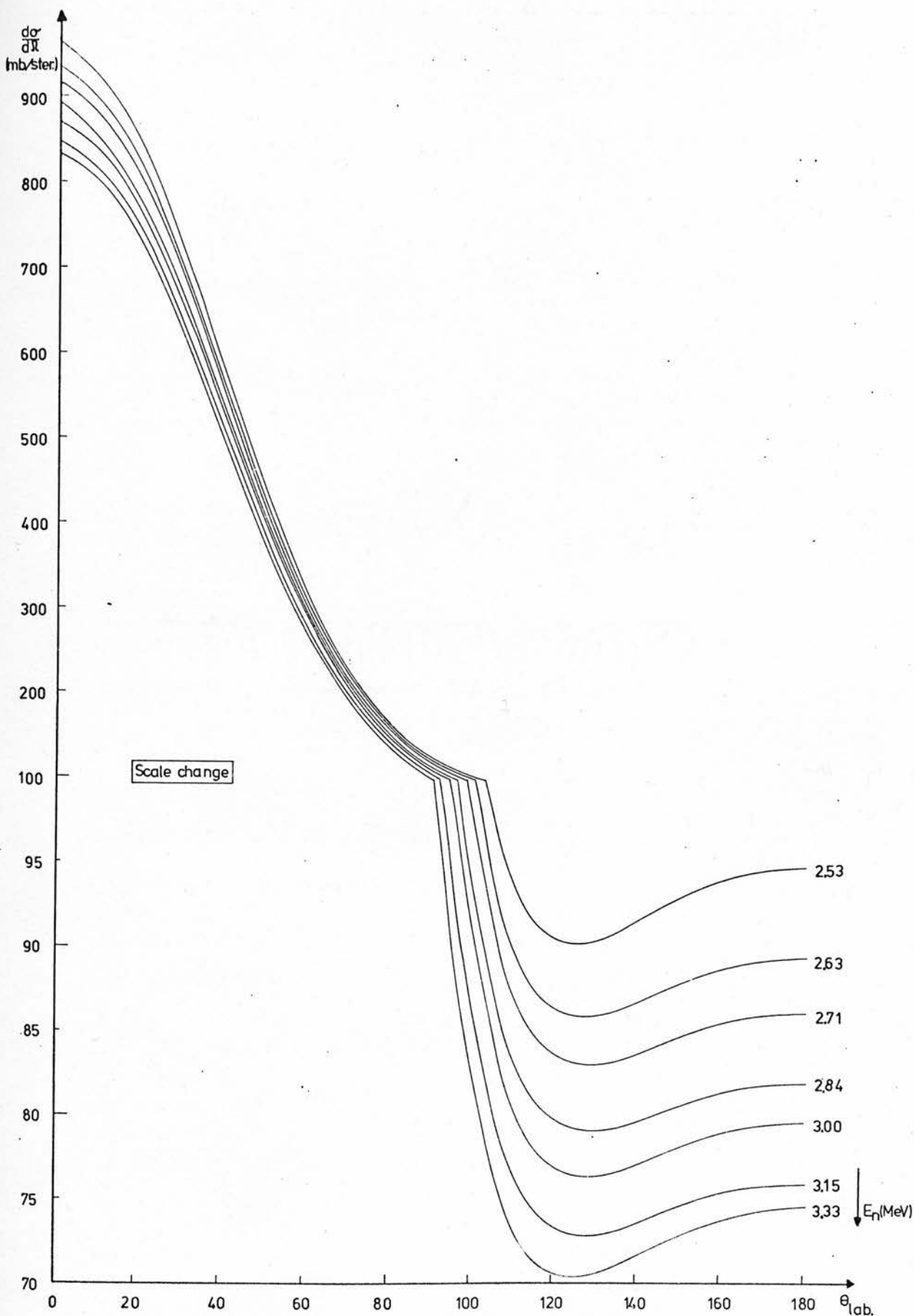
Fig. 32 The differential cross-sections for n-^{4}He elastic scattering derived from the phase shift set of Stammbach and Walter [73].

Table 6 — Measured and derived data for backward/forward n-^{4}He scattering.

$\overline{E}_d$ = 270 keV, target thickness = 195 keV, E_n at ~45° $_{LAB}$ = 2.97 MeV,

$P_n = 0.15 \pm 0.01$ [5].

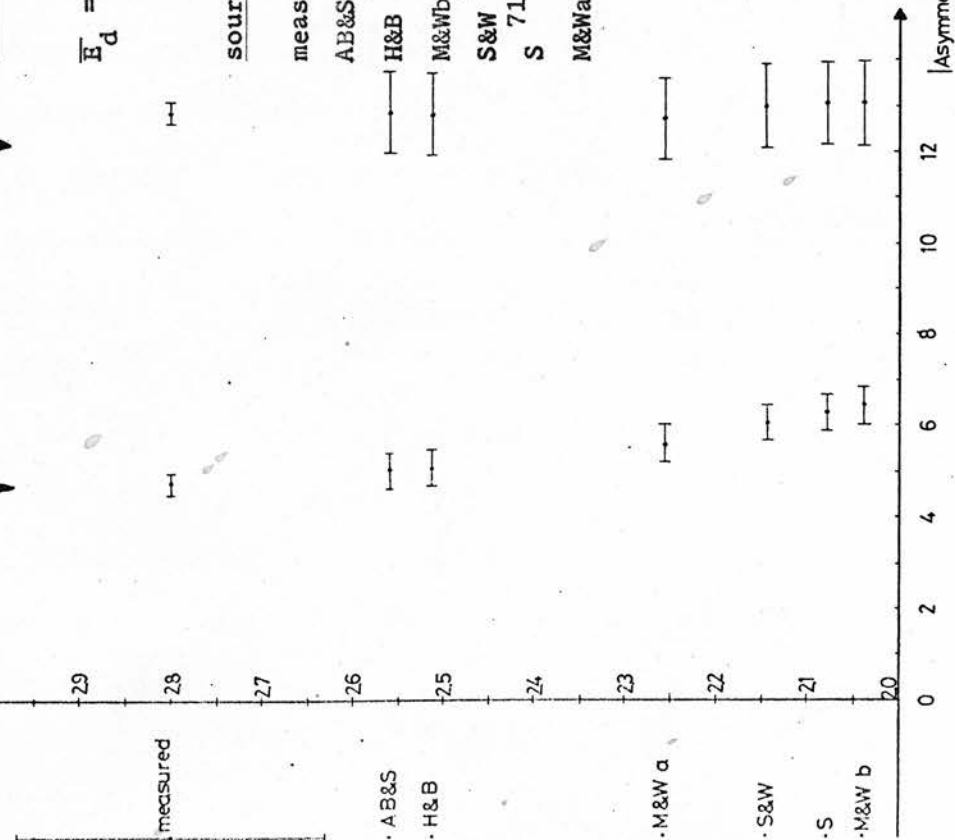| source	Backward $A(\theta)_{2.97}$	$\langle A(\theta)\rangle$	$|\varepsilon|$	Forward $A(\theta)_{2.97}$	$\langle A(\theta)\rangle$	$|\varepsilon|$	Ratio
measured	-	0.86 ± 0.02	0.1288 ± 0.0025	-	-0.31 ± 0.01	0.0460 ± 0.0027	$2\cdot8\pm0\cdot1$
AB&S [69]	0.856	0.858	0.1287	-0.331	-0.335	0.0503	2.56
H&B [70]	0.854	0.860	0.1290	-0.352	-0.353	0.0530	2.52
M&Wb [17]	0.870	0.871	0.1307	-0.424	-0.424	0.0641	2.04
S&W [73]	0.865	0.865	0.1298	-0.402	-0.403	0.0605	2.15
S [71]	0.868	0.869	0.1304	-0.419	-0.418	0.0627	2.08
M&Wa [17]	0.847	0.847	0.1271	-0.372	-0.375	0.0563	2.26

Fig. 37 Back/forward ratios from measured asymmetries compared with predictions of various phase shift sets for this geometry, and the asymmetries derived from an independent value of 0.15 ± 0.01 for the polarization.

phase shift sets are listed for the mean energy of neutrons incident on the helium cell. In practice the range of neutron energy was 2.86 to 3.04 MeV and bearing in mind the rapid variation of analysing power with energy (fig.33) a more rigorous approach was considered advisable. Deriving the geometrically weighted mean analysing powers for backward and forward scattering it is found (fig.34) that the analysing power is a more strongly increasing function of energy at forward angles. The ratio of analysing powers adjusted for the present geometry at backward and forward angles is therefore a decreasing function of energy and figure 35 shows this for two phase shift sets. Folding the yield curve (fig.36) into this variation over the appropriate neutron energy range therefore gives a weighted mean for the ratio. In these two selected cases the respective values were 2.16 and 2.46 rather than 2.15 and 2.53 as obtained taking analysing powers at the mean neutron energy. While it thus appears the correction required to the ratios was negligible, similar treatment applied separately to the backward and forward analysing powers pointed to a significant correction in the latter case. Modified values were therefore obtained for the analysing powers (Table 6), using a similar though coarser folding procedure which gave asymmetries which would realistically be expected on the basis of these several phase shift sets.

The pictorial representation of this data (fig.37) page before makes clear that while the ratio of backward and forward scattering fails to agree with the predictions of any phase shift set, the

-54-
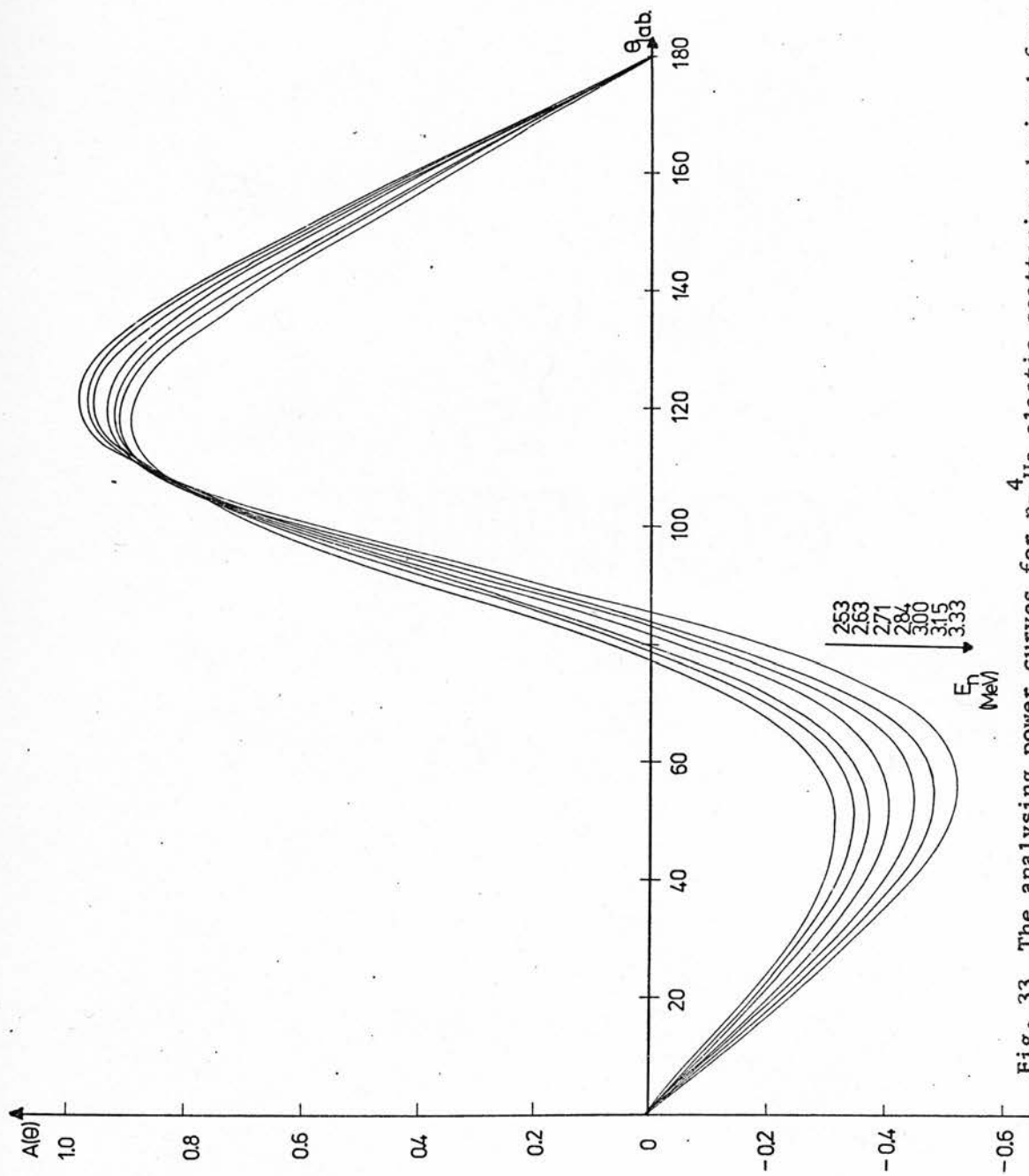
Fig. 33 The analysing power curves for n-^{4}He elastic scattering derived from the phase shift set of Stammbach and Walter [73].
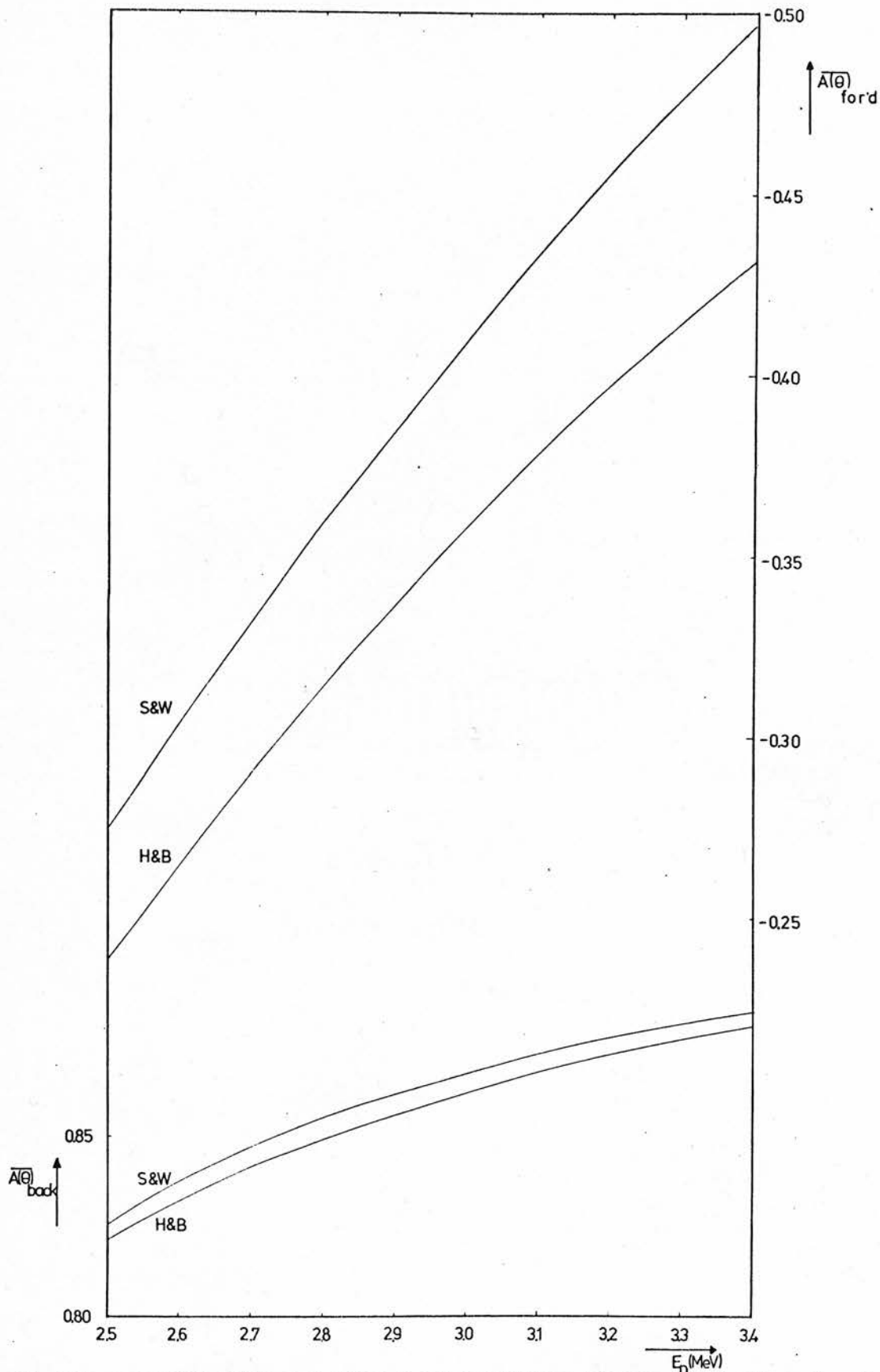
Fig. 34   The geometrically weighted mean analysing powers for backward and
forward n-^{4}He scattering as a function of neutron energy (derived
from the phase shift sets of Stammbach and Walter [73] and Hoop and
Barschall [70]).

Fig. 35 The ratio of analysing powers in figure 34 as a function of neutron energy

Fig. 36 The yield curve for the D(d,n)^{3}He reaction as a function of neutron energy with corresponding deuteron energy scale for observations at 45° LAB.

derived asymmetries are compatible with those obtained using the Austin et al [69] or Hoop and Barschall (H & B) [70] phase shifts.

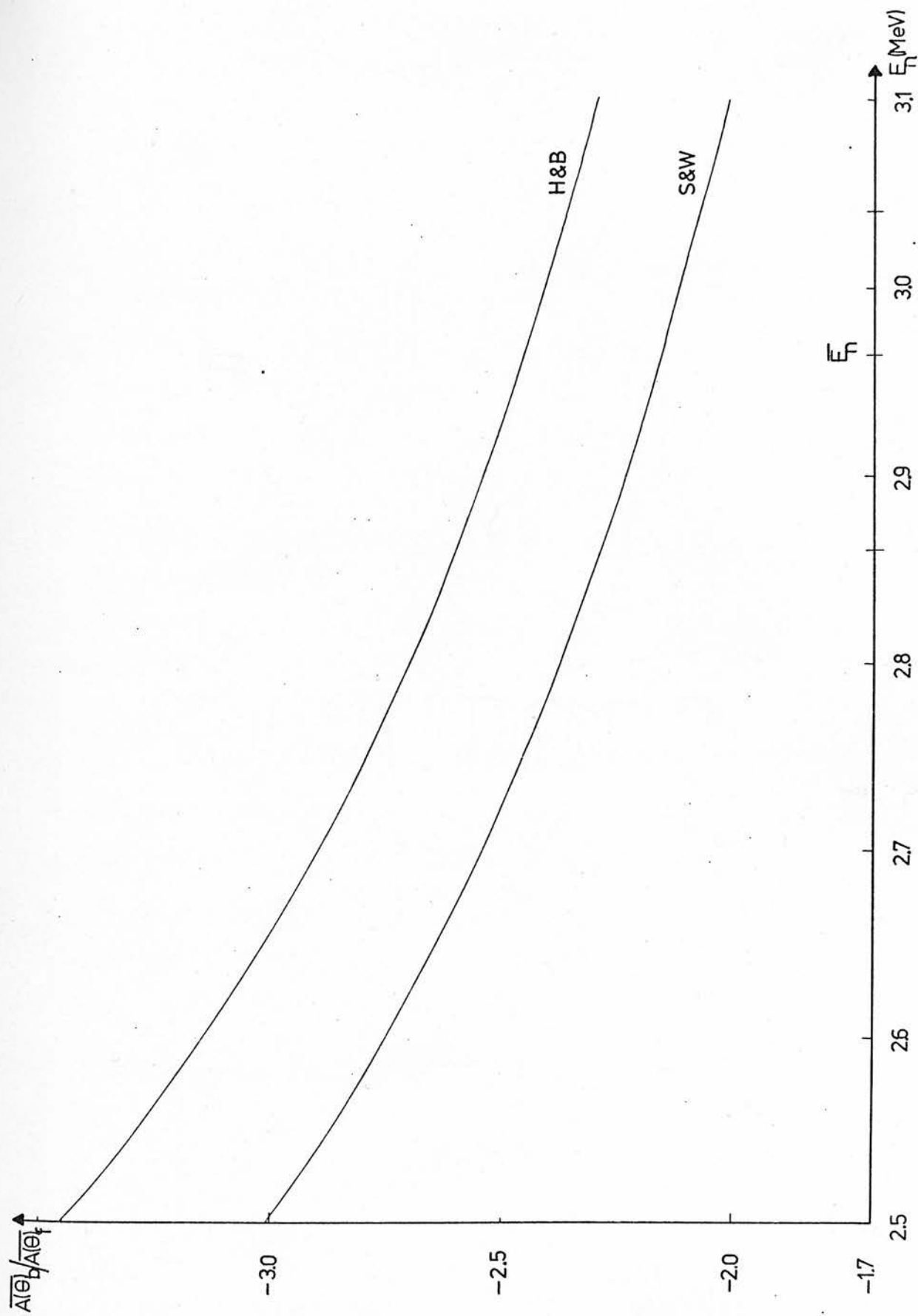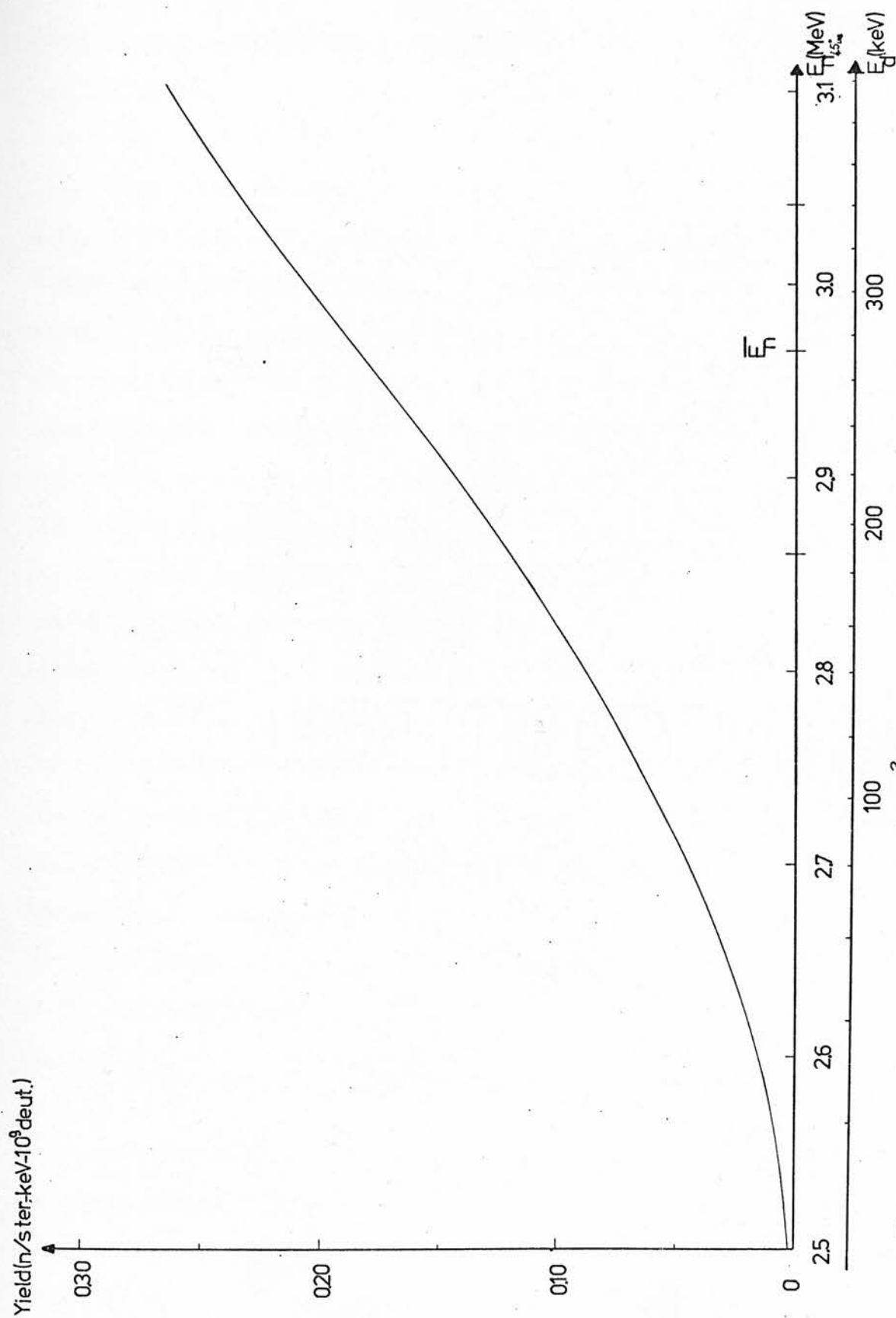Some caution should be exercised in interpreting the present data too widely. Firstly the experimental technique samples the analysing power over a range of angles and a finite neutron energy range. Secondly, the phase shift sets with which comparisons may be made do not in most instances use data obtained with 3 MeV neutrons. Thus reliance is placed on interpolations between well separated measurements and though the phase shift sets may be satisfactory at these points their general acceptability is not to be relied upon. The preference for the analysing powers resulting from Austin's [69] and Hoop's [70] work is supported by Sikkema who using χ^2 test on his 3 MeV neutron polarization data found a markedly stronger compatability with their data rather than Stammbach and Walter's [73]. This may be attributed to the inclusion by Austin of a differential cross-section measurement at 3.02 MeV. Such a neat explanation is not available in Tornow's [68] double scattering experiment with 15 MeV neutrons where he found in favour Hoop and Barschall's and Satchler's [71] phase shifts; neither of these rely on measurements at this energy.

Certain points of experimental significance should be borne in mind at this stage. In its use as an analyser, n-^{4}He scattering is normally observed at backward angles where the figure-of-merit $A^2 \sigma_{He}$ [72] is good, there is greater agreement as to the

value of A, and background problems are reduced. Conversely tests to determine preferred phase shift sets are insufficiently sensitive under such conditions. Only a comparison technique such as is here reported, or a double scattering experiment (with its attendant low counting efficiency) has the sensitivity required. By implication also the data reported in sections 6.1 and 6.2 is affected to only a negligible extent by the choice of phase shift set.

Figure 38 illustrates the disparity in the predictions of analysing power from 4 to 18 MeV neutron energy. If further measurements of the kind discussed can help point towards the gross variation of analysing power with energy this will assist the experimenter in selecting the best phase shift set over a particular energy region. However it appears that the best solution is the accurate determination of the analysing power at discrete energy intervals. This will set more exacting requirements on the model interpretations underlying the parameterizations attempted and serve a useful purpose both for the theoretician and the experimenter.
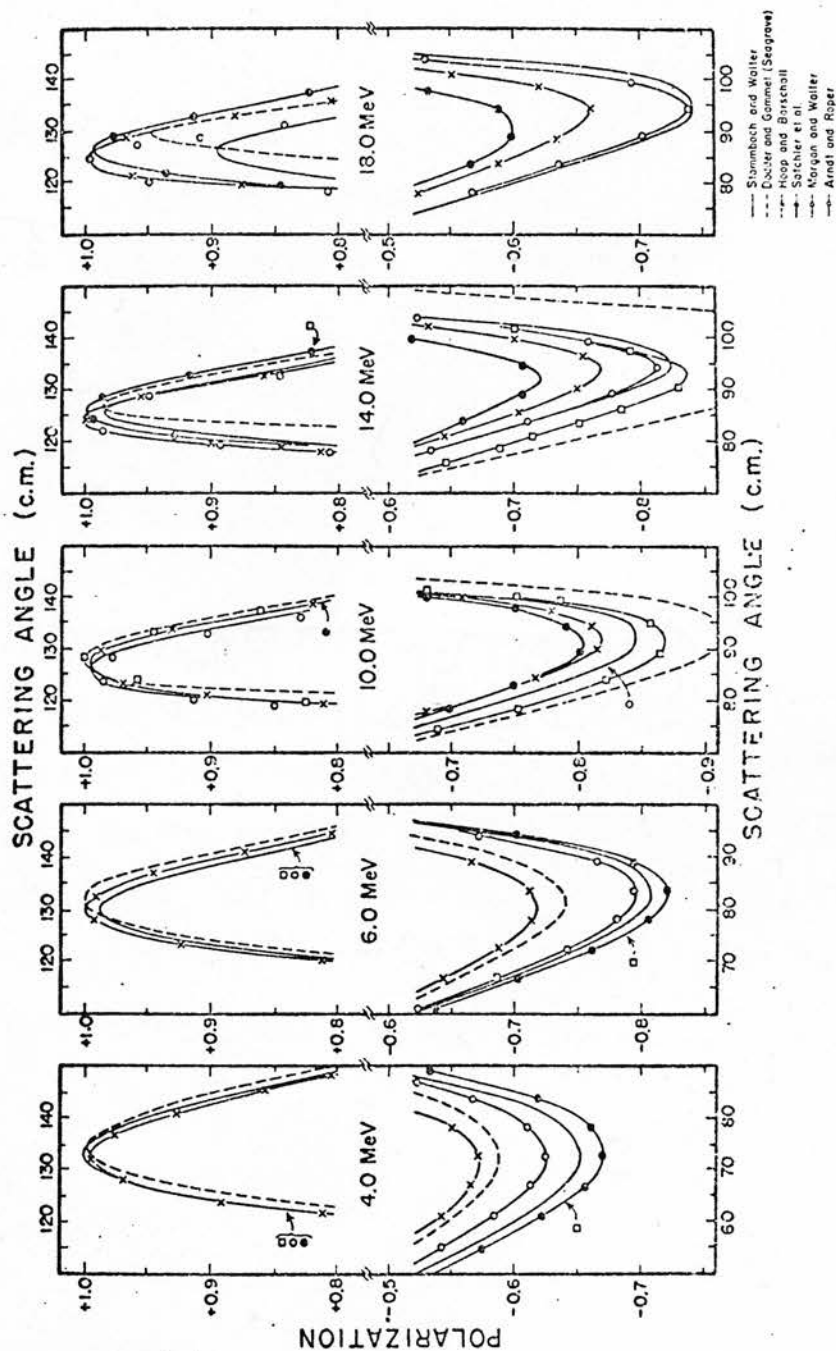
Fig. 38 Polarization for n-^{4}He scattering from 4 to 18 MeV for available sets of phase shifts.

CHAPTER 7.

SUMMARY.

7.1 Review.

It is apparent from the discussion in the previous chapter
that even in the simple systems under consideration our
understanding is far from complete. However, the general agreement
in polarization measurements has improved even since the recent
review of Fiarman [77], of Galloway [2] and of Walter [37] and a
definite trend appears to have been established by the
consistent observations regarding n-^{4}He scattering. It has been
shown in the former case that a successful parameterization of
the polarization may be achieved from 0 to beyond 1 MeV incident
deuteron energy. In the latter case the viability of the ratio
technique has been demonstrated as a means of selecting which of
the n-^{4}He phase shift sets are most satisfactory and this has
been successfully performed at 3 MeV neutron energy where the
distinction between alternative analysing power curves (fig.38)
is comparatively small.

The gap between theory and practice may not have closed to
a corresponding extent but the present work has pointed to the
important considerations, and the inconsistencies to be avoided.
Recently such disparate approaches as DWBA and R-matrix theory
have been applied to both the D-d system and n-^{4}He scattering

and attention has been drawn to the uncertain role of the direct interaction in the former system. No attempt has here been made to improve the existing theory or to substitute an alternative, but rather to draw together evidence of the existence of competing processes and to interpret the areas of relevance of the various approaches.

In some cases with the aid of fuller interpretation of the theory, the available observations may more usefully be employed. With reference to Hardekopf's proposal [41] to bring into line with one another the proton and neutron polarizations from the D-d reaction it is found that his observations may be used to augment the existing n-polarization data in the 4 - 5 MeV region. These observations are indicated on Table 1 but not on the accompanying graph, where they would tend to support the trend of the measurements obtained by the Duke and Edinburgh groups [27,3].

To a large extent the work for this thesis was a design project and the earlier chapters have encompassed the various additions, modifications and treatments considered necessary in these experiments. The effort has been justified by the improved functioning of the helium scintillator and the need for a variety of detector orientations in the measurements of angular distributions and backward/forward scattering ratios; the nature of these experiments (in particular the obtaining of good statistical accuracy despite low counting rates) also demanded the maintaining of long-term stability of accelerator running

conditions and a computer orientated approach to data collection and analysis. Besides their immediate and practical applications many of these treatments have significance beyond the confines of the present design project. Specifically, the conclusions regarding coating materials and sealing techniques in the helium scintillator have wider implications and the use of beam profiles to investigate attenuation and scattering in neutron beams, has possible uses in other situations. Similarly the design of the electronic systems was approached with an eye to their application in other experiments and their adaptability to other situations has been demonstrated.

At a slightly different level a critical assessment of the experiment led to a fuller appreciation of the sources of error involved. Some of these could be overcome by improved design as in the case of the helium scintillator, some involved correction procedures as in the case of the target yield-energy relation and in one instance more 'generous' error limits were ascribed as a result of an analysis of the source and extent of the recoil spectrum tail correction.

7.2 Further studies.

Further progress in the investigation of the D-d reaction may usefully concentrate on theoretical interpretation. In so much as the disparities in recent observations of neutron polarization are small, though still significant, some consensus

-59-

as to the trend is being achieved. As mentioned earlier the one hiatus in experimental measurements remains the 0.5 - 3 MeV region for polarized deuteron beams and data from these investigations may well indicate as to the existence or otherwise of broad resonances in the compound nucleus state. However, the chief interpretive problems concern the rôle of the direct interaction in this system and the gross features of the neutron polarization over the energy range 0 - 40 MeV as reviewed by Walter [37].

The investigations of n-^{4}He scattering at higher energies could usefully apply the new technique described here. Figure 38 has illustrated that even up to 15 MeV neutron energy there is fair agreement on the analysing power at backward angles while the disagreement at forward angles is considerably more marked than at 3 MeV, thereby improving the likelihood of obtaining a positive indication as to the most satisfactory phase shift set. Here also the theoretical interpretation is falling well behind the pointers provided by the recent experimental observations.

In conclusion it may be observed that the very properties of the D-d reaction that most strongly argue the existence of direct interaction effects could usefully be employed to provide a source of polarized neutrons for the n-^{4}He scattering ratio technique. Simmons[46] has pointed out that of all the available neutron sources, the D(d,n)^{3}He reaction at 0° gives the highest $P^2\sigma$, a factor of 70 greater than obtained with an

unpolarized deuteron beam, and this holds true over the whole
of the neutron energy range, 5 to 17 MeV, where the forward
analysing power of n-^{4}He scattering is most in need of
investigation.

Appendix A : Electronics.

A1. Belt Charge Stepping Motor Control unit.

To obtain stable running conditions with the Van de Graaff
accelerator, the corona points are positioned to draw about
$30 \mu A$ at the required terminal voltage. The stabiliser system of
the machine corrects for any change in the direction of the
analysed beam by furnishing a correction signal to the control
grid of the corona current control tube which controls the flow
of corona current. Some variation in the current drawn must be
tolerated therefore. However, long term drifts in corona current
associated with changes in belt condition, loading and gas
insulating properties must be corrected for by adjusting the
charge carried on the belt. The h.t. supply associated with the
belt charge receives its mains supply through a variac to
provide manual control. The shaft of this variac has been coupled
to a stepping motor with its own control unit to automate the
corrective action required when large variations in corona
current occur.

The transgressions by the Van de Graaff corona current of
manually set limits on a Sifam $100 \mu A.F.S.D.$ meter produces logic
transitions which may be used to activate the unit. (Fig A1)
The meter incorporates adjustable pointers bearing photosensors,
a light source and a meter needle with a vane attached near its
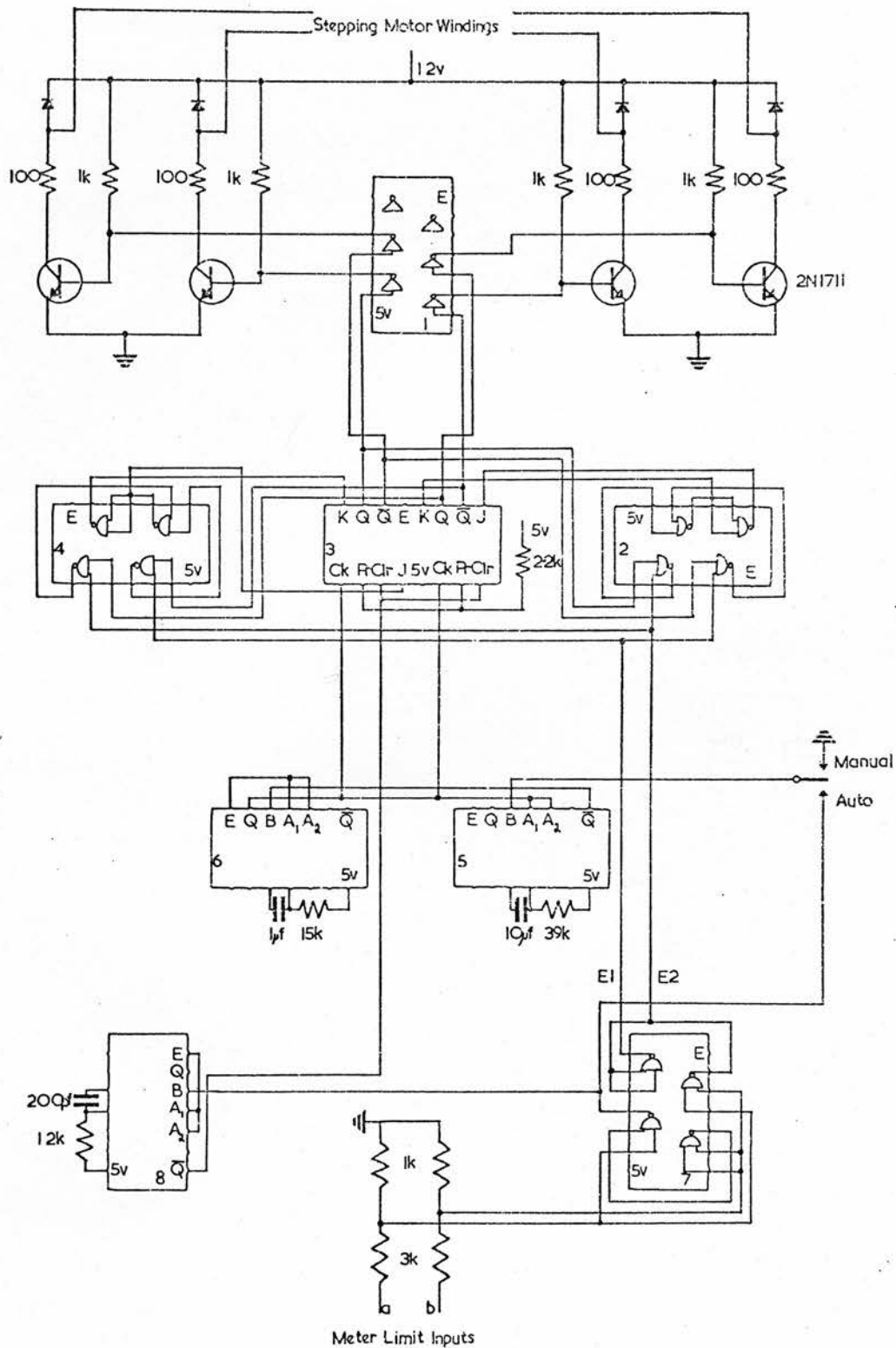base. According to the needle and vane position, the light beam

Fig. Al. Belt Charge Stepping Motor Control unit.

may fall on both sensors, or one or both may be in shadow. The photosensors' outputs are passed through amplifiers to provide logic levels and a current sourcing capability of 120 mA. A meter was selected for this monitoring task because of the elevated voltage at which the corona line is held which complicates the design of an electronic circuit solution to this problem. The visible setting of the limit pointers to correspond to desired limits, and their relation to the actual corona current is a further advantage of this solution. Applying the states associated with the upper and lower limits to 'a' and 'b', the 12 volt logic is first made compatible with TTL (transistor-transistor logic) by a resistor divider. Input 'a' registers a high-low transition as the current crosses the upper limit, and input 'b' registers a low-high transition as the current crosses the lower limit.

When corrective action is required a monostable (I.C.8) provides a clear pulse to initialise the JK flip-flop (I.C.3) responsible for the stepping motor pulse pattern and, if auto is selected, the oscillator (I.C.s 5-6) is armed to provide the clock pulse train (frequency about 200pps). The direction of rotation required of the stepping motor is determined (I.C.7) and signalled by E_1 (logic '1' if under-range) and E_2 (logic '1' if over-range). Accordingly the flip-flops (I.C.3) execute one of two cycles at the dictate of cross coupled nands (I.C.s 2,4) and the Q, $\bar{Q}$ outputs are buffered to give current sourcing capability.

The sequence of Q, $\bar{Q}$ states is such as to cause the required direction of stepping motor rotation. Each step corresponds to the setting up of a particular field direction in each of the two stators of the motor. The oscillator in the control unit clocks the next step which which will cause clockwise or anticlockwise rotation according to the new state of the Q, $\bar{Q}$ flip-flop outputs and the corresponding stator fields. Since each switching process causes a rotation of $7^{\circ}30'$ the movement is sensitive, and the clock frequency is adjusted to avoid 'hunting' while still giving rapid response.

When the accelerator is switched on, this provides power to the stepping motor control unit and switching off by either automatic or manual means switches off the unit.

A2. Fault Monitoring System.

This system was devised to monitor and indicate the occurrence of undesirable machine or beam conditions and to cause accelerator shut down in the event of certain faults occurring during unattended operation.

The circuit is illustrated in fig. A2. It is designed to work in one of three modes: the manual mode in which the status of various parameters associated with the machine are visually indicated on a 'green for go' basis (this includes sufficient cooling water flow to the Van de Graaff pressure tank, column diffusion pump baffle, viewers, slits, magnet box and targets, temperature sensing of liquid nitrogen in all diffusion pump traps, gate valves open and beam viewers out) and for general faults on a 'red for no go' basis (target beam current outside acceptable range, pressure tank over temperature limit, machine room door open, or end of experiment reached); the alarm mode in which a fault associated with the conditions relevant to the beam line and target in use would result in an audible alarm sounding; the auto mode in which the occurrence of any 'no-go' fault is recorded on the appropriate LED (light emiting diode) indicator until reset and the persistence of any relevant fault for a selected time up to 3 seconds results in accelerator shut down.

The beam line/target used is selected by the setting of analysing magnet supply polarity, or by inserting a target before

Fig. A2. Fault monitoring system.

the analysing magnet (fig.A3). Thus a logic '0' is produced corresponding to the line selected. I.C.11 allows the insertion of the target to over-ride the selection of any other beam line. The line selected is indicated by an LED.

The circuit diagram shows the fault sensors schematically. These sensors are wired to give a logic '0' for a fault condition and buffered to LEDs and nand gates which only produce a logic '0' if a fault occurs on the selected beam line. The state of gate valves and viewers are indicated (not shown on figure) but do not register faults since a 'beam current low' would occur if they were incorrectly positioned.

The general 'no-go' faults are treated differently. The transgression by the target beam current of manually set limits on a Sifam 100 μ A.F.S.D. meter (see A1) produces 12v. logic transitions which are made compatible with TTL by a resistor divider. The 'beam low' input registers a low-high transition and the 'beam high' input a high-low transition for the corresponding conditions. From this is derived (I.C.s 4,5) a 'fault = '0', OK = '1'' indication which is 'nanded' with similar indications from the tank temperature sensor, door open sensors, and end of experiment line. When alarm or manual mode are selected (switch bounce protected by I.C.5) the enable inputs of latch bistable 8 are held high presenting the fault levels to the red LED indicators but in auto mode the occurrence of a fault fires a monostable (I.C.7) creating a latch pulse so

Fig. A3 Plan view of accelerator beam lines with fault sensors.

that the occurrence of a transitory fault is stored by the latch and registered on the appropriate LED. Subsequent faults reset and repeat this process.
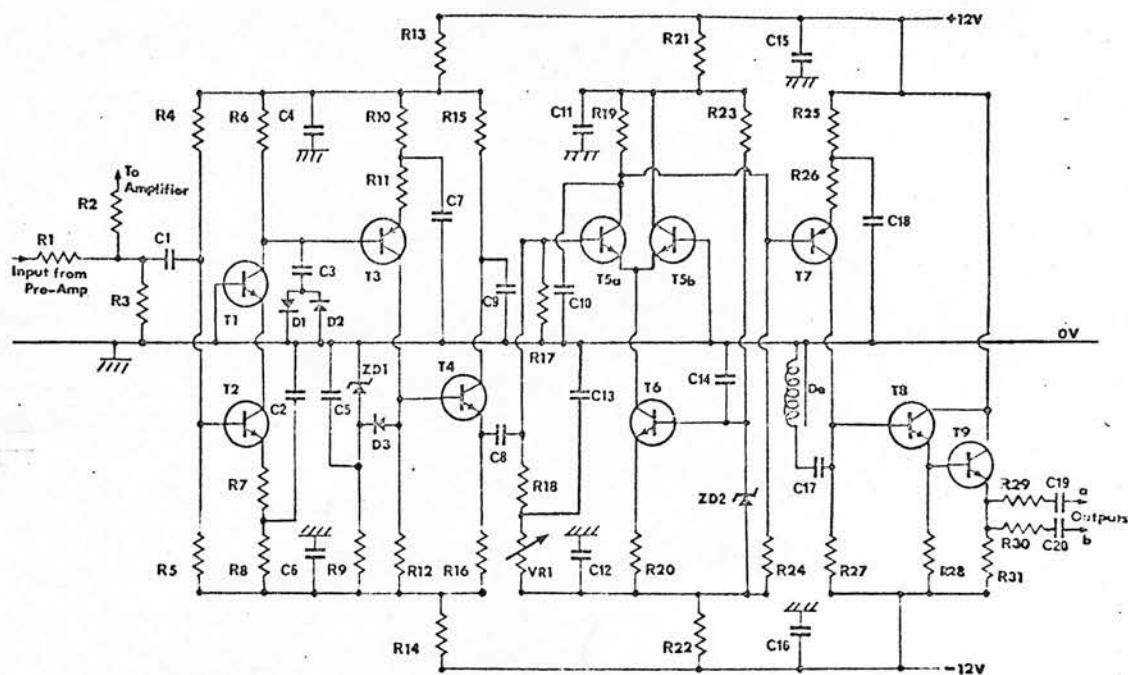
These several sources of possible fault are brought together (I.C.14) and for any mode this can create a low-high transition from I.C.15. This powers a dual frequency oscillator and if alarm mode is selected 12v. is supplied to an output transformer giving a two tone audible warning throughout the laboratory's suite of rooms. If auto mode is selected, action is delayed for an adjustable time up to 3 seconds (I.C.19) so that if the fault is of a very transient nature e.g. momentary beam low, it may be overlooked but latch recorded. However, in this mode, a valid fault sets a bistable (I.C.18) and a fault level is created to activate a relay breaking an interlock on the belt motor supply and causing the closure of the main gate valve. In manual mode only a visual indication of fault conditions is given. The mode select switch combines all the necessary switching operations using several wafers, and additionally gives an LED indication of the mode selected.

This circuit has enabled users to leave the accelerator overnight under stable running conditions and has generally removed the need for immediate or continuous supervision of the machine. This, and its reliability has helped obtain continuous running of experiments over 250 hour periods.

A3. The P.S.D. unit.

The design of this unit is detailed elsewhere [23] as are comparative studies of its performance [24]). The circuit makes possible discrimination between gammas and neutrons on the basis of the time from start to zero cross-over of a bipolar pulse derived from the linear output of the detector.

The building of this circuit in a single width module necessitated consideration of the layout of the electronics and provided a convenient stage to incorporate modifications and substitutions decided on from earlier tests. The figure (A4) illustrates the circuit and represents the approximate disposition of the components with alterations. Of prime importance is the provision of a good central earth line so that separate stages may be immediately decoupled. The TAC (time to amplitude convertor) stage of this circuit is built round a difference amplifier (a long tailed pair originally consisting of a 2C444 dual transistor with a BFY74 acting as constant current source). The original transistors are here replaced by a package containing 6 transistors arranged as two long tailed pair stages [25]) (CA3049) and possessing a superior gain band width product. Similarly, advantage is taken in improvements in technology in selecting compact low distortion delay line [26]). This serves to clip the slowly decaying pulse generated on C10, the amplitude of which represents the start to cross-over time referred to above. The lower impedance of this delay line necessitated a change of matching resistors, and

PULSE SHAPE DISCRIMINATION UNIT

R1 = 33Ω	R12 = 1.5kΩ	R23 = 4.7kΩ	C1 = 0.22μF	C12 = 2.2μF	T1 = BFY75	D1 = 1N251
R2 = 33Ω	R13 = 68Ω	R24 = 18kΩ	C2 = 600mF	C13 = 2.2μF	T2 = BFY75	D2 = 1N251
R3 = 150Ω	R14 = 68Ω	R25 = 680Ω	C3 = 0.22μF	C14 = 0.22μF	T3 = BFX48	D3 = 1N251
R4 = 15kΩ	R15 = 680Ω	R26 = 270Ω	C4 = 2.2μF	C15 = 2.2μF	T4 = BFY75	ZD1 = BZY88-C4V3
R5 = 3.0kΩ	R16 = 680Ω	R27 = 4.2kΩ	C5 = 0.22μF	C16 = 2.2μF	T5 = 2C444	ZD2 = BZY88-C4V3
R6 = 1.8kΩ	R17 = 10kΩ	R28 = 3.3kΩ	C6 = 2.2μF	C17 = 0.22μF	T6 = BFY74	
R7 = 68Ω	R18 = 33kΩ	R29 = 82Ω	C7 = 2.2μF	C18 = 0.01μF	T7 = BFX48	
R8 = 1.5kΩ	R19 = 2.2kΩ	R30 = 82Ω	C8 = 0.22μF	C19 = 0.22μF	T8 = BFY75	
R9 = 4.7kΩ	R20 = 1.2kΩ	R31 = 1.2kΩ	C9 = 0.22μF	C20 = 0.22μF	T9 = 2N1711	
R10 = 1.2kΩ	R21 = 100Ω		C10 = 1500pF			
R11 = 100Ω	R22 = 100Ω	VR1 = 1MΩ	C11 = 2.2μF			

MODIFICATIONS

R_{25} = 100Ω

$C_3 = \dfrac{0.22 \ \mu F}{1000 \ pF}$

T_5, T_6 = CA3049

R_{26} = 39Ω

$C_6 = C_4 = \dfrac{2.2 \ \mu F}{1000 \ pF}$

T_7 = 2N1132

R_{27} = 620Ω

D_e = CCCB817-7
(700ns, 600)

Fig. A4 Circuit/Layout diagram for the modified P.S.D. unit.

the opportunity was taken to increase the gain of this stage thus increasing the gamma-neutron differential. Because of the higher current consequently drawn, a higher wattage transistor was substituted in this stage. Consideration of the current drain from the $\pm$ 12v. rails for the last two stages led to careful decoupling of the supplies to the early stages in particular the use of silver mica capacitors in parallel with the larger polyester capacitors previously used.

These changes gave a marginal improvement in performance (fig. 10) while giving a more compact unit.

A4. Coding units.

The coding units previously developed for use with Laben analysers are described elsewhere [21]. Their function is to accept coincidence pulses from the side detector electronics and translate them into a routing code for sub-group analysis. These units have been extended and additional circuits incorporated to make the logic outputs suitable for use with the ADC-computer interface units (A5) and provide the coding capability for the second set of detectors. In this application the routing pulses must be supplied to synchronize with the conclusion of A-D conversion and thus adjustable delays up to 12 μs must be built into the coding unit. In the case of the backward coding (Fig. A5) this is accomplished with monostables (I.C. 10,13) creating variable length pulses and outputs are generated off the trailing edge (I.C. 9,12) of these pulses. The coding outputs are most conveniently derived from the scaler outputs of the existing RTL logic, but for the forward coding the entire circuit was constructed from TTL, but generating the same coding pattern:

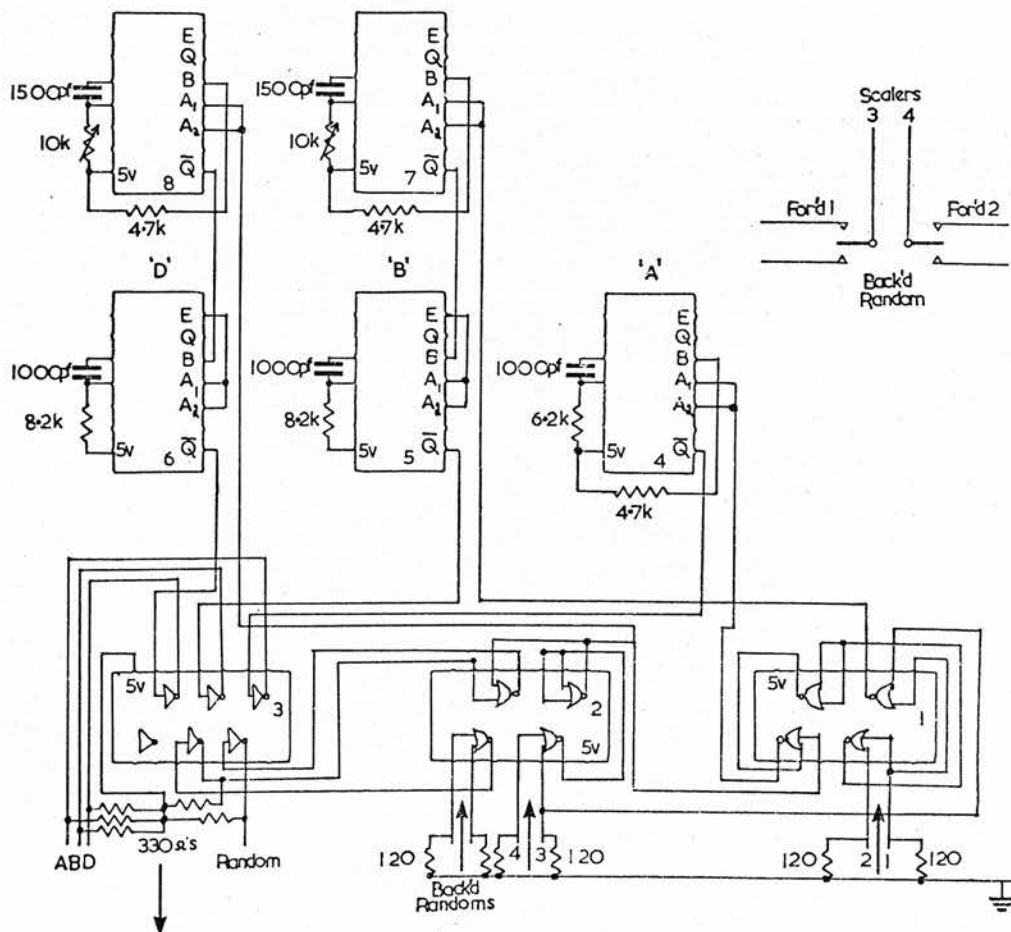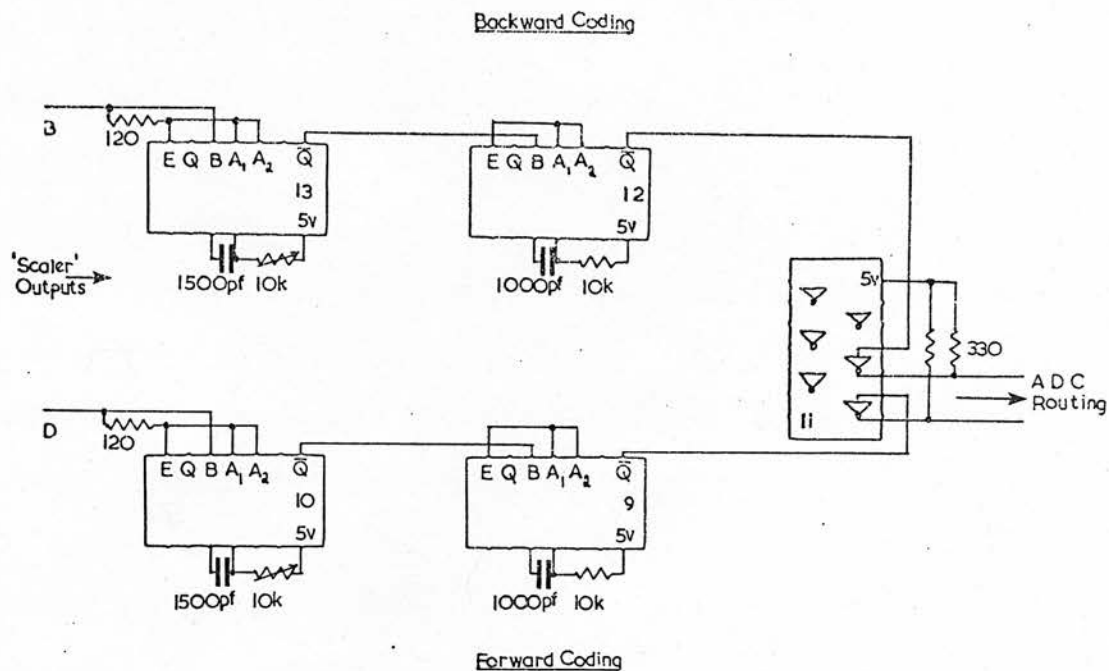| Input	A(coinc.)	B	D
1	1	1	0
2	1	0	0
3	1	0	1
4	1	1	1

Fig. A5. Backward and Forward coding circuits.

This pattern was created by 'or'ing' (I.C.s 1 and 2) the inputs and deriving the routing pulses as in the backward case. Note that a 'prompt' coincidence pulse is required. In addition, the 'random' inputs of both backward and forward electronics are 'or'd' together to provide a front panel output for scaler counting of the total number of random events. A switch was provided to enable either the backward random counts or the forward 'real and random' counts to be routed by back-wiring to the second half of the adjacent quad-scaler (A6).

Though this unit posed a trivial design problem, it was essential to the performance of simultaneous backward and forward data collection.

A5. ADC – Computer interface units.

The original units [20]) were modified in collaboration with
F.McN. Watson to allow up to 3 bits of identity information to
be incorporated in each data word as presented to the computer.
Thus the computer receives a 9 bit data word of which 6, 7 or 8
bits may be the buffered output of the 256 channel ADC utilising
part or all of its conversion range while the most significant
3, 2 or 1 bits may be externally sourced for labelling the data.
This label is called a routing code, being similar in operation
to the coding unit outputs for sub-group analysis with the
alternatively used 400 channel pulse height analyser, (P.H.A.).
The computer treats the data in an identical fashion to the
P.H.A. and treats the interface as a peripheral with direct
memory access (D.M.A.). Thus, this unit is more fully described
as a memory increment D.M.A. interface. In the present application
128 channels were used allowing two bits of routing information
per event.

The figure (A6) illustrates the use of common emitter stages
for the data line driving to the computer. The use of the 7th
and 8th data lines interchangeably between ADC outputs and
routing inputs is accomplished by 'nanding' these lines (I.C.8)
and appropriate choice of ADC conversion range. The ADC signals
the completion of A – D conversion on the data-ready line. The
interface unit derives a data ready signal for the computer
(I.C. 3,5) with a common emitter stage for line driving, and a

Fig. A6. ADC – Computer interface circuit.

$\bar{Q}$ pulse (I.C.s 5,6) to set a bistable (I.C.8) which in turn enables the latch (I.C.7). This latch transfers the state of the routing inputs to the drive stages at the instant it is enabled and hence the need for appropriate delaying of these inputs as referred to previously (A4).

The computer signals the completion of data storage by sending a data accepted signal (which must see a 100 Ω input impedance). This is used to reset the latch enabling bistable (I.C.8), and also passed to the ADC to allow it to accept the next analogue signal. A zero level will appear on the computer interface run-stop line should data processing be terminated by program or teletype control. This has the same effect as the data accepted signal (being 'or'd' together by I.C.1) but additionally is passed to the ADC to terminate conversion and reset bistables. It is also accessible at the front panel of the unit for other control functions, e.g. to initiate polarimeter rotation and to stop scalers counting.

The design of this unit makes redundant a further control line - the ADC's data request line - and this is tied high thus permanently enabling the ADC's transfer gates. The latch enable line is accessible at the front panel for oscilloscope monitoring when setting the delay on the routing pulses to best synchronize with the rest of the'data word'.

The original units used resistor transistor logic (e.g. μL927)

to different extents and modifications and substitutions were made using TTL devices. The figure illustrates the unit more completely altered.

A6. Scalers.

The electronic design of the basic scaler is illustrated in figure A7. This is based on the application note for the TIXL 360, 6 digit LED display marketed by Texas Instruments.

Of particular interest is the multiplex circuitry used to turn each digit on in sequence. This is driven by a 10kHz oscillator (I.C.14) which clocks a decade counter (I.C.15) and bcd to decimal decoder (I.C.16) to produce a $\bar{Q}$ pulse for use with consecutive scaler digits. The circuit recycles itself when a sequence of outputs equal to the number of scaler digits is complete. The scaler input is fed to decade counter I.C.13 and higher decades are incremented by transitions on D outputs. The multiplexing circuitry arms nands (I.C.8-4) fed from consecutive decade counters routing this bcd information to the 7 segment decoder (I.C.1) and powering the appropriate segments. The multiplexing simultaneously powers (I.C.3) the digit corresponding to each decade counter in turn and as stated then returns to the first digit cyclically. This process is easily extended to scalers of six or more digits. It has the advantage of reducing the current required for a certain digit luminance and economises on the use of seven segment decoders.

For auto recording, the bcd scaler information may be output on a data link through transfer gates which may be enabled by a high on the strobe line. Resetting the scalers is accomplished
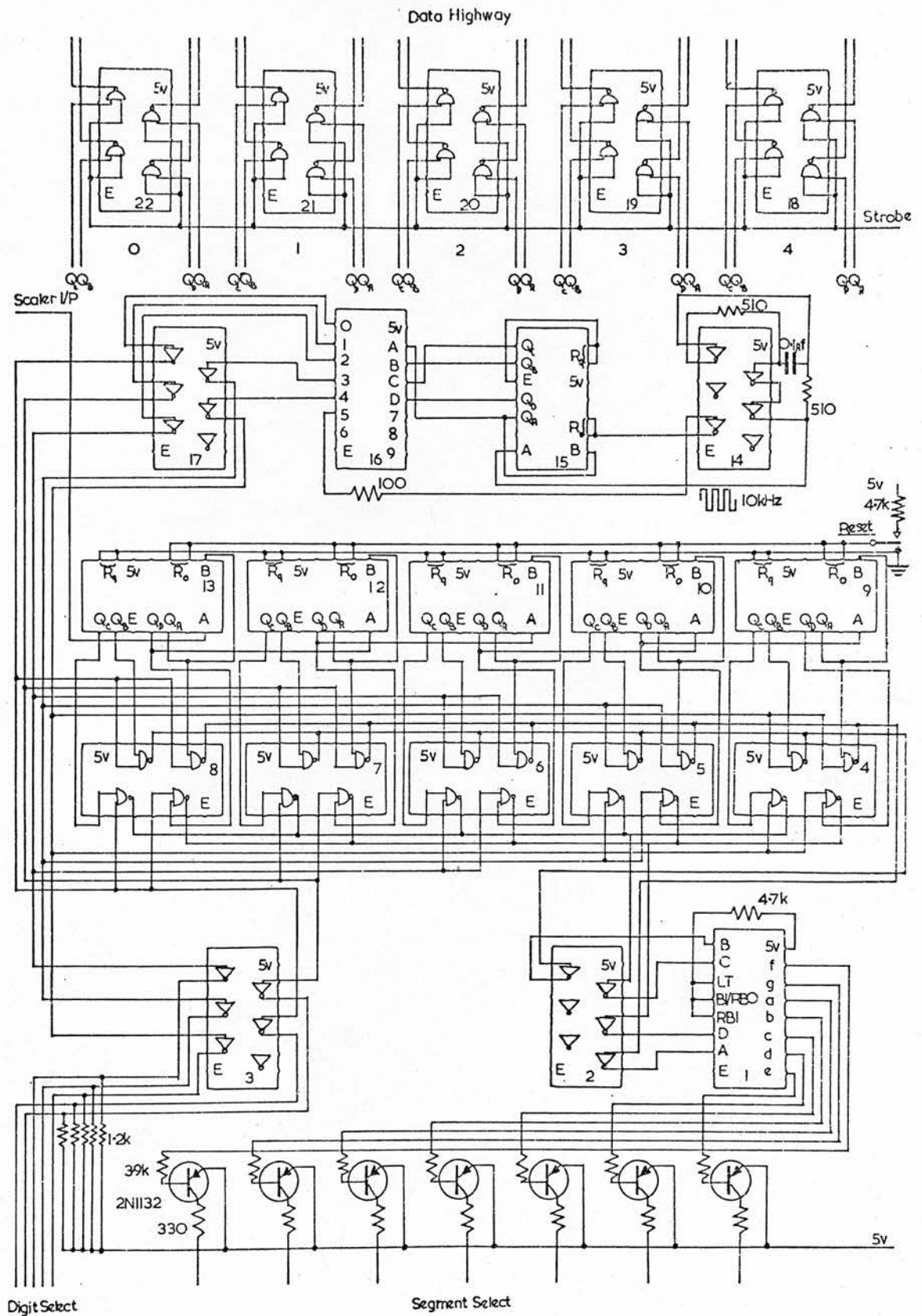
Fig. A7. Five decade scaler circuit.

by holding the R_o's of I.C.s 9-13 high by switch or equivalent process. These and a variety of other control functions are illustrated in figure A8.

The operation of the scalers is designed to allow integration into a system complete with line printer (A7) while keeping the ability to operate individually. Figure A8 refers to the control board of the quad-scaler which incorporates stages also used in the nim module version of the scaler.

Stop pulses for the scalers may be generated by timers on pulse height analysers or TTL control units. Appropriate selection for positive or negative voltage logic input routes a '0' for stop level to I.C.18 where it is nanded with the manual stop switch. (In the case of nim scalers, the stop pulse may be backwired in). The output is nanded (I.C.19) to control the passage of data to the decade counters. On the quad-scaler, an additional switch selected control allows external gating (through monostable I.C.14) of data counting.

When counting is stopped, the control gates (I.C.9-13) are armed so that the line printer may initiate data transfer by sending a data begin pulse. This sets the print-out bistable (I.C.13) providing a positive level to the print command and arming the print-out gates (Fig.A6) on the first scaler. When the line printer sends a 'data reset' pulse, the print-out
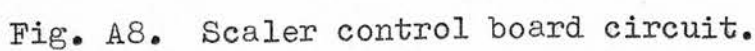
Fig. A8. Scaler control board circuit.

bistable output goes low and does three things: it disarms the print-out gates; it restores the print command line to '0', and it provides a negative transition to the transistor stage which provides a $5 \mu s$ 'data end' pulse to the next control gate (I.C.12) where it is treated as a 'data begin', repeating the process. After the final print-out, the data end is returned to the line printer. However in the single nim scalers there is only one cycle of this process, and the 'data end' pulse is passed to the next scaler along the back-wiring or returned to the line printer direct.

Scalers restart counting on receipt of a transition on the start/stop input for the nim scalers; this may alternatively be signalled by a pulse on the start/reset line of the data highway. In general, this transition is used by monostable I.C.15 to derive a reset pulse for all the scalers so that the last reading is visible throughout the waiting period. The nim scalers are fitted with a switch preventing reset if accumulate mode is required.

A means of providing a run number is provided on the quad-scaler. I.C.s 6-8 are up-down decade counters which may be loaded by a 3 digit thumbswitch and incremented at the beginning of data collection by a pulse from the reset monostable (I.C.15). The transfer gates operate in the same way as in the scalers and are armed last so as to appear above the scaler readings on the

print-out. Two digits are not allocated but wiring exists should other labels, e.g. polarimeter position, need to be given with the run number.

The quad-scalers are accessible through the adjacent coding unit for any source of TTL/RTL pulses for any user. The data transfer is by a 24 line data highway (4x5 bcd digits plus four control lines) with separate line to control the stop and start/ reset of counting. For the nim scalers, a data highway was constructed for the rear of a nim bin (4x6 bcd digits plus six control lines). One of the nim scalers is constructed with an integral discriminator of standard design [21]) on the input, but otherwise the three nim scalers constructed are identical. Provision is made for switching one or two nim scalers out of the data highway and either the quad-scaler alone or selected nim scalers or a combination of both may be read out to the line printer.

This scaler design has proved to be reliable and flexible. The nim module form of this circuit is sufficiently attractive to have justified creating a two sided PCB version and additional units may be produced with ease.

A7. Line Printer Scaler System.

This data acquisition system was designed to be compatible with the Nuclear Enterprises range of scalers and timers. The control and command signals were decided upon with consideration of pending I.E.C. recommendations [22]). Data transfer is by 4 bit x 6 digit parallel data line and control by 7 lines with special separate wiring for interfacing to the quad-scaler. This latter requires a 4 bit x 5 digit parallel data line plus 5 control lines.

Provision is made for a flexible system of control. The stopping of the scalers is simultaneous with commencement of printing and may be instigated by manual push-button, and internal presetable timer (range $1x10^1$ to $9x10^4$ secs.), or by an externally sourced voltage (switch selectable to cope with positive or negative voltage levels for stop). A three-way switch allows selection of the source which will stop the scalers and start printing. There is an almost identical arrangement for the 'recycling' of the scalers, except that the selection of auto start with the separate three-way recycle switch starts the scalers immediately the print-out has finished.

Most of these controls are accomplished by the circuitry illustrated in Figure A9. The start print switch selects between three sources of 'stop' level: a push-button with bistable to remove the effects of bounce; a switch which selects between
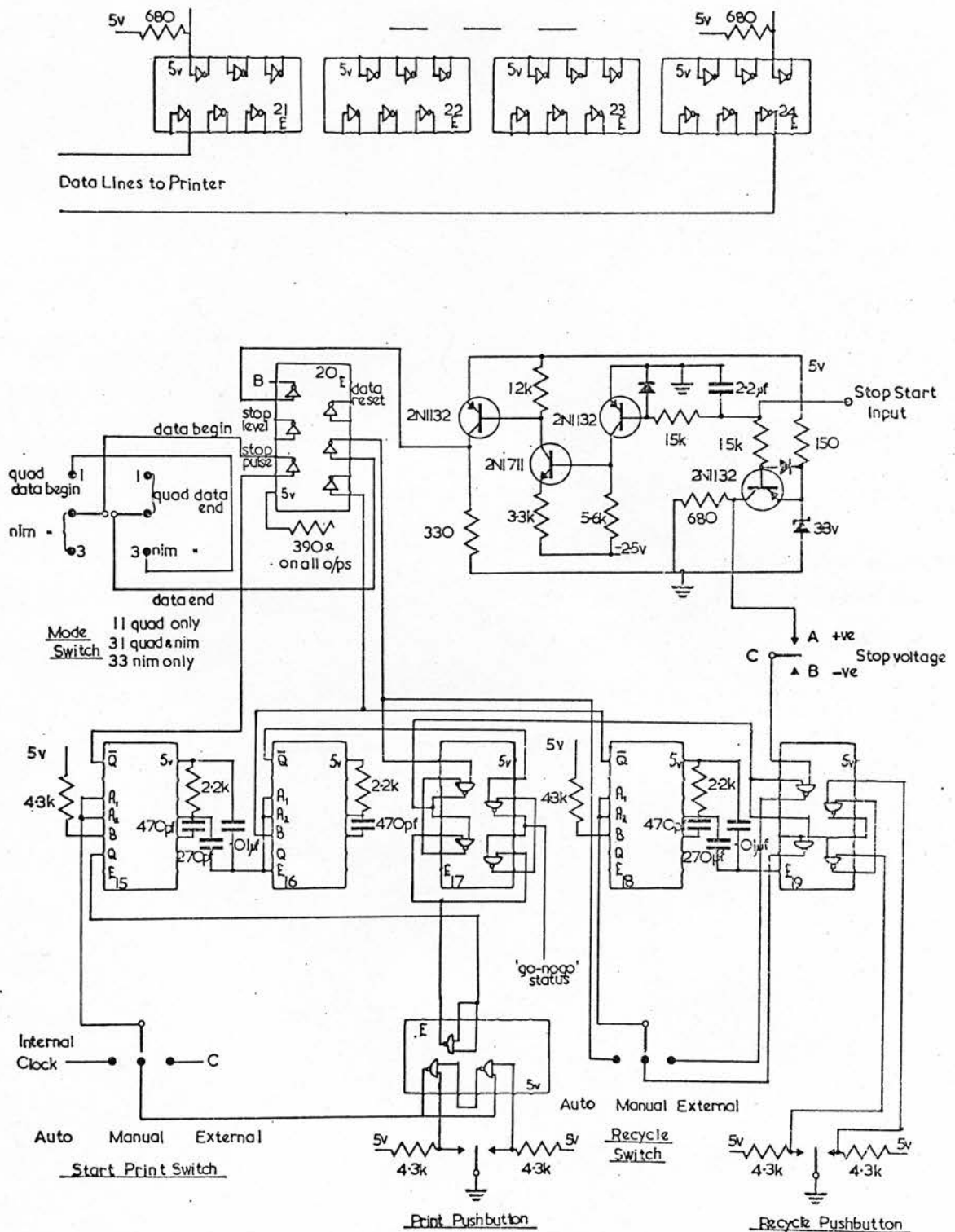
Fig. A9. Line Printer Control Board circuit.

circuits accepting external stop signals of either positive or negative voltage logic; a negative transition generated by the internal clock to be described in connection with Figure A10. The selected stop line may fire a monostable (I.C.15) to produce a 'data begin' pulse which initiates the data transfer process (A6) and a 'stop' pulse for the nim scalers, and also sets the two bistables of I.C.17. The left bistable provides a '1' level on pins 3,4 to indicate the completion of print-out and the right bistable provides a '1' level on pins 10,11 to indicate that counting is in progress. The latter level is required on the other circuit board (Fig. A10) and is output as the quad-scaler stop/start level and the former level is used to enable the gates (I.C.19) associated with recycling. The recycle bistable (I.C.17) is reset on receipt of the 'data end' pulse from the last scaler in the sequence to signal the completion of data transfer to the line printer.

The recycle switch similarly selects between three reasons for recycle: a push-button, with bistable to remove the effects of bounce, which supplies a negative transition if the following gate is armed by the recycle bistable; the return of the externally sourced stop signal to the 'go' state, again if passed by the recycle bistable; the above mentioned 'data end' pulse if recycling is required immediately the printing is finished. The selected recycle line may fire a monostable (I.C.18) to provide a reset and start pulse to the scalers (I.C.20) and to fire another monostable (I.C.16) so that the resetting of the

'go – no go' bistable may be delayed by 5μs. All monostables and drivers are decoupled to minimise the possibility of transients affecting performance.

This board also contains the input data buffers (I.C.s 21-24) at which the various scaler data outputs are 'wire or'd' together before transfer to the printer [23]).

The circuit board illustration (Fig. A10) is concerned mainly with the internal clock and the control functions of the Moduprinter itself. The 555 Timer (I.C.13) is used to produce a 10Hz clock pulse which is also rectified to provide a negative voltage required for autostop level conversion (Fig. A9). The clock pulse is fed to a sequence of decade counters (I.C.s 1-5). A front panel thumbswitch and bcd – decimal decoder provide a '0' level so that 'or⁸ing' (I.C.8) with the outputs of counters only provides transitions to I.C.6 for the selected power of ten. I.C.6 counts the occurrence of such transitions until I.C.s 7,8 find agreement with the multiple of 10^n secs selected on a second thumbswitch. If the scalers are still counting a stop signal may be generated as previously explained, but if the line printer is 'waiting' and the desired pattern recurs (as it will every 10^{n+1} secs.), nanding with the (I.C.11) 'go – no go' level from (I.C.17) prevents the generation of a further stop pulse.

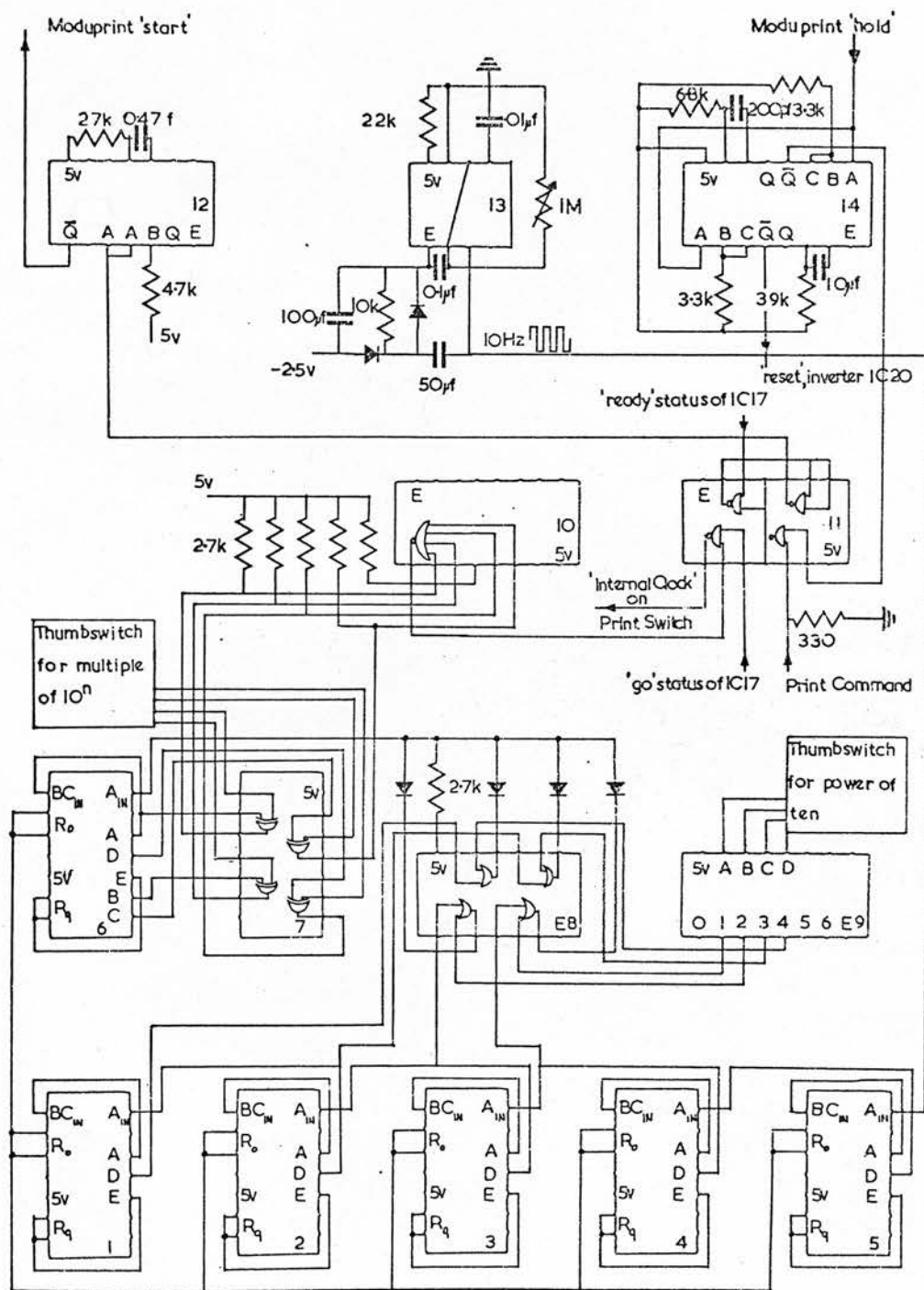The Moduprinter has only two control lines. The print command

Fig. A10. Timer and Moduprint control board.

pulse from each scaler is received by a monostable (I.C.12) to derive a clean version of this pulse for the moduprinter. It responds with a long 'hold' signal to give time for the printing process. The end of this pulse is used to produce (I.C.14) a common data reset pulse to trigger the next scaler into data transfer, and also to produce a delay before the next printing (I.C.s 14 and 11) to allow time for the winding on of paper. Transients can generate false print commands and therefore this signal is gated with the output of the recycle bistable to inhibit such pulses.

The line printer is constructed in a three width nim module but it has its own power supplies and a.c. mains input so that free standing operation is possible. Both the nim and quad-scalers have their own data highway cables so that routing and sequencing of scalers is simply arranged. The system has the flexibility to meet the requirements of a variety of applications, it economises on running time by rapid data recording, and relieves other sophisticated equipment previously used as timers or to control measurement sequences.

PDP-11 Interrupt Unit.

The Program Interrupt interface was designed to give a more versatile method of feeding data to the PDP 11-45 than could be obtained using the memory increment DMA interface. This versatility is gained at the expense of data rate. Three modes of operation are provided:

(a) <u>Test.</u> In this mode the data lines can be set individually to the "0" or "1" state, and a transfer request triggered by a push button. Hence the full range of 8 bit numbers ($\emptyset$ - 255) can be used to test the lines. The test program INT1 in the file *INT1* in File index 17 is provided. It uses the basic routine:

<u>integerfn</u> GET

   *EMT ⌴244

   <u>RESULT</u> = ACC

   <u>END</u>

which should be used to acquire data from the interface.

(b) <u>external data source.</u> In this mode, 8 bit data with 'handshake' control is provided from an external data source. This is used at present to take blocks of 1024 words (2048 8 bit transfers) from the peripheral driver on the Neutron Physics CAMAC system. The program *LINK* places the result in the file LINKFL.

(c) <u>multiplex ADCs.</u> In this mode, two LABEN 256 channel ADCs are used. They are assumed to be acquiring dual parameter

data in coincidence with each other. When both ADCs have
finished analysing the event, the interface ends ADC1's
data, then ADC2's data, then resets them both. An 'enable'
switch on the front can inhibit the ADCs from counting.
The reset button on the front should be used at the
beginning of a run to ensure that the order of transfers
is correct.

The figure illustrates the 'or'ing' together of the various
data sources and the handling of control logic. According to
the mode selected, different sets of open collector nand gates
are enabled (I.C. 11-18) and the outputs are 'wired or'd'
together to provide the 8 bit data word. If multiplex is
selected, I.C.6 waits (LED lit) till receipt of data ready
levels from both ADCs and then fires Monostable 1, and 2 in turn.
The latter thus produces a $\bar{Q}$ pulse after 5µs delay and the
selection of Multiplex (Rotary switch) passes this through an
o-c. nand (I.C.3) to provide a Data Ready pulse to the computer.
The Reset button sets the flip-flop (I.C.9) into a 'Q=1' state
initially. This lights one Transfer LED and arms one gate in
I.C.7 enabling the transfer gates of ADC1. After computer
storage, a reset pulse is returned and clocks the flip-flop
similarly enabling the other ADC transfer gates and lighting the
other transfer LED. Following the sequence, the next transition
of the flip-flop causes a pulse on the run-stop line (Monostable 5)
resetting all the ADC bistables.

If external is selected a similar process is followed. In this mode only one nand of I.C.7 is armed and a data ready from the external source causes the transfer gates (I.C.15 and 16) to be enabled. A Monostable (I.C.4) is also fired on the B i/p to produce a data ready pulse for the computer. The returning reset is routed direct to the external source along with an inverted copy. The flip-flop is also caused to toggle as before, causing alternate illumination of the transfer LEDs as before.

In the test mode, a push-button performs the role of data ready. The same Monostable (I.C.4) is fired on the A i/p to produce the Data Ready pulse, but the reset pulse returned by the computer is redundant in this case. Each pattern is set up and triggered individually.

The use of this unit has so far been limited to operating in the external mode. In this application it has been used to interface the CAMAC Peripheral Driver to the PDP 11-45, the former itself being sourced by a PDP 11-05.

Appendix B : Determination of coefficients in the differential polarization expansion.

Consider quantities linearly related as :

$$a_1 A_k + a_2 B_k + a_3 C_k + \dots + a_z Z_k - X_k = \Delta_k$$

where A, B, C, ... Z, X = known quantities

k = number of equation

$a_1, a_2, a_3, \dots a_z$ = coefficients to be determined for best fit

Δ = unknown adjustment for consistency

If the values of X_k have different errors, the k equations have different weightings (w). The normal equations for the unknown adjusted 'a' values then become :

$$(\textstyle\sum_k w A^2)a_1 + (\sum_k wAB)a_2 + (\sum_k wAC)a_3 + \cdots (\sum_k wAZ)a_z - \sum_k wAX = 0$$

$$(\textstyle\sum_k wAB)a_1 + (\sum_k w B^2)a_2 + (\sum_k wBC)a_3 + \cdots (\sum_k wBZ)a_z - \sum_k wBX = 0$$

$$(\textstyle\sum_k wAC)a_1 + (\sum_k wBC)a_2 + (\sum_k wC^2)a_3 + \cdots (\sum_k wCZ)a_z - \sum_k wCX = 0$$

In the case of a three coefficient fit, these have solutions :

$$Q_1 = \frac{1}{D}\begin{vmatrix} \sum wAX & \sum wAB & \sum wAC \\ \sum wBX & \sum wB^2 & \sum wBC \\ \sum wCX & \sum wBC & \sum wC^2 \end{vmatrix}
\qquad
Q_2 = \frac{1}{D}\begin{vmatrix} \sum wA^2 & \sum wAX & \sum wAC \\ \sum wAB & \sum wBX & \sum wBC \\ \sum wAC & \sum wCX & \sum wC^2 \end{vmatrix}$$

$$Q_3 = \frac{1}{D}\begin{vmatrix} \sum wA^2 & \sum wAB & \sum wAX \\ \sum wAB & \sum wB^2 & \sum wBX \\ \sum wAC & \sum wBC & \sum wCX \end{vmatrix}
\qquad \text{where} \qquad
D = \begin{vmatrix} \sum wA^2 & \sum wAB & \sum wAC \\ \sum wAB & \sum wB^2 & \sum wBC \\ \sum wAC & \sum wBC & \sum wC^2 \end{vmatrix}$$

This is the procedure of best fitting for unequally weighted observations of linearly related quantities as described by Worthing and Geffner.[65]

The current application is the solution of :

$$a_1 \frac{\sin 2\theta_c}{\sigma(\theta_c)} + a_2 \frac{\sin 4\theta_c}{\sigma(\theta_c)} + a_3 \frac{\sin 6\theta_c}{\sigma(\theta_c)} - P(\theta_c) = 0 \quad .$$

$P(\theta_c)$ has been measured to some degree of accuracy for several (7) values of θ ; the errors provide weighting factors (proportional to $(error)^{-2}$ ibid p. 190). The observations were at measured values of θ_L from which θ_c is derived by :

$$\tan \theta_L = \frac{\sin \theta_c}{\gamma + \cos \theta_c} \quad \text{where} \quad \gamma = \left[\frac{m_d \, m_n \, K.E._d}{m_{he}(m_n + m_{he})Q + m_{he}(m_{he} + m_n - m_d)K.E._d} \right]^{\frac{1}{2}} \quad [66]$$

$\sigma(\theta_L)$ for the D-d reaction is given by Liskein[1] from which $\sigma(\theta_c)$ is calculated according to :

$$\sigma(\theta_c) = \frac{\sigma(\theta_L)|1 + \gamma \cos \theta_c|}{(1 + \gamma^2 + 2\gamma \cos \theta_c)^{\frac{3}{2}}} \quad [66]$$

Expansions for the differential polarization in terms of $\sin 2n\theta$ and associated Legendre polynomials are equivalent :

$$\sum_{\ell\,even} B_\ell P_\ell'(\cos\theta) = B_0 P_0' + B_2 P_2' \qquad + B_4 P_4' \qquad\qquad + B_6 P_6' + \cdots$$

$$= 0 + \frac{3}{2}B_2\sin 2\theta + \frac{1}{16}B_4\sin 2\theta(140\cos^2\theta - 60) +$$

$$\frac{1}{16}B_6\sin 2\theta(1386\cos^4\theta - 1260\cos^2\theta + 210)$$

$$= \left[\frac{3}{2}B_2 - \frac{15}{4}B_4 + \frac{105}{16}B_6\right]\sin 2\theta + \left[\frac{35}{4}B_4 - \frac{315}{8}B_6\right]\sin 2\theta\cos^2\theta +$$

$$\frac{693}{16}B_6\sin 2\theta\cos^4\theta$$

$$\sum a_n\sin 2n\theta = a_1\sin 2\theta + a_2\sin 4\theta + a_3\sin 6\theta + \cdots$$

$$= (a_1 - 2a_2 + 3a_3)\sin 2\theta + (4a_2 - 16a_3)\sin 2\theta\cos^2\theta + 16a_3\sin 2\theta\cos^4\theta$$

Therefore if B_6, a_3 are negligible, $a_2 = \dfrac{35}{16}B_4$

and

$$a_1 = \frac{3}{2}B_2 + \frac{2}{8}B_4$$

REFERENCES.

1. Liskien, H, et al   Nuclear Data Tables A11 (1973) 569

2. Galloway, R.B.   Nuclear Inst. & Methods 92 (1971)537

3. Galloway, R.B. et al   Nuclear Physics A242(1975)122
    (enclosure)

4. Rhea, T.C. et al   Proc. of the Third Int. Symp. on
    polarization phenomena in nuclear
    reactions, Madison, 1970, eds.
    Barschall, H.H., Haeberli, W., p 556
    Madison: University of Wisconsin
    Press, 1971.

5. Martinez Lugo, R.   Ph.D. Thesis, 1976

6. Davie, H.   Ph.D. Thesis, 1972

7. Alsoraya, A.   Ph.D. Thesis, 1976

8. Shamu, R.E.   Nuclear Inst. & Methods 14(1961)297
    Jenkin, J.G. et al   Nuclear Inst. & Methods 34(1965)116

9.   Electronic Design 23/19(1975)30

10. Stammbach, Th, et al   Physical Review C2(1970)434

11. Davie, H. et al   Nuclear Inst. & Methods 108(1973)581

12. Berlman, I.B.   Handbook of Fluorescence Spectra.

13. Neporent, B.S. et al   Optics & Spectroscopy 1(1956)951

14. Birks, J.B.   Private communication

15. Hall, A.S.   Internal Report, July 1975 (enclosed)

16. Hoop, B. et al   Nuclear Physics 83(1966)65

17. Morgan, G.L. et al   Physical Review 168(1968)1114

18. Coon, J.H.   Fast neutron Physics, eds. Marion,J.B,
    Fowler, J.L., Ch.4D. New York:
    Interscience Publishers Inc., 1960

19. Seagrave, J.D. $D(d,n)He^3$ and $T(d,n)He^4$ Neutron
    Source Handbook: LAMS-2162.

20. Ayemon   Diploma dissertation, 1972

21. Davie, H.   Ph.D. Thesis 1972, Chap.3

22.   Electronic Design

23. Practical Automation Inc. Moduprinter Manual, 1972

24. Hall, A.S.   M.Sc. Thesis, 1972

25. Delaney, C.F.G.   Electronics for the physicist, Penguin
                          Educ. Series, Harmondsworth, 1969

26. Columbia Components Corp. Delay Line Manual, 1970

27. Purser, F.O. et al   Physical Review 140(1965)B870

28. Smith, J.R. et al   Canadian Journal of Physics 50(1972)
                                           783

29. Dubbeldam, P.S. et al   Nuclear Physics 28(1961)414

30. Spalek, G. et al   Nuclear Physics A191(1972)449

31. Stinson, G.M. et al   Nuclear Inst. & Methods 62(1968)13

32. Okamura, H. et al   Nuclear Physics A169(1971)401

33. Meier, M.M. et al   Physical Review 150(1966)821
     Hollandsworth, C.E. et al Physical Review 150(1966)825
     Morgan, G.L. et al   Physical Review 150(1966)830

34. Meier, M.M. et al   Nuclear Physics A182(1972)468

35. Boersma, H.J. et al   Nuclear Physics 46(1963)660

36. Fierz, M.   Helvetica Physica Acta 25(1952)629

37. Walter, R.L.   Proc. of the Third Int. Symp. on
                          polarization phenomena in nuclear
                          reactions, Madison, 1970, eds.
                          Barschall, H.H., Haeberli, W. p.317
                          Madison: University of Wisconsin
                          Press, 1971.

38. Boersma, H.J.   Nuclear Physics A135(1969)609

39. Konopinski, E.J. et al   Physical Review 73(1948)822

40. Simon, A. et al   Physical Review 90(1953)1039

41. Hardekopf, R.A. et al   Physical Review Letters 28(1972)760

42. Boersma, H.J.   Symposium on light nuclei, few body
                          problems and nuclear forces, p.503
                          (Brela, Yugoslavia, 1967)

43. Horowitz, J. et al — Journal de Physique et la Radium 14(1953)695, 731

44. Fairbairn, W.M. — Proceedings of the Physical Society 67(1954)990

45. Goldberg, M.D. et al — Physical Review 119(1960)1992

46. Simmons, J.E. et al — Physical Review Letters 27(1971)113

47. Gruebler, W. et al — Nuclear Physics A193(1972)129

48. Hilscher, D. — Nuclear Physics A179(1972)187

49. Salzman, G.C. et al — Nuclear Physics A222(1974)512

50. Dieder, J.C. et al — Nuclear Physics A196(1972)107

51. Clegg, T.B. et al — Physical Review C8(1973)922

52. Lisowski, P.W. et al — Nuclear Physics A242(1975)298

53. Blyth, C.O. et al — Physics Letters 33B(1970)211

54. Seiler, F. — Nuclear Physics A244(1975)236

55. Lane, A.M. et al — Reviews of Modern Physics 30(1958) 257

56. Fick, D. et al — Z. Physik 265(1973)87

57. Purser, F.O. et al — Proc. of the Second Int. Symp. on polarization phenomena of nucleons, Karlsruhe, 1965, eds. Huber, P., Schopper, H., p 514 Basel: Birkhauser Verlag, 1966.

58. Bieduk, F.M. et al — Physical Review 77(1950)622

59. Rook, J.R. et al — Nuclear Physics 27(1961)79

60. Sikkema, C.P. et al — Nuclear Physics A245(1975)1

61. Maayouf, R.M.A. — Ph.D. Thesis, 1973, Chap. 4

62. Sikkema, C.P. — Nuclear Inst. & Methods 122(1974)415

63. Thornton, S.T. et al — Z. Physik 266(1974)329

64. Haeberli, W. — Fast Neutron Physics, eds. Marion, J.B, Fowler, J.L., Ch. 5G. New York: Interscience Publishers Inc., 1960

65. Worthing, A.G., Geffner, J.   Treatment of Experimental Data, Ch. 10. New York: J. Wiley & Sons, Inc., 1943.

66. Arya, A.P.   Fundamentals of Nuclear Physics, Ch. 4. Boston: Allyn & Bacon, Inc. 1966

67. Bond, J.E. et al   Nuclear Physics A258(1976)189

68. Tornow, W.   Z. Physik 266(1974)357

69. Austin, S.M. et al   Physical Review 126(1962)1532

70. Hoop, B. et al   Nuclear Physics 83(1966)65

71. Satchler, G.R. et al   Nuclear Physics A112(1968)1

72. Davie, H. et al   Nuclear Inst. & Methods 92(1971) 547

73. Stammbach, Th. et al   Nuclear Physics A180(1972)225

74. Dodder, D.C. et al   Physical Review 88(1952)520
Seagrave, J.D.   Physical Review 92(1953)1222

75. Arndt, R.A. et al   Physical Review C1(1970)903

76. Hardekopf, R.A. et al   Nuclear Physics A191(1972)468

77. Fiarman, S. et al   Nuclear Physics A206(1973)1

78. Drigo, L. et al   Nuovo Cimento Lett 1(1969)237

79. Roding, P. et al   Nuclear Physics A125(1969)585
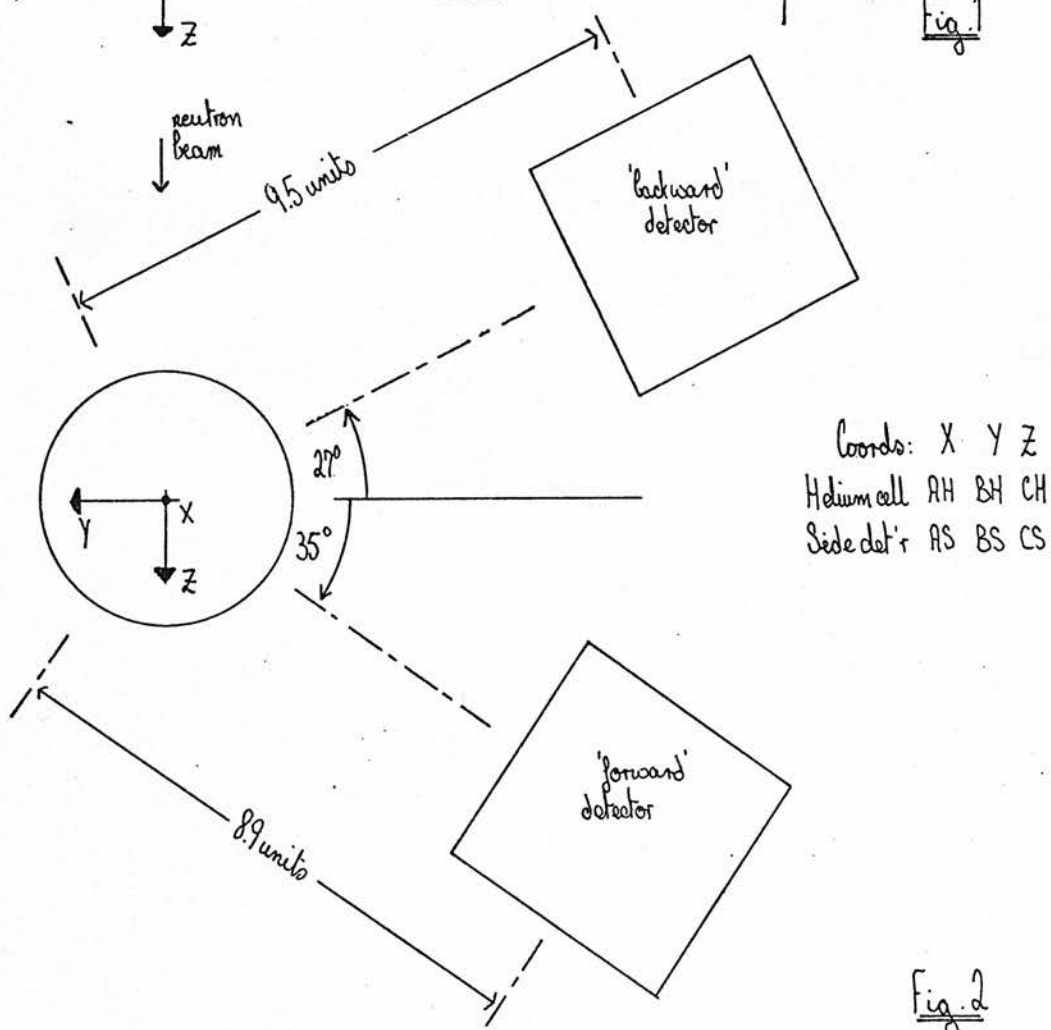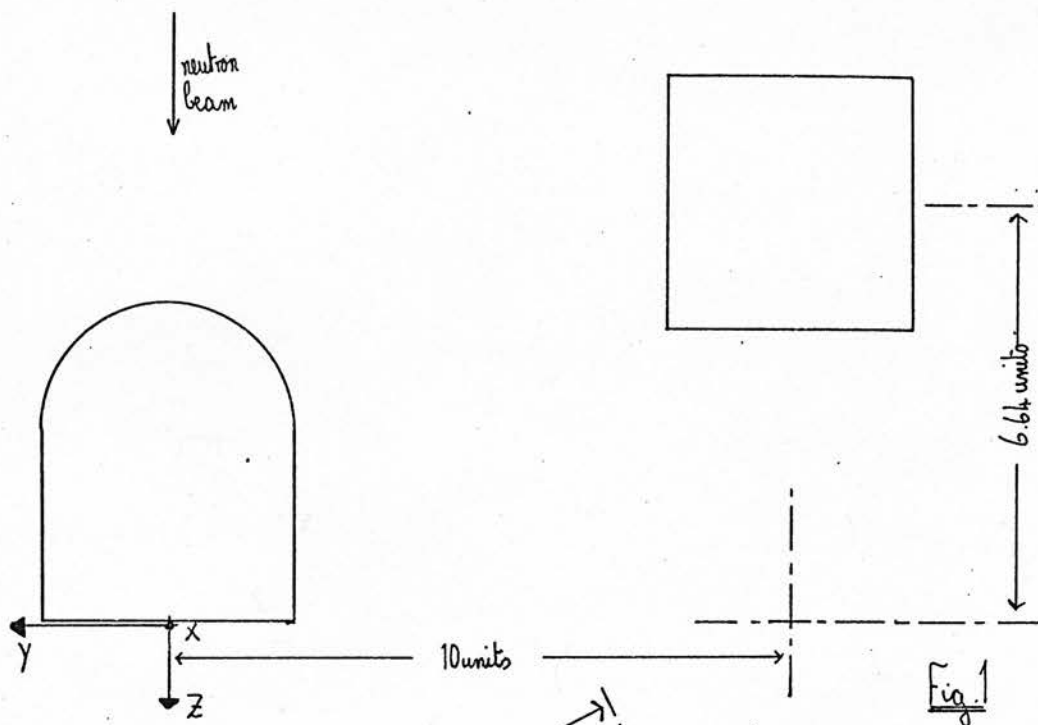
ACKNOWLEDGEMENTS.

ENCLOSURES.

This Program calculates mean analysing powers (n-He) with weightings derived from the geometry of the detectors, and corrections based on supplied values for the variation of the reaction cross-section and approximate neutron polarisation.

The calculation of analysing power is broken down as indicated on p.2, with appropriate phase shifts supplied as data and the angles of deviation and azimuth computed from individually simulated scattering events. The random coordinates of scatter and detection in the Helium and side detector are created using a 'Power Residue Method'(1) - an external function 'Random (I,1)' with values ranging from 0 to 1 - and the coordinates are further examined to eliminate events outside the defined volumes of the scintillators. The half inch is adopted as a convenient unit of measure.

In the geometry of H. Davie's polarimeter, (fig. 1), the Helium cell is defined as a right cylinder 3 units long plus a sphere of radius 2 units centred on axis but 3 units behind the base. The side detectors are defined as right cylinders 10 units off axis and displaced 6.64 units towards the target.

With the new polarimeter, (fig. 2), limitations on the coordinates in the Helium cell are expressed as a requirement to fall within the right cylinder of the cell and the horizontal cylinder of the incident neutron beam, each of radius 2 units. For the new geometry, the side detectors were initially considered as being on the y axis and described as right cylinders of radius 2 units and centred 9.5 or 8.9 units from the origin. The accepted coordinates are then adjusted by a rotation of axes through - 27° or + 35° to adjust to the real position of the side detectors. These distances and angles correspond to the mean positions

(1) IBM report CO-8011

neutron beam

6.64 units

10 units

X

Y

Z

Fig. 1

neutron beam

9.5 units

'backward' detector

27°

35°

X

Y

Z

Coords: X Y Z
Helium cell AH BH CH
Side det'r AS BS CS

'forward' detector

8.9 units

Fig. 2

$$P = \frac{-2 \, \text{Im} \, (g^* h)}{|g|^2 + |h|^2} \qquad \text{p.1407 } \Pi + F.$$

$$g = \frac{1}{k} \sum_{\ell} P_\ell(\cos\theta) \left[(\ell+1) \sin \delta_\ell^+ e^{i\delta_\ell^+} + \ell \sin \delta_\ell^- e^{i\delta_\ell^-} \right] \qquad P_0 = 1$$

$$\qquad\qquad\qquad\qquad\qquad\qquad\qquad\qquad\qquad\qquad\qquad\qquad P_1 = \cos\theta$$

$$h = \frac{1}{k} \sum_{\ell} P_\ell^{(1)}(\cos\theta) \left[\sin(\delta_\ell^+ - \delta_\ell^-) e^{i(\delta_\ell^+ + \delta_\ell^-)} \right] \qquad P_0^{(1)} = 0$$

$$\qquad\qquad\qquad\qquad\qquad\qquad\qquad\qquad\qquad\qquad\qquad\qquad P_1^{(1)} = \sin\theta$$

$$g = \frac{1}{k} \left[\sin\delta_0 \, e^{i\delta_0} + \cos\theta \, (2\sin\delta_1^{3/2} e^{i\delta_1^{3/2}} + \sin\delta_1^{1/2} e^{i\delta_1^{1/2}}) \right]$$

$$= \frac{1}{k} \left[\sin\delta_0 (\cos\delta_0 + i\sin\delta_0) + \cos\theta \, (2\sin\delta_1^{3/2}(\cos\delta_1^{3/2} + i\sin\delta_1^{3/2}) + \sin\delta_1^{1/2}(\cos\delta_1^{1/2} + i\sin\delta_1^{1/2})) \right]$$

$$= \frac{1}{k} \left[\tfrac{1}{2}\sin 2\delta_0 + i\sin^2\delta_0 + \cos\theta (\sin 2\delta_1^{3/2} + 2i\sin^2\delta_1^{3/2} + \tfrac{1}{2}\sin 2\delta_1^{1/2} + i\sin^2\delta_1^{1/2}) \right]$$

$$= \frac{1}{k} \left[\tfrac{1}{2}\sin 2\delta_0 + \tfrac{i}{2}(1 - \cos 2\delta_0) + \cos\theta (\sin 2\delta_1^{3/2} + i(1 - \cos 2\delta_1^{3/2}) + \tfrac{1}{2}\sin 2\delta_1^{1/2} + \tfrac{i}{2}(1 - \cos 2\delta_1^{1/2})) \right]$$

$$= \frac{1}{2k} \left[\sin 2\delta_0 + i(1 - \cos 2\delta_0) + \cos\theta (2\sin 2\delta_1^{3/2} + \sin 2\delta_1^{1/2} - i(2\cos 2\delta_1^{3/2} + \cos 2\delta_1^{1/2} - 3)) \right]$$

$$= \frac{1}{2k} \left[\text{calc3} - i \, \text{calc1} + \cos\theta (\text{calc4} - i \, \text{calc2}) \right]$$

$$= \frac{1}{2k} \left[\text{calc3} + \cos\theta \cdot \text{calc4} - i(\text{calc1} + \cos\theta \cdot \text{calc2}) \right]$$

$$= \frac{1}{2k} \left[A2 - i \, A1 \right]$$

$$g^* = \frac{1}{2k} \left[A2 + i \, A1 \right]$$

$$h = \frac{1}{k} \left[\sin\theta \, (\sin(\delta_1^{3/2} - \delta_1^{1/2}) \cdot (\cos(\delta_1^{3/2} + \delta_1^{1/2}) + i\sin(\delta_1^{3/2} + \delta_1^{1/2}))) \right]$$

$$= \frac{1}{k} \left[\sin\theta \, (\tfrac{1}{2}(\sin 2\delta_1^{3/2} - \sin 2\delta_1^{1/2}) + \tfrac{i}{2}(\cos 2\delta_1^{1/2} - \cos 2\delta_1^{3/2})) \right]$$

$$= \frac{1}{k} \left[\sin\theta \, (\tfrac{1}{2} \text{calc6} - \tfrac{i}{2} \text{calc5}) \right]$$

$$= \frac{1}{2k} \left[\sin\theta \, \text{calc6} - i \sin\theta \, \text{calc5} \right]$$

$$= \frac{1}{2k} \left[B2 - i \, B1 \right]$$

$$\left| \begin{array}{l} \sin\frac{A+B}{2} \cdot \sin\frac{A-B}{2} = \tfrac{1}{2}(\cos B \cdot \cos A) \\[2mm] \cos\frac{A+B}{2} \cdot \sin\frac{A-B}{2} = \tfrac{1}{2}(\sin A \cdot \sin B) \end{array} \right.$$

$$\therefore \; g^* h = \frac{1}{4k^2} \left[B2 A2 + A1 B1 + i(A1 B2 - A2 B1) \right] ; \; |g|^2 = g^* g = \frac{1}{4k^2}(A2^2 + A1^2) ; \; |h|^2 = h^* h = \frac{1}{4k^2}(B2^2 + B1^2)$$

$$\therefore \; P = \frac{-2 \, \text{Im} \, (g^* h)}{|g|^2 + |h|^2} = \frac{-2(A1 B2 - A2 B1)}{A1^2 + A2^2 + B1^2 + B2^2} = \frac{V}{U}$$

for the backward and forward scattering detectors respectively.

The displacements and angles are then computed. These distances allow the determination of the cosines of the azimuthal angle (L) and of the LAB deviation angle (K). The latter is converted into $\cos \theta_{CM}$ (COSH) using a solution of the relation:

$$\tan \theta_L = \frac{\sin \theta_C}{f + \cos \theta_C} \qquad \text{(Arya Eq}^n\text{. 4.47, p 103)}$$

where $f = \frac{\text{mass of neutron}}{\text{mass of Helium}} \approx 0.252$

and from this a subsequent line determines:

CALC 7 $= \dfrac{\sigma(\theta_{LAB})}{\sigma(\phi_{CM})}$ according to equation 4.84, p. 104 of Ayra.

The next section computes $\displaystyle\sum \frac{\sigma(\theta)}{r^2}$, (W) and $\displaystyle\sum A_{(\theta)} \frac{\sigma(\theta)\cos\phi}{r^2}$, (T) so that T/W gives <A1> , the uncorrected analysing power. With allowance for the fractional variation of the reaction cross-section (χ) across the helium cell, a corresponding term T1 is derived from which the 'false' assymetry χ may be deduced. Further evaluation of a corrected value for W1 using an estimate of the neutron polarisation gives a corrected value for the analysing power, (<A2>).

$$\epsilon = P \langle A1 \rangle + \chi$$

The effect of χ on the measured assymetry (ϵ) is easily visualised. If χ is negative, i.e. decreasing as θ increases, then the 'false' assymetry, (χ), created is negative; if χ is positive, so is χ . The magnitude of <A2> relative to <A1> depends also on whether the ϵ is positive or negative.

A two-dimensional simulation performed by hand for each of the geometries has increased confidence in the program's performance and supplied a deeper insight to the importance of several factors. Steps were added to the program to determine the probability distribution of

the angle of scatter Θ_{LAB}, and this tallied closely with the distribution arrived at by hand. The manual simulation relied on the measurement of all possible angles between subsections of the scintillators involved. These angular distributions are illustrated (fig. 3) against the analysing power curves for n-He scattering at 3 MeV.

These distributions indicate a geometric contribution of ~15% to the resolution with backward scattering. Since the observed resolution is at best 35%, the intrinsic detector resolution smears out completely any correspondence between angle of scatter and detector response. H. Davie deduced that the analysing power should be fairly uniform over the helium recoil spectrum, and this offers another way of understanding why.

Calculations of mean analysing power were performed at a variety of energies. In the hand done version, the angular distribution and elastic scattering differential cross-section provided the weighting factors. Fig. 4 shows that for both H. Davie's and the new polarimeter the computer program consistently gives values for A1 about 2% smaller than those obtained by the approximate 2-D method. The difference is therefore attributable to the program's allowance for the azimuthal angle dependence of the polarisation. The generally lower values of the new polarimeter correspond to a failure to position the side detectors at the angle of maximum analysing power (fig. 3).

The three versions of the program follow (pp 5-7). The following sections are singled out: the selection of appropriate coordinates for the site of scatter and detection; the storing of the angular distribution; and its tabulation. It should be noted that the fractional variation of the DD cross-section per half inch (λ) is as measured in the positive y - direction (p. 85, H. Davie's thesis) which for the present geometry means λ is positive for situations in which $\sigma(\theta)$ decreases with increasing reaction angle, and vice versa.

Fig. 3: Analyzing Power of Helium at 2 MeV [β: Dale Group]
[W: Wasmann Group]

Computer (dotted) and Hand (curve) simulation of
angular distribution of scatter
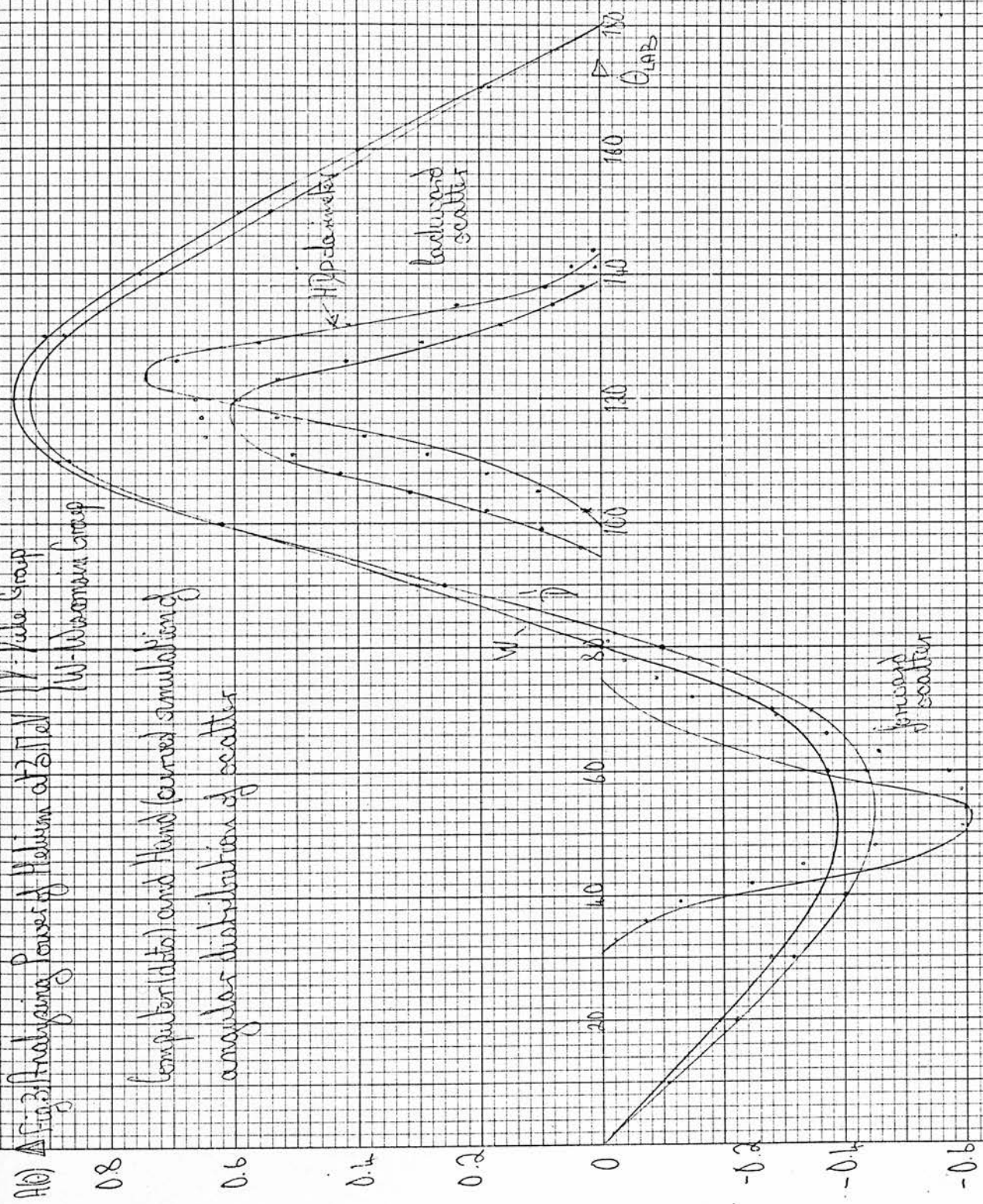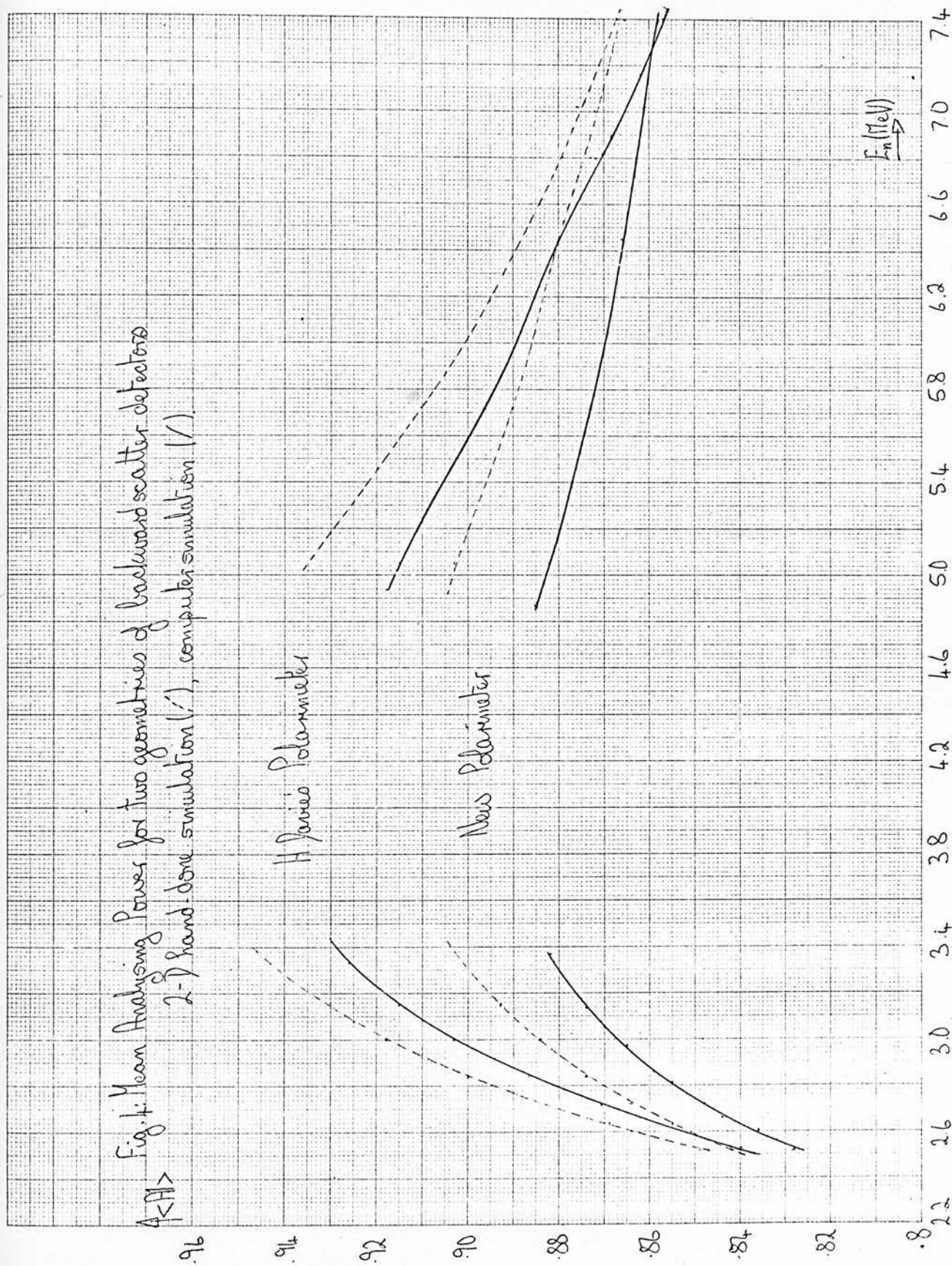
Fig. 1.4. Mean Analysing Power for two geometries of backwardscatter detectors.
2-D hand.done simulation (··), computersimulation (//).

$A\langle H\rangle$

$E_n(MeV)$

H.Pairs Polarimeter

Nais Polarimeter

2.B

THE POLARIZATION OF NEUTRONS
FROM THE ²H(d, n)³He REACTION
FOR DEUTERON ENERGIES FROM 1 TO 5.5 MeV

R. B. GALLOWAY, A. S. HALL, R. M. A. MAAYOUF † and D. G. VASS

Physics Department, University of Edinburgh, Scotland

Abstract: The dependence of the polarization of the neutrons from the ²H(d, n)³He reaction on angle of emission and deuteron energy, in the range 1.1–5.45 MeV, was determined from the asymmetry in the scattering of the neutrons by ⁴He. The polarization values are discussed both in relation to previously reported discrepant values and to the Beiduk, Pruett and Konopinski description of the ²H-²H reaction.

E | NUCLEAR REACTIONS ²H(d, n), $E = 1.1$–5.45 MeV; measured polarization $P(\theta)$.

1. Introduction

Purser, Morgan and Walter [1]), following Beiduk, Pruett and Konopinski [2]) and Fierz [3]), have shown how the energy dependence of the differential polarization of the neutrons from the ²H(d, n)³He reaction may be critical in determining the nature of the forces involved in the reaction. Their discussion was based on the polarization data for deuteron energies less than 3.5 MeV obtained by the Duke University group [1, 4]). However, a markedly different trend in the dependence of neutron polarization on deuteron energy below 2 MeV was later reported by Roding and Scholermann [5]). Markedly different values from 2 to 4.5 MeV had been reported earlier by Baicker and Jones [16]). Besides the value of reliable neutron polarization measurements to the understanding of the reaction mechanism, the ²H(d, n)³He reaction is frequently used as a source of polarized neutrons in scattering experiments. As Walter [6]) has pointed out in a review of sources of polarized neutrons there is considerable uncertainty in the polarization of the ²H-²H neutrons in the region of maximum polarization (around 49° lab.) for deuteron energies below 4 MeV.

We present polarization measurements for deuteron energies from 1.1 to 5.4 MeV which, taken along with other measurements using the same polarimeter [8,10]), gives a set of polarization values obtained by a consistent experimental technique from 275 keV to 5.4 MeV deuteron energy. Some confidence in our use of the ⁴He scattering

† Present address: Reactor and Neutron Physics Department, Atomic Energy Authority, Cairo, Egypt.

polarimeter comes from agreement between neutron polarization deduced using the ⁴He polarimeter and neutron polarization deduced from Mott-Schwinger scattering [ref. [10]]. A preliminary report of some of our polarization values was made to the Budapest Conference on nuclear structure study with neutrons [9]).

2. Experimental technique

The reaction was initiated by deuterons of 1.2 to 5.5 MeV from the Harwell Van de Graaff incident on Ti-D targets ranging in thickness from 0.9 to 3.0 mg/cm². The neutron polarimeter and data analysis procedure were essentially as described in ref. [8]). In brief, a collimated neutron beam was incident on a ⁴He gas scintillator operating at a pressure of 70 atmospheres and neutrons scattered through a mean angle of 120° were detected by a pair of liquid scintillator neutron detectors with pulse shape discrimination applied against γ-rays. The pulse height spectra due to ⁴He recoil nuclei detected in coincidence with neutrons scattered to 'right' and 'left' were recorded along with spectra due to random coincidences. The detectors were mounted on a cradle which could rotate about the collimated neutron beam direction as axis so that the 'right' and 'left' hand neutron detectors could be interchanged to cancel out any instrumental asymmetry. Measurements of scattering asymmetry in the reaction plane for polarization determination were alternated with measurements in the plane normal to the reaction plane to test for any spurious instrumental asymmetry which might upset the polarization values deduced.

Along with the expected peak in the helium recoil spectra due to the scattering of neutrons by helium through 120° and from which the asymmetry is determined, a substantial low energy tail is found which exhibits no asymmetry. This tail is caused by scattering of neutrons in the stainless steel shell or quartz window of the gas scintillator in addition to scattering in the ⁴He gas itself [8, 10]). Some of the measurements were made with the gas scintillation detector mounted axially along the direction of the collimated neutron beam exactly as in refs. [8, 10]) and some were made with the gas scintillation detector mounted at right-angles to the direction of the collimated neutron beam in order to reduce the tail of low energy neutrons in the ⁴He recoil spectra by keeping the quartz window and the photomultiplier assembly out of the neutron beam.

3. Results

In determining asymmetries due account was taken of the low energy tail in the ⁴He recoil spectra following the procedure described before [8, 10]). In addition to allowance for this low energy tail extending under the peak in the recoil spectra correction was also made for deuteron induced reactions in the Cu target backing, although this was only significant for deuteron energies of 4 MeV or more.

The mean analyzing power for each neutron energy was calculated from the phase shifts of Satchler et al. [11]) with allowance for the variation of the ²H(d, n)³He cross

TABLE 1

^{2}H(d, n)^{3}He neutron polarization values

Mean deuteron energy (MeV)	Target thickness (keV)	Lab angle (deg)	Neutron polarization	Instrumental asymm. test
1.10	±100	27	−0.080±0.006	0.010±0.007
		35	−0.102±0.006	0.003±0.006
		47	−0.145±0.009	0.005±0.007
		55	−0.166±0.008	0.001±0.007
		65	−0.128±0.009	−0.003±0.008
		75	−0.052±0.010	0.007±0.008
		89	0.102±0.021	−0.025±0.025
1.90	±150	47	−0.158±0.008	0.007±0.009
2.44	± 60	27	−0.030±0.012	0.02 ±0.02
		35	−0.070±0.011	0.02 ±0.02
		47	−0.133±0.010	−0.010±0.015
		55	−0.112±0.010	0.000±0.010
		65	−0.082±0.010	−0.004±0.010
		75	0.010±0.011	−0.002±0.008
		89	0.104±0.015	−0.002±0.013
		105	0.127±0.024	0.01 ±0.02
2.88	±120	46	−0.102±0.009	−0.01 ±0.02
2.94	±125	47	−0.103±0.010	−0.001±0.012
3.87	±125	46	−0.061±0.011	−0.014±0.011
4.93	± 70	46	−0.012±0.009	0.017±0.012
		33	0.00 ±0.02	
5.45	± 50	46	−0.02 ±0.02	
		33	0.06 ±0.03	

section [17, 20]) over the range angles subtended by the gas scintillator at the target. The neutron polarization values resulting from the corrected asymmetries in the reaction plane are listed in table 1 along with the asymmetries in the plane normal to the reaction plane which tested for instrumental asymmetry.

4. Discussion

Present and past measurements are compared in figs. 1 and 2.

Fig. 1a shows the energy dependence close to the angle of maximum polarization. Our 47° measurements are in good agreement with those from 1.9 to 3.7 MeV by Purser *et al.* [4]), they continue smoothly from the measurements below 1 MeV obtained using the same polarimeter [8]) and approach smoothly the measurements at 6 MeV and higher energies by Spalek *et al.* [13]). The variation of polarization with energy at 45° observed recently by Smith and Thornton [7]) shows a similar trend to that observed by Purser *et al.* [4]) and ourselves, but the magnitude of the polarization is slightly smaller throughout. There is substantial disagreement with the energy dependent trend in the measurements of Roding and Scholermann [5]) since their 40°
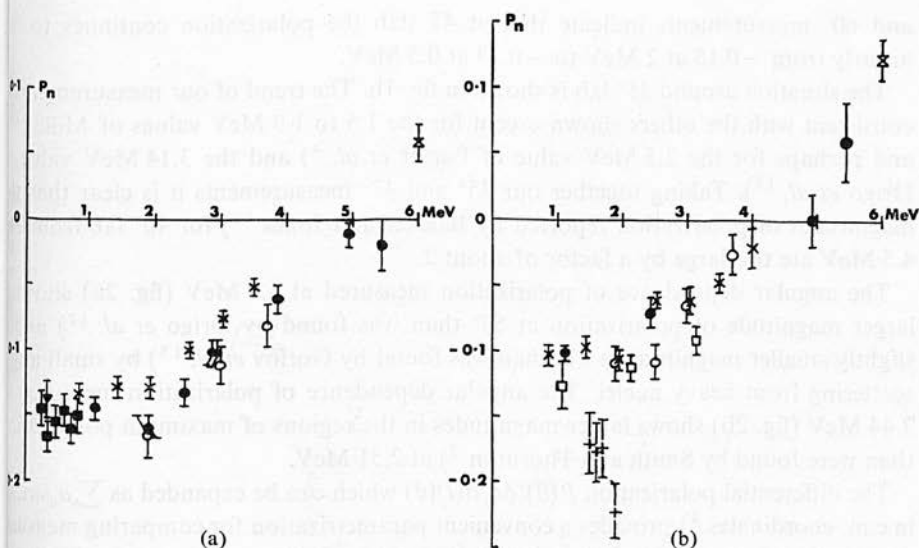
Fig. 1. Comparison of polarization values as a function of deuteron energy (a) for lab angles 5°–49° and (b) for lab angles 33°–36°. ○ Purser et al. [4]); + Miller [19]); □ Drigo et al. [12]); ⟨ Smith and Thornton [7]); ⟨ Spalek et al. [13]); ■ Davie and Galloway [8]); ▼ Maayouf and Galloway [10]); ● present measurements.
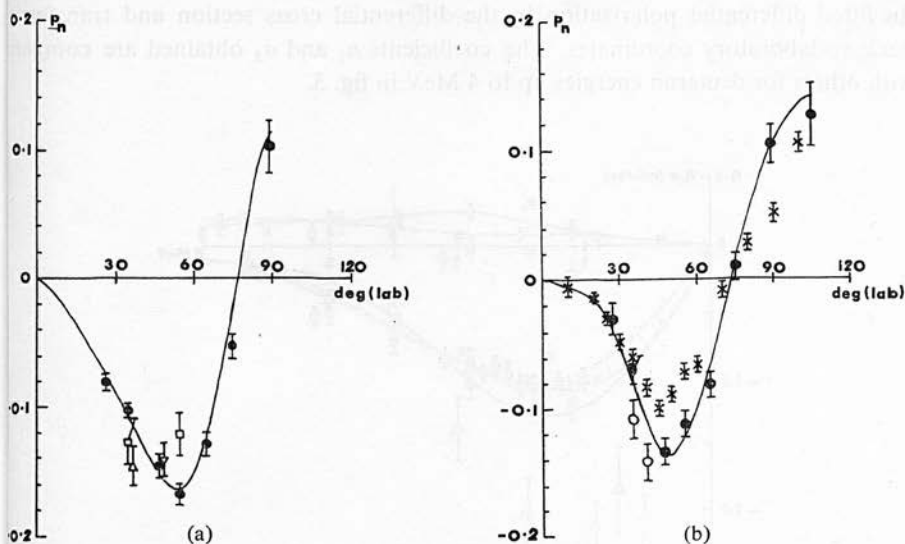

Fig. 2. Comparison of angular dependence of polarization values. (a) ▽ Levintov et al. [14]), 1.2 MeV; △ Gorlov et al. [15]), 1.2 MeV; □ Drigo et al. [12]), 1.09 MeV; ● present measurements, 1 MeV. (b) ○ Purser et al. [4]), 2.5 MeV; × Smith and Thornton [7]), 2.51 MeV; ● present measurements, 2.44 MeV. The curves are obtained from a least squares fit to our differential polarization data, see text.

and $60°$ measurements indicate that at $47°$ lab the polarization continues to fall linearly from -0.15 at 2 MeV to -0.23 at 0.5 MeV.

The situation around $35°$ lab is shown in fig. 1b. The trend of our measurements is consistent with the others shown except for the 1.5 to 1.9 MeV values of Miller [19]) and perhaps for the 2.5 MeV value of Purser et al. [4]) and the 3.14 MeV value of Drigo et al. [12]). Taking together our $35°$ and $47°$ measurements it is clear that the magnitudes of polarization reported by Baicker and Jones [16]) for $40°$ lab from 2 to 4.5 MeV are too large by a factor of about 2.

The angular dependence of polarization measured at 1.1 MeV (fig. 2a) shows a larger magnitude of polarization at $55°$ than was found by Drigo et al. [12]) and a slightly smaller magnitude at $37°$ than was found by Gorlov et al. [15]) by small angle scattering from heavy nuclei. The angular dependence of polarization measured at 2.44 MeV (fig. 2b) shows larger magnitudes in the regions of maximum polarization than were found by Smith and Thornton [7]) at 2.51 MeV.

The differential polarization $P(\theta)(d\sigma/d\Omega)(\theta)$ which can be expanded as $\sum_n a_n \sin 2n\theta$ in c.m. coordinates [3]) provides a convenient parametrization for comparing measurements with one another as well as with models of the reaction. With appropriate differential cross sections [17]) it was found by least squares fitting that for 1.1 MeV deuteron energy $a_1 = -1.07 \pm 0.04$, $a_2 = 0.11 \pm 0.08$ and for 2.44 MeV $a_1 = -0.60 \pm 0.06$, $a_2 = 0.21 \pm 0.05$. The quality of the fits, which were not improved by including higher terms, can be judged from the curves in fig. 2 which were obtained by dividing the fitted differential polarization by the differential cross section and transferring back to laboratory coordinates. The coefficients a_1 and a_2 obtained are compared with others for deuteron energies up to 4 MeV in fig. 3.
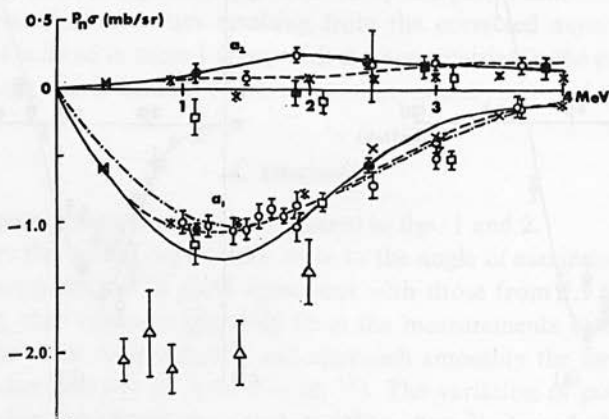

Fig. 3. The differential polarization coefficients a_1 and a_2 for deuteron energies up to 4 MeV. ○ Purser et al. [1]); □ Drigo et al. [12]); △ Roding and Scholermann [5]); × Smith and Thornton [7]); ⋈ Boersma et al. [18]); ● present values from the angular distributions in fig. 2; ■ present values from $47°$ lab data in fig. 1a.

The angular distributions of polarization measured by Smith and Thornton [7]) along with appropriate differential cross sections [17,20]) were fitted in the same way as our own data to give the a_1 and a_2 coefficients shown in fig. 3. This re-analysis was performed because no indication of accuracy was attached to the coefficients of the associated Legendre polynomial expansions of the differential polarizations listed in ref. [7]).

Considering first the a_1 coefficients, our values fall in with the trend of those reported by Purser et al. [1]) and dismiss the Roding and Scholermann [5]) values. The curves shown for a_1 are those fitted by Purser et al. [1]) to their data and are based on the approach cross-section description of the ^{2}H-^{2}H reaction by Beiduk et al. [2]). The solid line and dash-dot line are fits which assume central and tensor forces only with no spin-orbit interaction and differ only in that the 0.375 MeV measurement [18]) was taken into account in the fitting producing the solid line and not in the dash-dot case. The dashed line resulted from including a spin-orbit interaction and taking account of the 0.375 MeV measurement in the fitting. Our 2.44 MeV a_1 coefficient is consistent with all the curves while our 1.1 MeV coefficient is consistent with the dashed curve.

Also the a_1 coefficient obtained from the data of Smith and Thornton [7]) for 0.87 MeV, favours the dashed curve.

Considering now the a_2 coefficients, also shown in fig. 3, our 1.1 MeV value differs in sign from that found by Drigo et al. [12]) while at 2.44 MeV we find a value about twice that from the data of Smith and Thornton [7]). A fit to the 1.1 and 2.44 MeV values based on approach cross sections [2]) with only central and tensor interaction terms provides the solid curve which also agrees well with the a_2 coefficients from ref. [1]). Further information on the energy dependence of the a_2 coefficient may be obtained from our 47° lab data by accepting the established trend of a_1 with energy (dashed curve in fig. 3). This leads to $a_2 = -0.02 \pm 0.11$ at 1.90 MeV, $a_2 = 0.17 \pm 0.11$ at 2.94 MeV and $a_2 = 0.17 \pm 0.09$ at 3.87 MeV as indicated in fig. 3. The 2.92 and 3.87 MeV values agree well with the values from Purser et al. [1]) and with the solid curve, in contrast to the 1.9 MeV value. The dashed curve for a_2 shows how smaller a_2 values in the 2 MeV region may be accommodated within the approach cross-section description if allowance is made for a spin-orbit interaction.

References

1) F. O. Purser, G. L. Morgan and R. L. Walter, Proc. 2nd Int. Symp. on polarization phenomena of nucleons (Basel, 1966) p. 514
2) F. M. Beiduk, J. R. Pruett and E. J. Konopinski, Phys. Rev. **77** (1950) 622
3) M. Fierz, Helv. Phys. Acta **25** (1952) 629
4) F. O. Purser, J. R. Sawers and R. L. Walter, Phys. Rev. **140** (1965) B870;
   P. S. Dubbeldam and R. L. Walter, Nucl. Phys. **28** (1961) 414
5) P. Roding and H. Scholermann, Nucl. Phys. **A125** (1969) 585
6) R. L. Walter, Polarization phenomena in nuclear reactions, ed. H. H. Barschall and W. Haeberli (Univ. of Wisconsin, Madison, 1970) p. 317
7) J. R. Smith and S. T. Thornton, Can. J. Phys. **50** (1972) 783
8) H. Davie and R. B. Galloway, Nucl. Instr. **108** (1973) 581
9) R. B. Galloway, H. Davie, R. M. A. Maayouf and D. G. Vass, Conf. on nuclear structure study with neutrons (Budapest, 1972) paper A23
10) R. M. A. Maayouf and R. B. Galloway, Nucl. Instr. **118** (1974) 343
11) G. R. Satchler, L. W. Owen, A. J. Elwyn, G. L. Morgan and R. L. Walter, Nucl. Phys. **A112** (1968) 1
12) L. Drigo, C. Manduchi, G. Moschini, M. T. Russo Manduchi, G. Tornielli and G. Zannoni, Nuovo Cim. Lett. **1** (1969) 237
13) G. Spalek, R. A. Hardekopf, J. Taylor, Th. Stambach and R. L. Walter, Nucl. Phys. **A191** (1972) 449
14) I. I. Levintov, A. V. Miller, E. Z. Tarumov and V. N. Shanshev, Nucl. Phys. **3** (1957) 237
15) G. V. Gorlov, N. S. Lebedeva and V. M. Morozov, Yad. Fiz. **4** (1966) 519 [English transl.: Sov. J. Nucl. Phys. **4** (1967) 369]
16) J. A. Baicker and K. W. Jones, Nucl. Phys. **17** (1960) 424
17) J. E. Brolley and J. L. Fowler, Fast neutron physics, vol. 1, ed. J. B. Marion and J. L. Fowler (Interscience, New York, 1960) p. 73;
   V. V. Volkov, P. E. Vorotnikov, E. A. Koltipin, N. E. Sidrov and G. B. Jankov, Atomnaya Energia, Suppl. 5 (Atomizdat, Moscow, 1957)
18) H. J. Boersma, C. C. Jonker, J. G. Nijenhuis and P. J. van Hall, Nucl. Phys. **46** (1963) 660
19) T. G. Miller, Nucl. Instr. **40** (1966) 93
20) R. L. Schulte, M. Cosack, A. W. Obst and J. L. Weil, Nucl. Phys. **A192** (1972) 609